M2LW-25OR0402033

Light Water Reactor Sustainability Program

Oxygen Effects on Stress Corrosion Cracking Initiation Susceptibility of Stainless Steel in PWR Primary Water

Ziqing Zhai
Mychailo Toloczko
Pacific Northwest National Laboratory

September 2025
U.S. Department of Energy
Office of Nuclear Energy

M2LW-25OR0402033

Oxygen Effects on Stress Corrosion Cracking Initiation Susceptibility of Stainless Steel in PWR Primary Water

Ziqing Zhai
Toloczko Mychailo
Pacific Northwest National Laboratory

September 2025

Light Water Reactor Sustainability Program
Materials Research Pathway

http://lwrs.inl.gov

Prepared for the
U.S. Department of Energy
Office of Nuclear Energy
Under DOE Idaho Operations Office
Contract DE-AC07-05ID14517

Page intentionally left blank

ABSTRACT

Stainless steels (SS) comprise approximately 90% of the primary components in pressurized water reactors (PWRs), with operational history demonstrating their robustness under typical conditions. However, since the 1980s, cases of stress corrosion cracking (SCC) in unirradiated austenitic SS exposed to PWR primary water have been reported, and over 200 intergranular SCC (IGSCC) incidents in SS auxiliary piping have emerged since 2021 across multiple French nuclear power plants. These incidents, affecting non-isolable branch piping in the PWR primary circuit, raise significant nuclear safety concerns and result in substantial financial losses. While weld residual stress has been widely recognized as a key factor, it alone does not account for the prevalence of IGSCC, indicating complex interactions between welding history, operational environments, and material properties. The SCC initiation research on SS at PNNL was started in FY 2024 with the aim to identify the root cause of SS SCC initiation in service and to provide service-relevant data that can inform inspection planning and maintenance strategy development for field applications. This report documents the FY 2025 research progress made on this topic, focusing on the role of dissolved oxygen in SCC initiation susceptibility of SS in PWR primary water. SCC initiation tests on cold-forged 304L stainless steel specimens (10–40% cold-forged) were conducted in 300°C PWR primary water under constant load conditions, with dissolved oxygen (DO) concentrations of either 2 ppm or 50 ppb. Crack initiation was monitored in situ using direct current potential drop (DCPD), with post-exposure SEM analysis revealing small cracks after ~4,000 hours despite no DCPD detection of initiation during ~5,000 hours of exposure. Periodic partial unloading was recently introduced to assess the combined effects of stress cycling and DO concentration on SCC initiation under service-relevant conditions. In addition, another SCC initiation test in hydrogenated primary water on two cold-worked 304L specimens started at constant load in August 2025 with no DCPD-indication of crack initiation to-date. This report provides an up-to-date summary on the testing status and experimental findings, offering new insights into the SCC initiation processes of SS in various environments.

Page intentionally left blank

ACKNOWLEDGMENTS

The authors gratefully acknowledge the financial support from the U.S. Department of Energy, Office of Nuclear Energy, through the Light Water Reactor Sustainability Program Materials Research Pathway. In addition, Dr. Raul Rebak and Mr. Steve Buresh from G.E. Global Research Center are acknowledged for cold forging the 304L and 316L used in this study. Dr. Jared Smith at Electric Power Research Institute is acknowledged for technical discussions. Dr. Benjamin Schuessler and Dr. Nicole Overman are acknowledged for performing electron backscatter diffraction analysis on cold forged 304L and 316L materials, respectively. Dr. Mark Bowden is acknowledged for X-ray diffraction analysis of the 304L and 316L materials. Key technical assistance from Robert Fluor, Dexter Kling, Robert Seffens, Michael Blazon, Nate Brown, Jonah Garza, and Irving Brown at Pacific Northwest National Laboratory is acknowledged for testing and materials preparation activities.

Page intentionally left blank

CONTENTS

FIGURES

TABLES

Page intentionally left blank

ACRONYMS

ASN	Autorité de Sûreté Nucléaire
BNCT	Blunt notch compact tension
BSE	Backscattered electron
CF	Cold forged
CW	Cold worked
DCPD	Direct current potential drop
DC	Dislocation channels
DH	Dissolved hydrogen
DO	Dissolved oxygen
ECP	Electrochemical potential
EBSD	Electron backscatter diffraction
EdF	Electricité de France
FY	Fiscal year
GEGRC	General Electric Global Research Center
GB	Grain boundary
HAZ	Heat affected zone
IG	Intergranular
K	Stress intensity
KAM	Kernel average misorientation
NPP	Nuclear power plant
PWR	Pressurized water reactor
PWROG	Pressurized Water Reactor Owners Group
RHR	Residual heat removal
SCC	Stress corrosion cracking
SE	Secondary electron
SEM	Scanning electron microscope
SI	Safety injection
SS	Stainless steel
TG	Transgranular
YS	Yield strength

Page intentionally left blank

Oxygen Effects on Stress Corrosion Cracking Initiation Susceptibility of Stainless Steel in PWR Primary Water

1. Project Background

1.1 Objective

The primary objective of the Light Water Reactor Sustainability (LWRS) task at Pacific Northwest National Laboratory (PNNL) is to develop actionable strategies to address stress corrosion cracking (SCC) and other long-term degradation modes that threaten the reliability and performance of Ni-base alloys and stainless steels in Light Water Reactor (LWR) pressure boundary components. Understanding the long-term microstructural stability and performance of these alloys is critical for ensuring robust serviceability of LWRs. This research aims to bridge fundamental understanding with applied solutions by focusing on the practical mitigation of SCC in primary and secondary water systems of LWRs. By tailoring investigations to real-world service challenges, the work emphasizes optimizing inspection and maintenance strategies, extending the operational lifespan of critical components, and informing the design and deployment of SCC-resistant materials.

Additionally, the task evaluates the impact of emerging technologies designed to sustain reliable and economical operation of the nation's LWR fleet. The research scope is driven by industry priorities, ensuring alignment with service-oriented needs while leveraging state-of-the-art laboratory testing and advanced microscopic characterization techniques to deliver solutions that enhance safety, performance, and cost-effectiveness.

1.2 Focus of Current Report

Type 304 and 316 austenitic stainless steels are the most widely used grades of stainless steels in pressurized water reactors (PWRs), mainly for structural supports of the reactor core and pressure-retaining boundary components such as piping in the primary circuit. Operational experience with these stainless steels has generally been very good given their extensive use, with the major concern being raised on the irradiation effects on core support structures. Nevertheless, SCC cases of unirradiated austenitic stainless steels (SS) in PWR primary water have occurred in the field since the early 1980s [1] and continued to this day. Before the year 2020, a total of ~180 SCC events were reported worldwide on austenitic SS exposed to primary water environments in PWRs. The majority of the events (~84%) occurred in low-flow regions or occluded/stagnant primary water conditions. However, in August 2020, an intergranular (IG) SCC crack was reported in the pressurizer spray line piping 316 stainless steel weldment in Japanese Ohi Nuclear Power Plant (NPP) Unit 3. Since October 2021, IGSCC cracks have been detected in SS auxiliary piping systems in multiple French NPPs, causing at least twelve French nuclear power reactor units to go offline in 2021-2022 for inspection. In two years, the newly detected SCC cases reached a similar number to the total cases reported over the past 30 years worldwide. These new IGSCC cases detected in Japanese and French NPPs represent the first SCC cases confirmed in non-isolable portions of branch piping [2] in the PWR primary circuit, suggesting that IGSCC of austenitic SS in PWR environments is a potentially serious emerging issue. It is essential to have a better mechanistic understanding of the conditions under which such IGSCC incidents could take place, so that an informed inspection and maintenance plan can be made to prevent such events from jeopardizing plant operation.

To devise an adequate test plan to address such a need, a literature review was performed on relevant operational experience and associated laboratory research on the SCC of unirradiated austenitic SCC in PWR primary water in fiscal year (FY) 2023 and the information was summarized in [3]. Actual testing effort started in FY 2024 focusing on the effect of dissolved oxygen (DO) on SCC initiation of cold worked SS in PWR primary water and the initial results were reported in [4]. The current report documents the testing and characterization progress accomplished in FY 2025 on this continued effort. Chapter 2 gives a brief review of the IGSCC cases reported in the French NPPs with updates obtained in FY 2025 to provide a better understanding of the motivation of this study and the context of testing parameter selection. Chapter 3 introduces the materials purchased for this study and summarizes the mechanical property and microstructural characteristics of 304L and 316L. Chapter 4 summarizes the test progress to date on the evaluation of the effect of dissolved oxygen content on the SCC initiation of cold worked SS.

2. Background of the Study

2.1 Motivation

In October 2021, flaw indications were detected in the safety injection (SI) lines connected to the cold leg of the primary circuit at Civaux-1 during the second decennial outage [5]. The SI system is used to control accidents in which coolant escapes from the primary system due to a leak [6]. In French PWRs, it consists of a low-pressure and a medium-pressure injection systems as well as the pressure accumulators (Figure 1). It is connected in several places to the loops of the primary system, through which the water heated in the reactor core is fed into the steam generator and then cooled and returned to the reactor core [6]. The flaws were detected near two circumferential welds in an elbow weld joint made of non-sensitized 316LN, exposed to free-flowing, non-polluted hydrogenated primary water at ~300°C (Figure 2). The inspection method used was the standard mono-element ultrasonic technique dedicated to the identification of thermal fatigue cracks. To confirm the flaw indications, Electricité de France (EdF) cut out the impacted elbow weld joints and performed destructive examinations on them. The results unexpectedly revealed that the cracks detected in both weld joints are SCC instead of thermal fatigue cracks given their fully intergranular morphology (Figures 3 and 4). It should be noted that these cracks occurred in the portion of the piping immediately adjacent to the primary circuit piping, downstream of the SI isolation valves [7]. This implies that the leak cannot be isolated if it occurs at this location.

These cracks exhibit a circumferential orientation with a large aspect ratio (surface length >> depth) in the weld heat affected zone (HAZ). As shown in Figures 3 and 4, these elbow welds both have a very large root pass, but the subsequent passes were annealed during welding, which is believed to introduce compressive residual stress in the adjacent base metal [2]. This welding procedure may help explain the wider profile of elevated hardness values measured from the inner face (Figure 3) [8]. The fact that the crack did not grow deeper beyond the root pass also seems consistent with the quick drop in hardness measured from the inner surface near the subsequent passes. It is worth noting that the highest hardness values measured in these two welds did not exceed 270 HV, which is below the 300 HV previously identified as the threshold value based on operational experience for SCC initiation to occur in PWR primary water [9].

Upon detection of the above IGSCC incident in Civaux-1, EdF subsequently shut down multiple NPPs for investigations of defect alike, and additional indications were detected in multiple units at the time of this report: Civaux-2, Chooz-1 & -2, Penly-1, Chinon-3, Cattenon-3, Flamanville-2, and Golfech-1. These crack indications mostly occurred in SI lines and residual heat removal (RHR) lines in N4 (1450 MW) and P4 (1300 MW) type reactors, but not in the older, 900 MW plants [10]. The largest SCC crack detected thus far was found in Penly-1 in the HAZ of a weld in a SI line connected to the hot leg of the primary circuit. As shown in Figure 5, this weld was fully emerged in ~300°C deaerated primary water insusceptible to thermal stratification effects but was repaired twice during manufacturing [5]. By the time it was detected, the crack had grown to a circumferential length of 155 mm (~1/4 circumference) and a maximum depth of 23 mm (85% through-wall thickness) [5]. Figure 6 shows another IGSCC crack observed in an elbow weld joint in a cold leg of the SI system. The weld build-up showed a very different morphology than those reported in Civaux (Figures 3 and 4), highlighting the variability in welding practices among the welds in auxiliary piping systems.

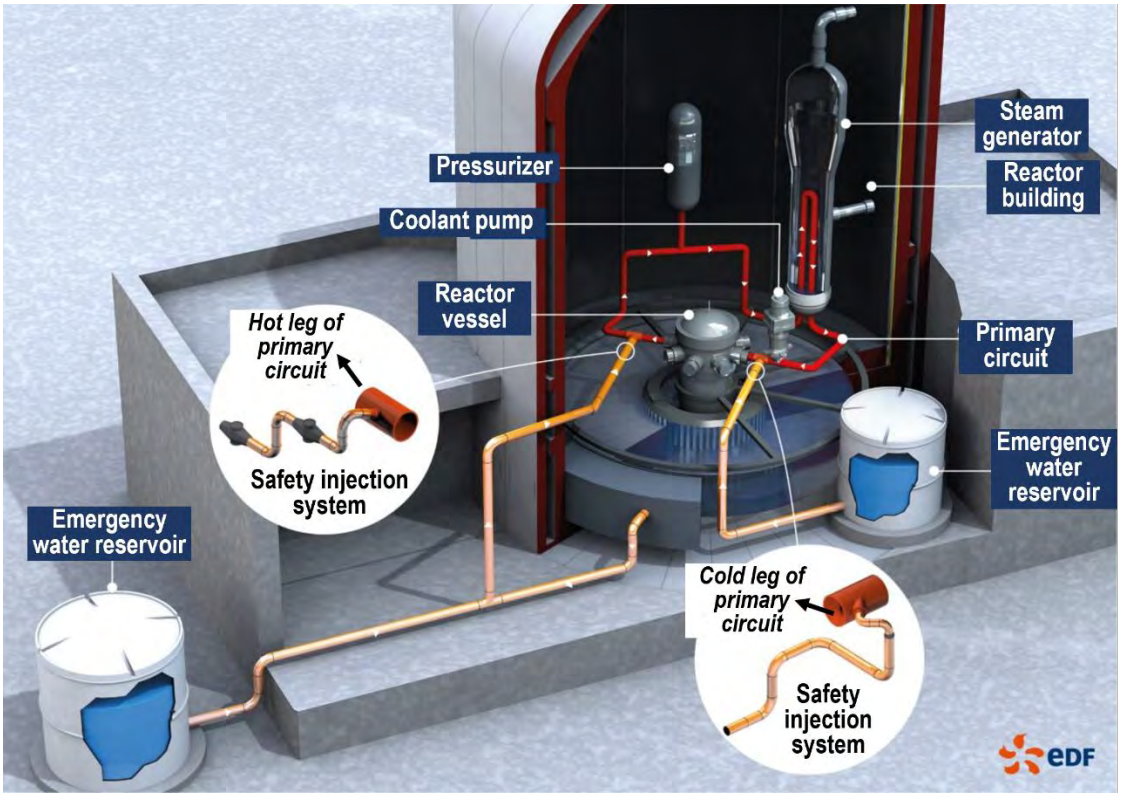

Figure 1. Illustration of the safety injection system location in the French N4 PWR design, redacted for English based on [11].

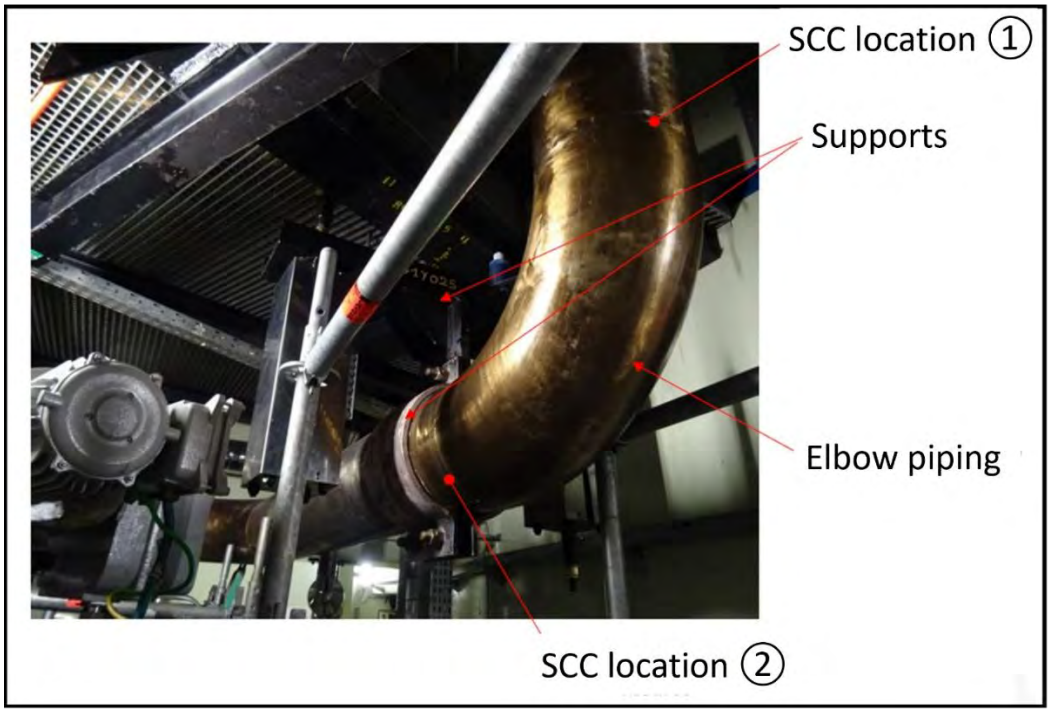

Figure 2. Photo of the actual elbow piping in a cold leg of the safety injection lines in Civaux-1 where the first SCC incidents were reported [12].

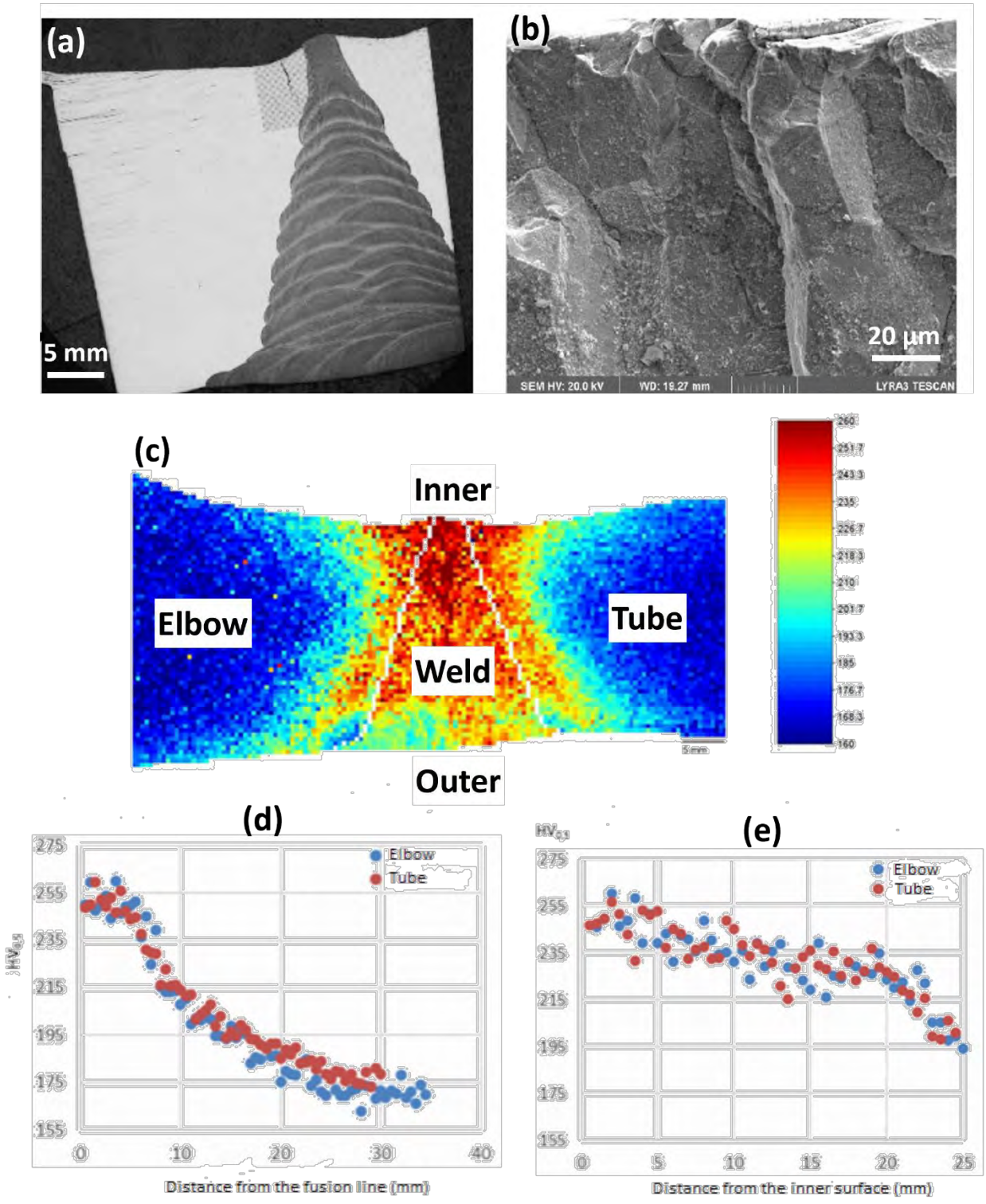

Figure 3. (a, b) Destructive examination and (c–e) hardness measurements of a cross-section containing the SCC crack found in location ① in Figure 2 [8].

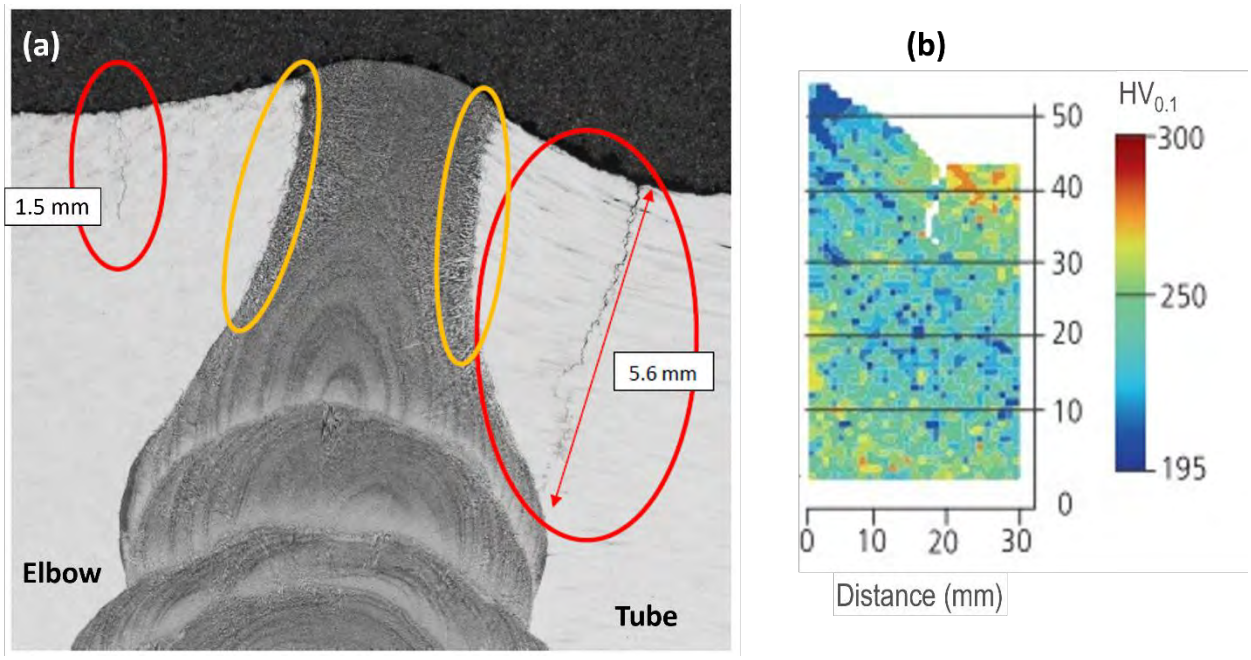

Figure 4. (a) Destructive examination of a cross-section containing the SCC cracks found in location ② in Figure 2, and (b) hardness map including part of the weld, HAZ, and base metal of the tube side. The location where the 5.6 mm-long crack is marked in (a) appears to coincide with the high-hardness area measured near the inner surface [13].

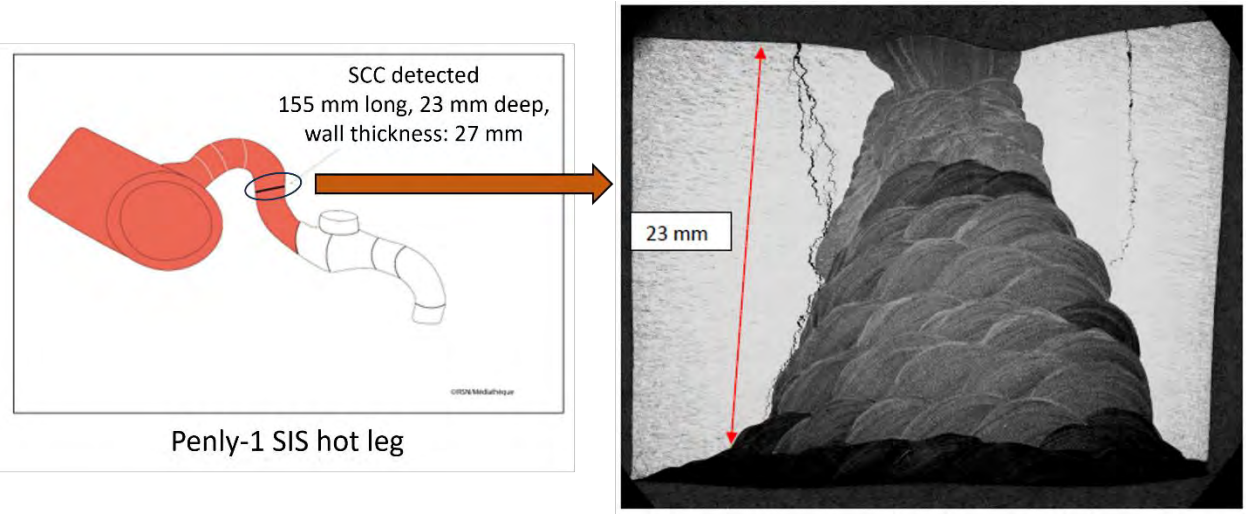

Figure 5. The longest SCC reported to date in all French PWRs. It was located in the HAZ of a weld joint in a hot leg of the safety injection system in Penly-1 (left) [5]. A micrograph of its morphology in the cross-section is also provided [14].

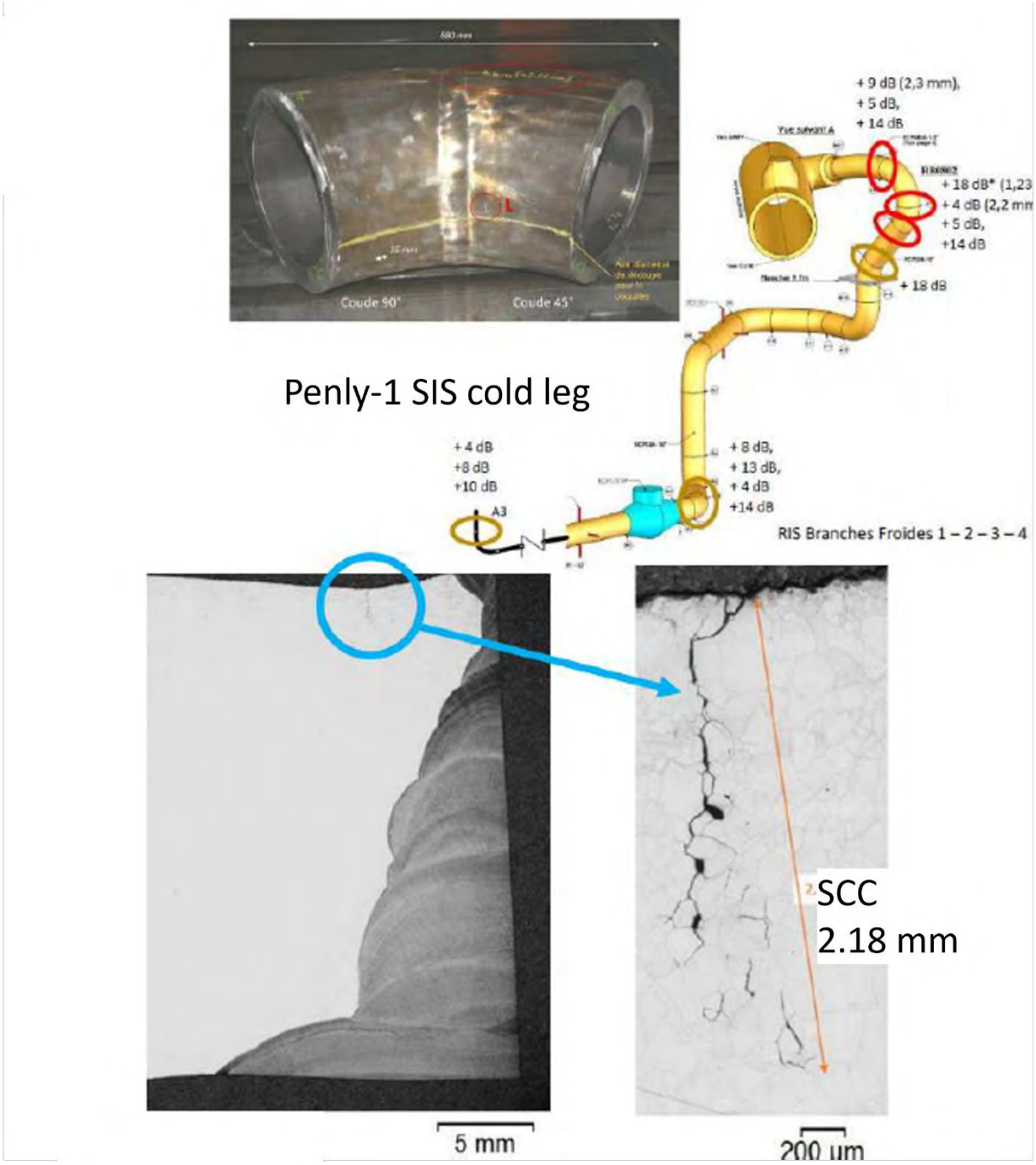

Figure 6. Example of destructive examination confirming the existence of SCC after defect indications were detected by ultrasonic technique in an elbow weld of a cold leg of the SI line in Penly-1 [15].

To date, additional inspections and investigations are still ongoing at EdF. Between the end of 2021 and June 2025, around 1000 welds from the SS auxiliary piping systems were inspected using non-destructive examinations across many French PWR units. The inspection used a new ultrasonic technique developed specifically for IGSCC detection and sizing, and ~300 welds were removed for laboratory examination. Figure 7 provides a summary of the frequency distribution of the examined IGSCCs as a function of their measured depth. A total of 172 IGSCC cases were summarized in this plot. It is worth noting that before the year 2020, a total of ~180 SCC events were reported worldwide on austenitic

stainless steels exposed to primary water environments in PWRs. The majority of the events (~84%) occurred in low-flow regions or occluded/stagnant primary water conditions. In two years, the newly detected SCC cases in French PWRs alone have exceeded the number of the total cases reported over the last 30 years worldwide, and all in PWR primary water at or below 300°C with potential presence of vortex flow.

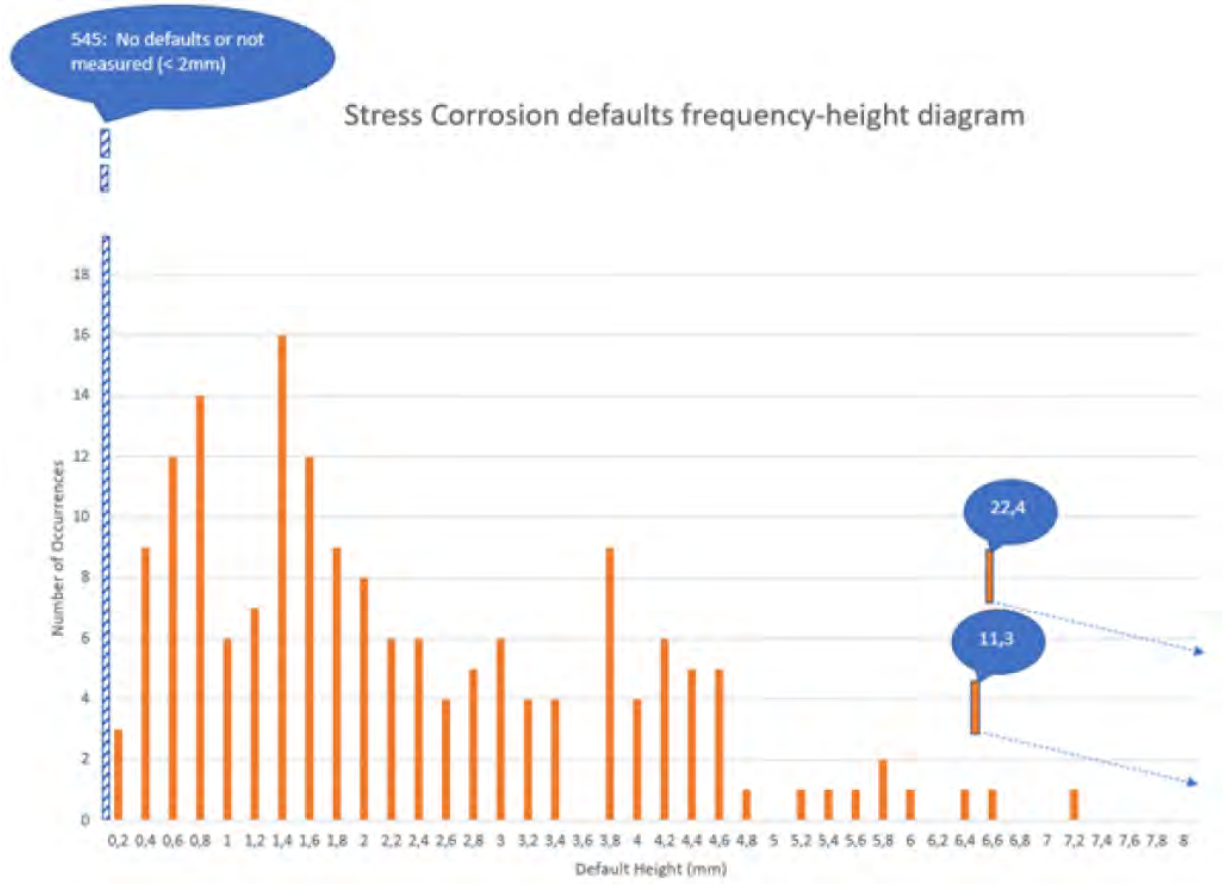

Figure 7. Distribution of IGSCC cracks depth (in mm) on emergency core cooling systems and RHR system welds examined between the end of 2021 and the beginning of 2023 in French PWRs [14].

As shown in Figure 7, most of these detected IGSCC remained shallow, with only two cracks exceeding a depth of 10 mm, and another nine cases exhibiting IGSCC cracks between 5 to 10 mm deep. Both welds made of 304L and 316L exhibited cracks. According to the manufacturing reports, various types of welding methods were used on the welds with IGSCC cracks including automated or tungsten inert gas welding, shielded metal arc welding, or flux welding. On some welds, a combination of these methods was used [14]. No specific welding method was found to be the most susceptible to SCC, but there are indications that automated process tends to create deeper cracks [16]. The fact that the cracks did not grow deeper is likely associated with decreasing weld residual stress from inner surface to the outer surface. However, questions remain on the cause of the initiation of these SCC cracks. According to the Autorité de Sûreté Nucléaire (ASN), elevated stresses caused by cyclic loading due to thermal stratification are suspected to be the primary contributor [2], followed by weld residual stress and potentially elevated oxygen due to dissolved oxygen in make-up water [17].

Statistics have shown that the pipes with the highest number of IGSCC cracks have a specific geometry that allows the thermal stratification phenomenon to occur, as illustrated in Figure 8. The water

circulation within the main primary pipes generates a vortex that penetrates into the auxiliary pipe. The water in the auxiliary pipe is, therefore, at the same temperature as the main primary pipes in the length that is penetrated by the vortex. If the vortex ends up in a horizontal part of the pipe, there is a superposition of a cold and a hot water layer inducing a bending stress. This additional stress in operation resulting from thermal stratification can likely explain the higher susceptibility of some particular pipe designs to IGSCC or fatigue cracks [14]. Another indirect evidence of the key role of thermal stratification is that the SCC occurrence has a strong dependence on reactor types. As shown in Table 1, the CP-type reactors and P4-type reactors have shown limited or no susceptibility to IGSCC due to the different geometry of the SI and RHR lines. The thermal stratification phenomenon is also relevant to the U.S. PWR fleet. The Pressurized Water Reactor Owners Group (PWROG) has reviewed the fleet branch piping configurations and identified those that meet the EDF criteria for susceptibility to thermal stratification. While such configurations are rare in SI piping, they are common for RHR suction piping. Thermal fatigue cracks are a known issue in such configurations and corresponding inspection procedure is in place, with no IGSCC cases reported to date.

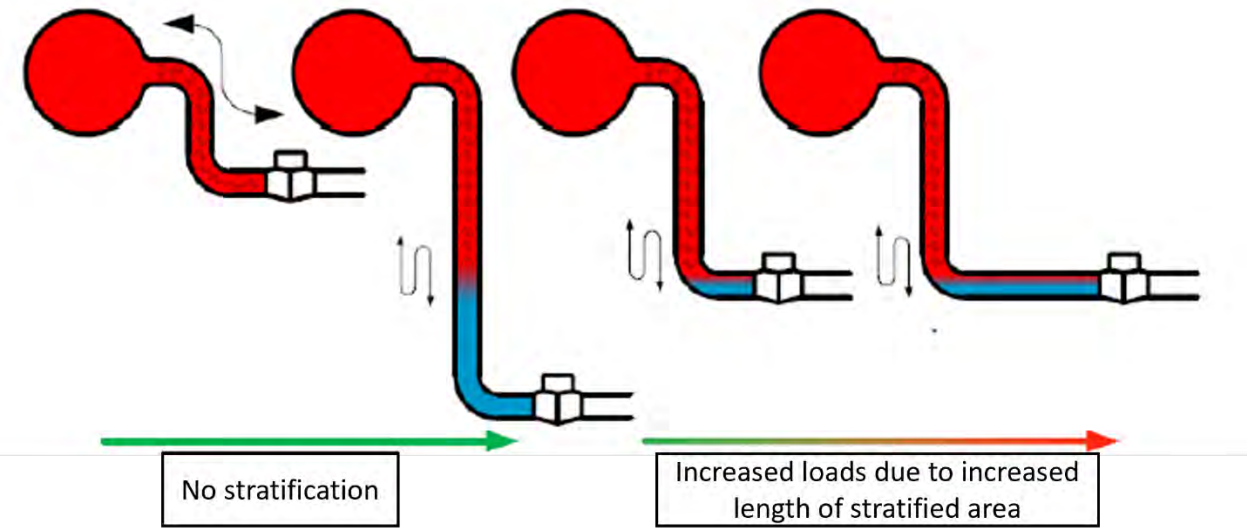

Figure 8. Illustration from EdF showing the effect of an auxiliary pipe design on thermal stratification [14].

Table 1. The systems and portions of their piping that were found sensitive to SCC on the PWR reactors of the French fleet [7].

Reactor System	**N4-type 1450 MW (4 reactors)**	**P'4-type 1300 MW (12 reactors)**	**P4-type 1300 MW (8 reactors)**	**CP0 and CP1-type 900 MW (32 reactors)**
Safety injection system	Lines connected to the cold leg of the primary loop	Lines connected to the cold leg of the primary loop	/	/
Residual heat removal system	Lines connected to the hot leg of the primary loop	/	/	/

However, there are cases where deep IGSCC was developed in absence of thermal stratification effect, such as the one reported in Penly-1 (Figure 5). In addition, it is interesting to note that many more IGSCC cases were found in lines connected to the cold leg than to the hot leg of the primary loop (Table 1), where the temperature is lower. Combined with the fact that the HAZ regions where the IGSCC occurred usually exhibit moderate hardness values lower than 300 HV (Figures 3 and 4), it is possible that other factors may have played a non-trivial role in causing SCC initiation to happen in these welds. The ASN suspects that DO in the primary water may have contributed to the observed SCC cases because there is a growing practice at EdF not to deaerate the make-up water tanks connected to the primary circuits, making it possible to have aerated water entering safety injection systems, resulting in discontinuous oxygen ingress. The scenarios, however, are very complicated and only postulated. Depending on the geometry of the piping, there are cases where aerated make-up water is injected only meters upstream, leaving only a fraction of a second for mixing before reaching the regions where SCC was reported thus extremely short oxygen transients. There is also the possibility of non-homogeneous mixing when a slug of cold water is injected into a hotter flowing stream leading to thermal stratification with examples shown in Figure 8, providing longer transients for oxygen ingress. Besides these scenarios, occluded crevice, if present, can also trap oxygen and lead to high local DO concentration. Fundamental studies have shown that aerated transient with air-saturated water can lead to non-reversible modification of oxides formed in nominal water [18], but its impact on SCC initiation in realistic operating conditions remains to be investigated. Some laboratory testing data is available on the effect of DO on SCC propagation in austenitic stainless steels, showing the presence of oxygen greatly accelerating the SCC crack growth rates of 304/316 in PWR primary water [19, 20]. However, similar evaluations are non-existent on the effect of DO on SCC initiation due to the known challenge in producing SCC initiation at constant load on Type 304/316 stainless steels in PWR primary water.

2.2 Key Knowledge and Technical Gaps

Based on the information collected on the operational experience of stainless steel SCC in PWR primary water and the literature review performed last year [3], high-quality SCC initiation data remains scarce to clarify the SCC initiation mechanism of Type 304/316 stainless steels in PWR primary water. Existing laboratory data were mostly obtained using testing conditions far from realistic service conditions and cannot be directly used to inform proactive material degradation management. Key knowledge/technical gaps have been identified as follows:

- There is a lack of fundamental understanding of the factors responsible for SCC initiation and the development of very shallow surface cracks into deep propagating cracks. There is also a lack of quantifiable relationships between the influencing factors and SCC initiation time/susceptibility. For example, although field experience and literature data suggest cold work could accelerate SCC initiation, there is little information about threshold yield strength and hardness values required for SCC initiation in PWR primary water under free-flowing conditions. The same issues exist for dissolved oxygen content. The dependency of SCC initiation on temperature is largely unexplored. The contribution of loading conditions to SCC initiation kinetics and mechanism is poorly understood. Heat-to-heat variability is another topic that may have been overlooked. In addition, the synergism between the influencing factors remains to be studied.
- There is a lack of suitable SCC initiation testing techniques that could effectively produce high-quality, reproducible SCC initiation data to be directly used to inform industry practice. At the same time, susceptibility map already exists for SCC propagation in PWR primary water [21] and for SCC initiation in BWR normal water chemistry [22]. Most of the existing body of SCC initiation data in PWR primary water is produced by SSRT using severe loading and excessive cold working that are difficult to relate to plant applications.

- There is a lack of statistically relevant SCC initiation data of austenitic SS in PWR primary water. Such data would be highly desired for industry to develop meaningful predictions on SCC initiation time/likelihood to guide inspection and maintenance strategy development.

To address these gaps, a research plan has been devised in FY 2024 based on updated information collected on the French NPP stainless steel auxiliary piping SCC experience and feedback from industry and the SCC research community. The objective of the research project is twofold: (1) To support the cause analysis of recent auxiliary piping SCC incidents reported in French NPPs focusing on knowledge gaps on environmental factors (i.e., dissolved oxygen and temperature); (2) To assess the potential relevance of the French NPP auxiliary piping SCC cases to the U.S. nuclear industry. FY 2025 marks the second year of the research effort in this area with a focus on the continued evaluation of the effect of DO on SCC initiation of cold forged (CF) 304L in PWR primary water. CF 316L materials were also fully characterized this year in preparation for their SCC initiation testing planned to start at the beginning of FY 2026. The research progress made to date on these topics will be summarized in detail in the following chapters.

3. Materials Information

3.1 Heat Selection

The typical grades for auxiliary stainless steel in the U.S. fleet are 304, 304L, 316, and 316L. A survey of PWROG fleet of 55 units found no cases of 316LN grades being used [23]. To assess the potential relevance of French NPP auxiliary piping SCC incidents to U.S. nuclear industry, 304L and 316L were selected as testing materials for this study. One heat was purchased each for a dual-certified 304/304L and 316/316L (denoted as 304L and 316L hereafter) in the plate form with a thickness of 6.35 mm (2.5 inches). This thickness was selected to enable 0.5”-thick compact tension specimens being extracted in the S-L, S-T, L-S, and T-S orientations as shown in Figure 9 after being forged up to 50% reduction in thickness, which is likely needed to produce materials with high hardness matching the threshold of 300 HV reported for SCC to occur in service in non-contaminated PWR primary water [9].

Certified mill test reports were obtained on multiple heats for selection, and the final choice was made based on a balance of desired composition (higher carbon, higher nitrogen, lower sulfur, lower molybdenum, and lower copper) and mechanical properties (higher strength) that are known to increase SCC susceptibility. The basic information and composition of the two purchased heats are listed in Tables 2 and 3, respectively.

Table 2. Basic materials information of the purchased 304L and 316L heats.

Material	Heat No.	Form	Heat treatment condition	Yield Strength at Room Temperature (MPa)
304/304L	530059	2.5” thick plate	Solution annealed at 1050°C and quenched in water	295
316/316L	Y35Y	2.5” thick plate	Solution annealed at 1038°C and quenched in water	272

Table 3. Chemical composition of the purchased 304L and 316L heats.

Heat # / Weight (wt%)	530059 (304/304L)	Y35Y (316/316L)
C	0.017	0.021
Si	0.32	0.423
Mn	1.2	1.187
P	0.031	0.033
S	0.001	0.001
Cr	18.23	16.600
Ni	8.02	10.035
Mo	0.56	2.017
Cu	0.38	0.431
N	0.07	0.056
Co		0.275

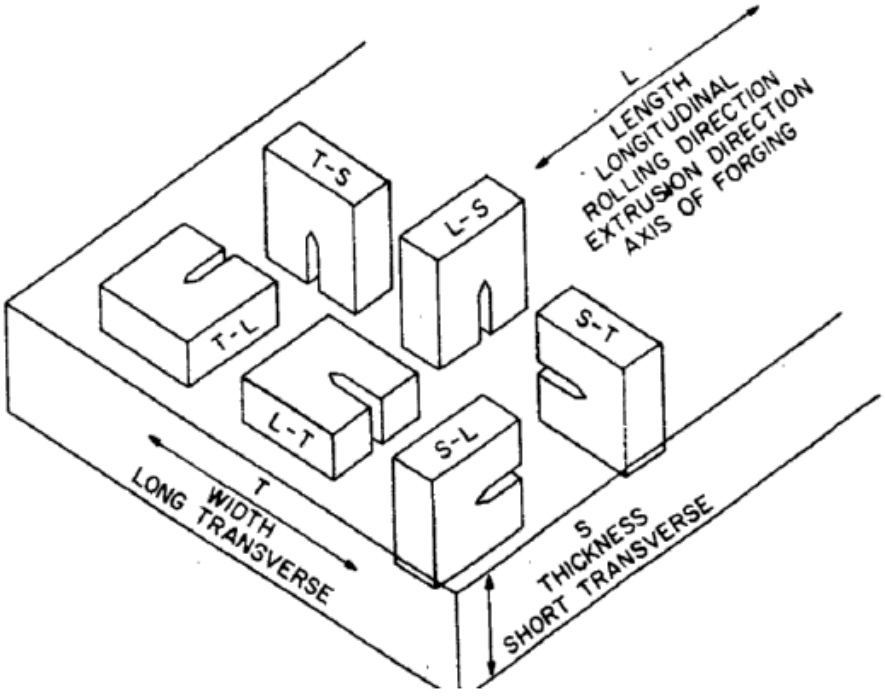

Figure 9. Specimen orientation for a plate product form [24].

3.2 Cold Forging Procedure

To evaluate the effect of cold work on materials' SCC initiation susceptibility, and to produce materials that match the high hardness values (~300 HV) reported on SS components where SCC incidents were detected in service, it was decided to cold forge the 304L and 316L materials to various

cold work levels for this study. While the microstructures produced by cold forging may not be fully representative of those of the HAZ in an actual weld, it provided a cost-effective way to identify the appropriate combination of oxygen content, loading conditions, and strain paths to produce SCC initiation in SS materials in a realistic time frame, which is also a critical goal of the first phase of this study.

As shown in Figure 10, four blocks of ~ L3.5" × W3" × T2.5" were prepared for 304L and 316L to be cold forged to 10%, 20%, 30%, and 40% reduction in thickness. The blocks to be cold forged to 30% and 40% reduction in thickness were further cut into half to facilitate the forging. The cold forging was performed at General Electric Global Research Center (GEGRC). To avoid strain-induced martensite formation during cold forging, the blocks were preheated in a furnace for several hours or overnight to reach a uniform temperature of ~210°C. To achieve this, the blocks were placed on an alumina base, which was linked to a thermal couple. The temperature on the thermal couple only varied from 207–210°C over the entire preheating duration. The forging was conducted immediately after the blocks were removed from the furnace. A photo of the post-forged 304L blocks is provided in Figure 11.

The testing effort started in FY 2024 focused on 304L, with preparation of 316L specimens completed in FY 2025. For the first series of tests, four blunt notch compact tension (BNCT) specimens and two cylindrical tensile specimens were machined from the 304L and 316L blocks in each cold forged condition. The tensile specimens were prepared for tensile testing to obtain yield strength (YS) of these cold forged materials at 300°C (i.e., SCC initiation testing temperature). The BNCT specimens were prepared for SCC initiation testing. The reason behind the selection of this geometry for testing will be discussed later in Section 4.1.1. As shown in Figure 12, the tensile and BNCT specimens were all prepared in the L-S orientation with respect to the rolling direction for the first phase testing because this orientation is coincident with the cracking path in actual welds in auxiliary SS piping in the French PWRs.

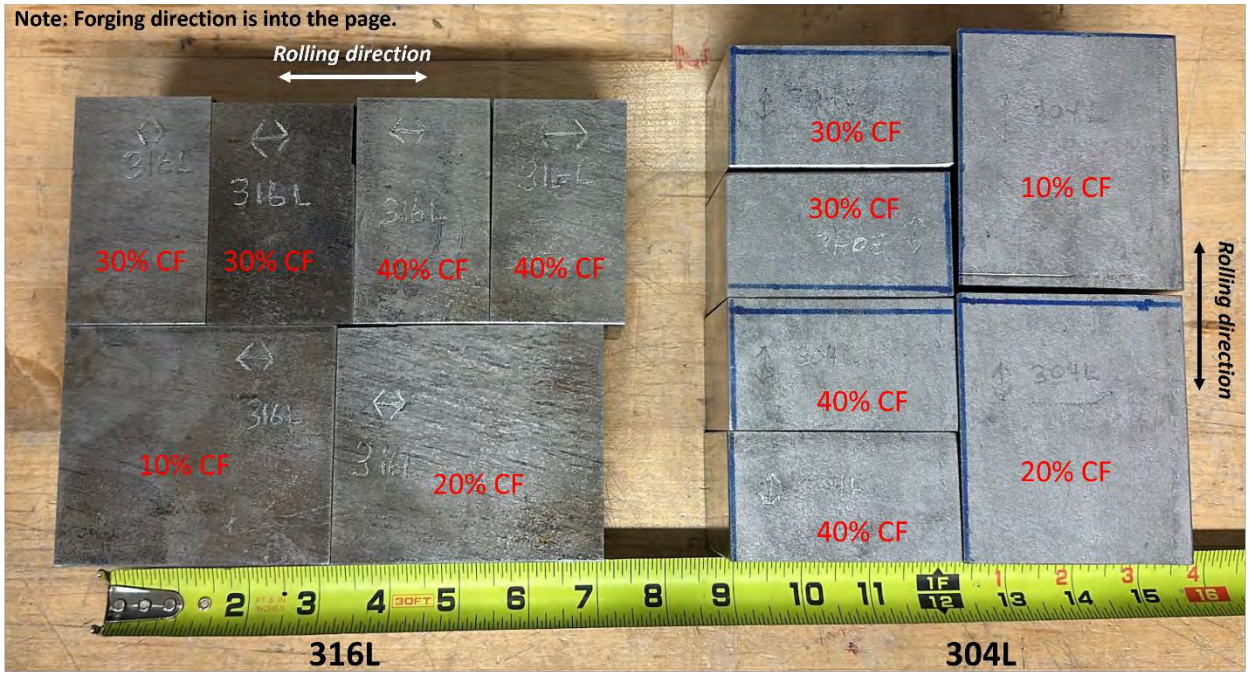

Figure 10. 304L and 316L blocks prepared for cold forging.

Figure 11. 304L blocks after being cold forged to 10–40% reduction in thickness. The forging direction is into the page.

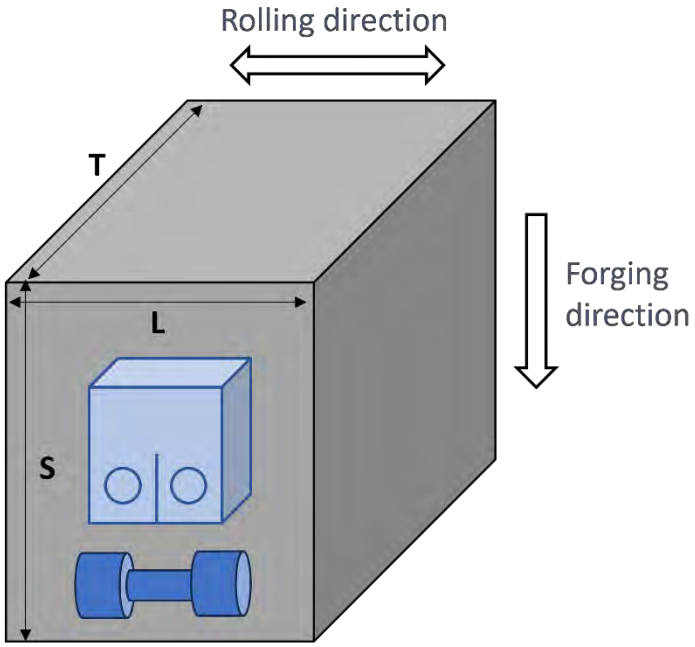

Figure 12. Schematic showing the specimen orientation with respect to the rolling direction of the as-received 304L and 316L plate materials and the direction of forging performed at GEGRC. L = longitudinal, T = transverse, and S = short transverse.

3.3 Materials Characterization

After the materials were cold forged, a ≥1/3-inch thick piece was taken off from one end of a block at each cold forged level and cut into three smaller samples for microstructural characterizations and hardness measurements. The LS, TS, and TL planes of the forged blocks were all sampled as indicated by the different colors in Figure 13a. The three samples from the same cold forged block were then mounted together in an epoxy base (Figure 13b) and prepared through standard metallographic procedures beginning with grinding using SiC pads of 220-1000 grit, followed by 6 µm and 1 µm diamond paste and 0.05 µm colloidal silica vibratory polish for high resolution microscopy characterizations and hardness measurement.

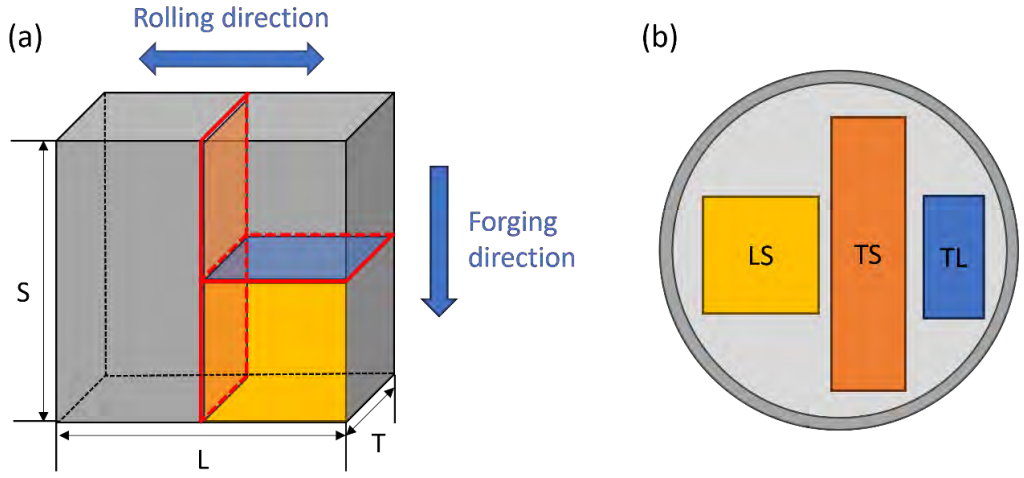

Figure 13. Schematic showing (a) the cutting plan of three samples from materials at each cold forged level and (b) their corresponding polishing planes in the epoxy mount.

3.3.1 304L General Microstructures

As the first step, a JEOL 7600F field emission scanning electron microscope (SEM) was used to document the materials' microstructures at each cold forged level in both secondary electron (SE) and backscattered electron (BSE) modes. Figure 14 displays the general microstructure observed in the 10, 20, 30, and 40% CF 304L materials, respectively. Strain contrast induced by cold work was observable and quantitative analysis results will be shown in Section 3.3.1.2. Randomly distributed darker stringers of 25–100 µm long are visible in all CF levels, which are confirmed as delta ferrites in the following energy dispersive spectroscopy (EDS) and electron backscatter diffraction (EBSD) analyses. High resolution examination found that there were often some micrometer- and sub-micrometer-sized, irregularly shaped secondary phase particles residing on the matrix-delta ferrite interfaces (Figure 15). Cracked precipitates and adjacent voids were also visible by the brighter edges revealed in these SE mode images (as highlighted by the red arrows). These damages are likely produced by cold forging and they share similar morphologies to those previously reported in thermally treated and cold forged Alloy 690 materials [25]. While no quantitative analysis was performed, these observations indicate that the degree of damage increases with the cold forge level, which is qualitatively demonstrated in these images. It is possible that these damages can act as stress concentrators, and there may be galvanic effects between the precipitates, delta ferrite, and matrix that can facilitate crack initiation at such sites. However, the density of these precipitates thus associated damage is very low, therefore unlikely to cause macroscopic SCC initiation even in the 40% CF specimens. Nevertheless, their impact on SCC initiation can only be confirmed by post-test examinations, and we will aim to obtain unambiguous evidence to prove/disprove the

hypothesis. In addition, increasing strains with the increase in cold forge level can also be viewed more clearly in these higher-magnification images.

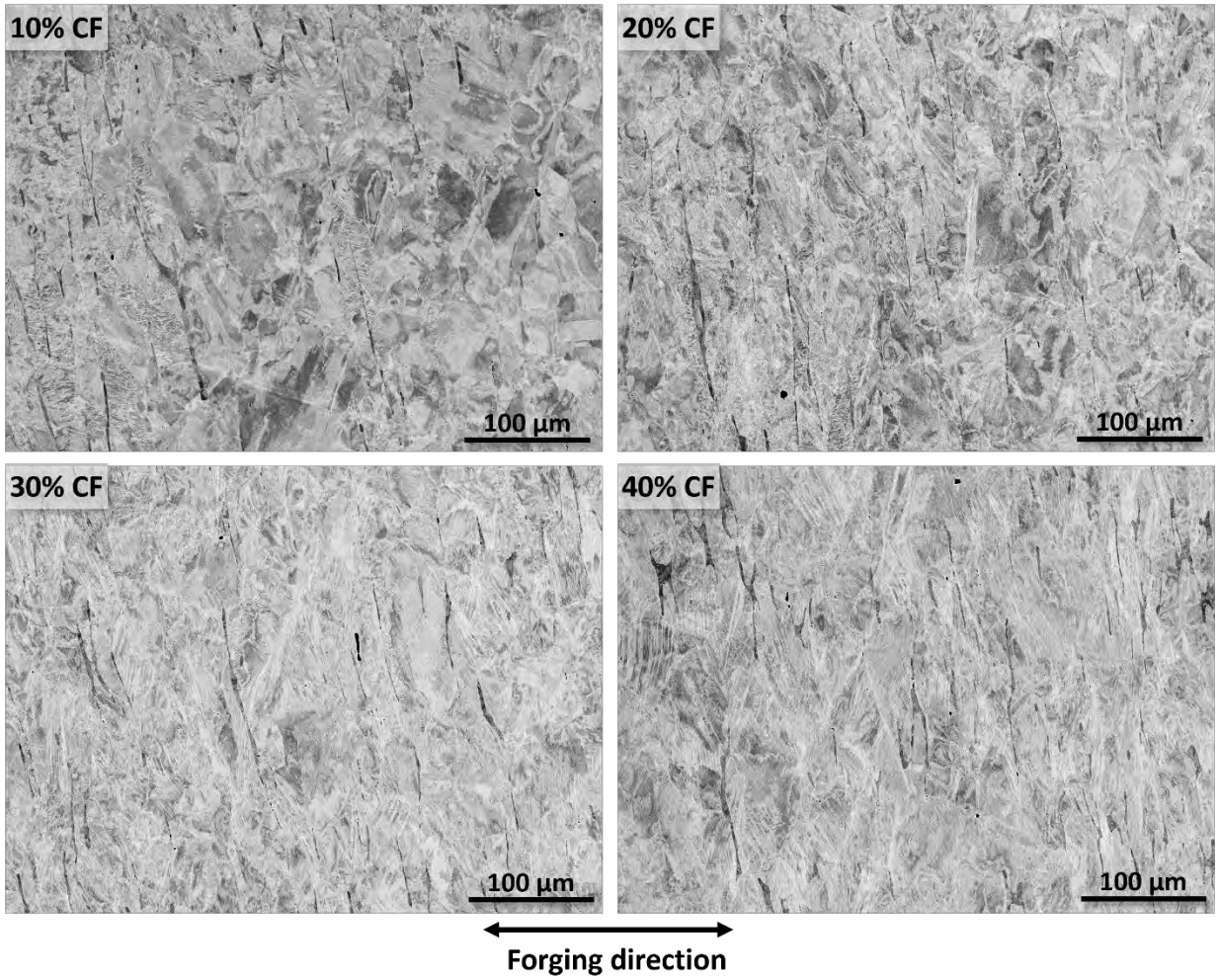

Figure 14. Representative SEM-BSE images of the microstructure in the TS plane of 304L cold forged to 10–40 % reduction in thickness.

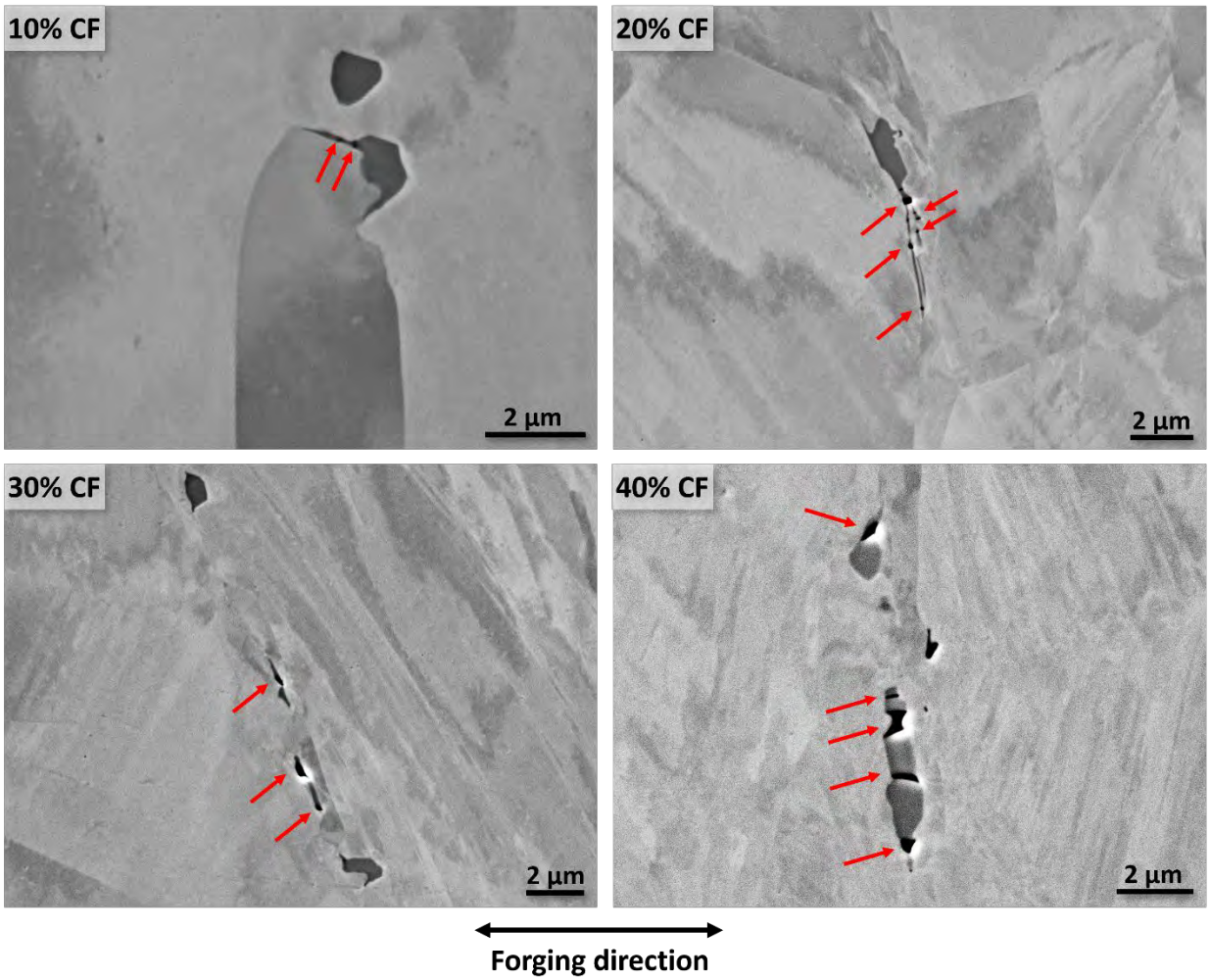

Figure 15. SEM-SE images of representative precipitates and cold forge-induced damage in the TS plane of the 10–40%CF 304L materials. Voids or cracks in precipitates produced by cold forging are highlighted with red arrows.

3.3.1.1 EDS Analysis

SEM-EDS analyses were performed first at low magnifications to obtain the general chemical composition of randomly selected sites in each cold forge level using a voltage of 20 keV. Figure 16 shows an example with selected elemental maps of an area documented in the TS plane in the 40%CF 304L material. The darker stringers revealed in the BSE image are high in Cr and low in Ni content, consistent with delta ferrite characteristics. In addition, enrichment of Cr, Al, and Ti were observed at certain spots, indicating secondary phases of different types.

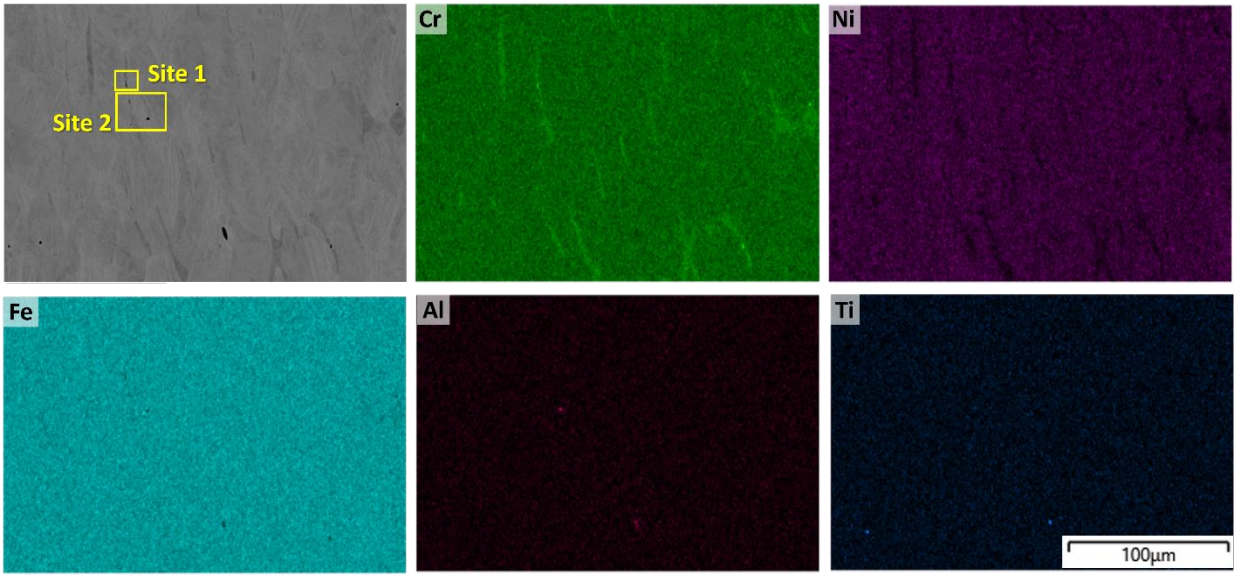

Figure 16. SEM-EDS elemental mapping of the general microstructure in the 40%CF 304L material (TS plane view).

SEM-EDS analyses were then performed at higher magnifications, focusing on obtaining chemical composition information on different types of secondary phases revealed in the low magnification maps. A lower voltage (10 keV) was used, taking advantage of the smaller interactive volume of the beam to obtain more accurate data on the precipitates found on the surface and on lighter elements. The results of the EDS analysis performed on the two sites selected in Figure 16 are shown in Figures 17 and 18, respectively. Site one features a few Cr-rich precipitates residing on the left side of a delta ferrite, where enrichment of silicon is found in the cracks in the lower precipitate, consistent with the colloidal silica suspension used at the final step of polishing. The irregularly shaped, darker, sub-micrometer-sized secondary phase residing on the right side of the delta ferrite features a more complex composition with Ti enriched in the needle-like strip immediately adjacent to the delta ferrite, while enrichment of Mn, S, and Al is found to the right of the Ti-enrichment in the lower rod-like portion, indicating a mix of titanium nitride and manganese sulfide inclusions. Site 2 also exhibits a few Cr-rich precipitates residing on the left side of a delta ferrite and an intragranular inclusion to the right of the delta ferrite. Figure 18 suggests this is a much bigger titanium aluminum nitride with titanium-rich outskirt wrapping an Al- and N-rich core.

Observations on 304L materials at other cold forged levels agree with the above findings. It can thus be summarized that at least three types of secondary phases are present in the 304L materials: Cr-rich precipitates, MnS inclusions, and TiN inclusions. The Cr-rich precipitates usually reside at the delta ferrite-matrix interfaces, while TiN have been observed at the delta ferrite-matrix interfaces and in the matrix. Since only one MnS was found by the limited EDS analyses performed, it is not possible to determine whether it has a favorable nucleation site. Since MnS is known to deteriorate the corrosion resistance of stainless steels and promote pitting especially in chloride-containing waters, it will be of interest to see if they can act as crack initiation site in oxygenated PWR primary water. More detailed examinations will be performed post-test to determine the extent of MnS distribution and their effects on SCC initiation of stainless steels.

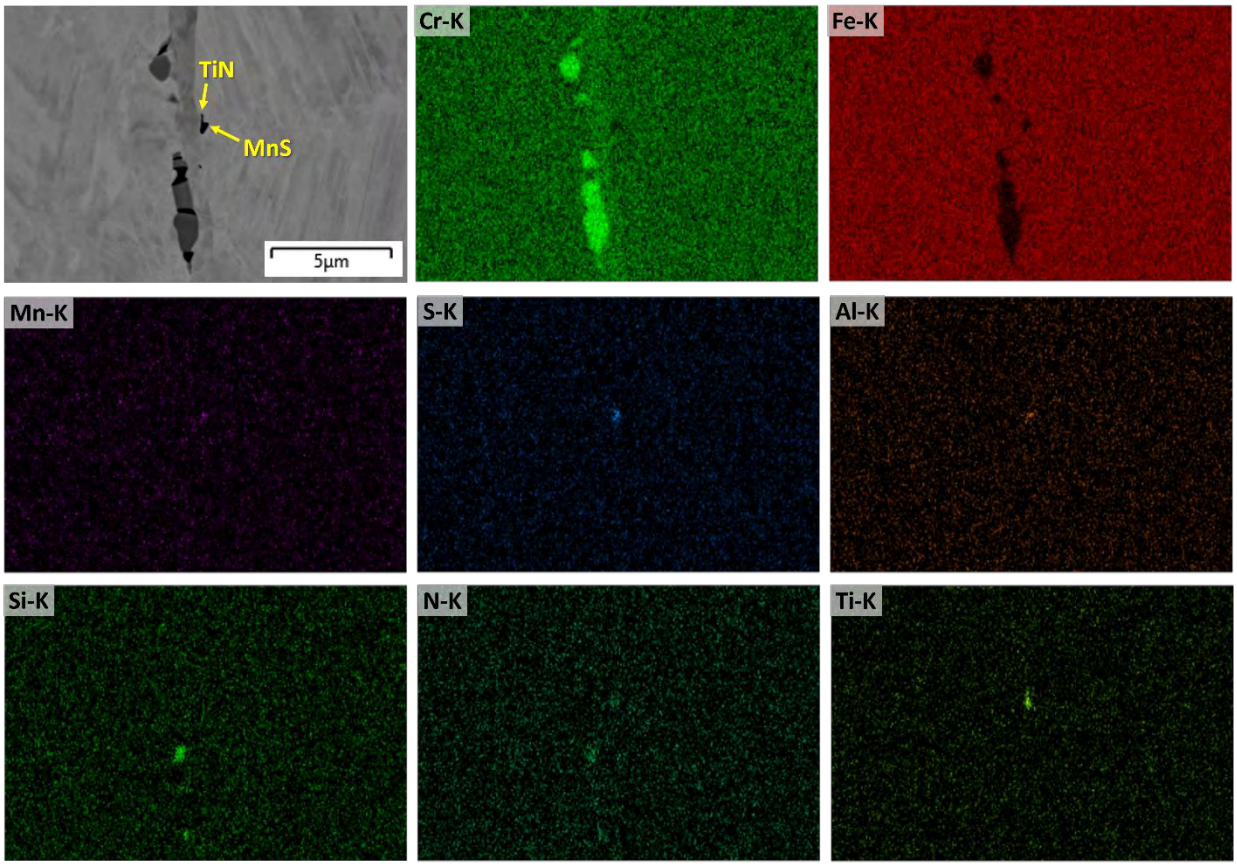

Figure 17. Qualitative SEM-EDS elemental mapping of precipitates found at Site 1 as highlighted in Figure 16 in the 40%CF 304L material.

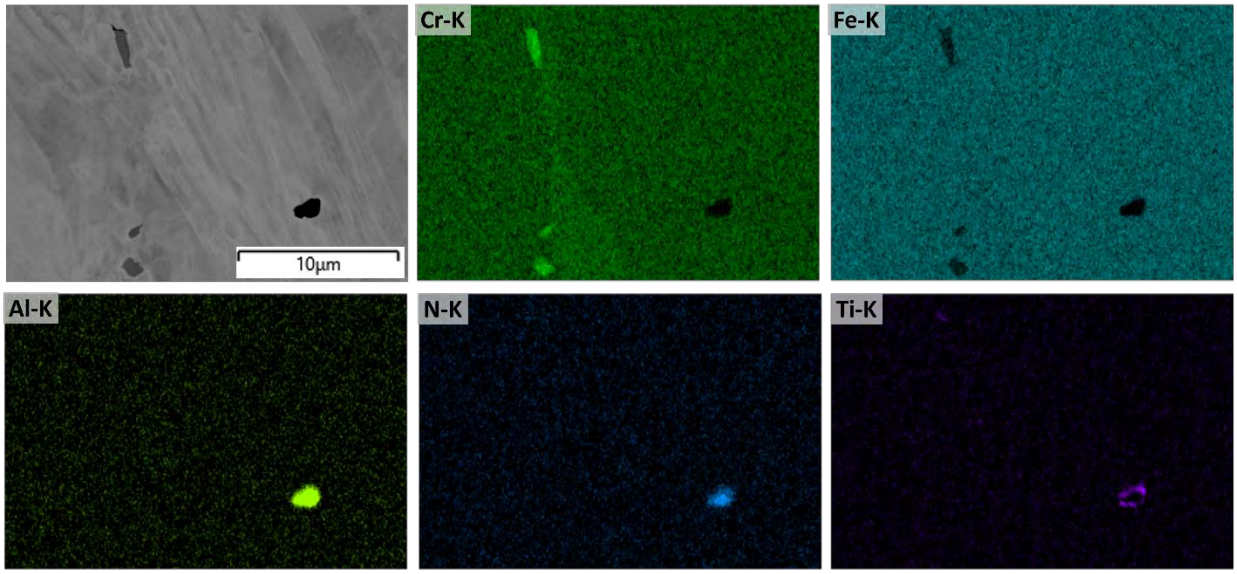

Figure 18. Qualitative SEM-EDS elemental mapping of precipitates found at Site 2 as highlighted in Figure 16 in the 40%CF 304L material.

3.3.1.2 EBSD Analysis

EBSD was performed to obtain crystallographic information of the cold forged blocks with a focus on the distribution of phases, local misorientations, and grain boundary types. A JEOL-IT800 FESEM equipped with an Oxford Instruments Symmetry detector was used. The imaging condition was 20 KeV at ~70° tilt and a working distance of ~25 mm. The EBSD focused on the middle sample shown in Figure 13b, i.e., the TS plane sample, of each cold forge level. Analysis was performed at four different magnifications, namely 100X, 250X, 400X and 2500X, using step sizes of 1 μm, 0.5 μm, 0.15 μm and 20 nm, respectively. Data cleanup was conducted using the Oxford's AZtecCrystal v3.1 software, first to remove mis-indexed electron backscatter patterns and then to perform an iterative zero solution extrapolation to a medium level. For highly strained samples (40% CF), additional data cleanup was done utilizing spherical harmonic indexing (MapSweeper) of diffraction patterns for particularly weak intensities. This allows for an increase in data for analysis and adequate comparison between the different forging levels.

Figures 19 summarizes the inverse pole figures, phase maps, kernel average misorientation (KAM) maps, and grain boundary type maps obtained at 400X magnification on the TS plane of 304L cold forged to 10, 20, 30, and 40% reduction in thickness, respectively. These maps provided information on the general microstructure of materials cold forged to the four different levels. The increase in cold forging level has resulted in a noticeable decrease in grain size and an increase in local misorientation. The local misorientation was mostly concentrated near grain boundaries in all cold forge conditions, while increased deformation inside grains was observed in highly CF materials, especially in the 40%CF condition. A small fraction of twin boundaries, mostly $\sum 3$ type boundaries, were seen through materials with different cold forge levels without obvious variation in density. Delta ferrites are present in materials in all cold forged conditions and their shape were obviously impacted by cold forging, with a trend of becoming narrower along the plane perpendicular to the forging direction and more fragmented as the forging level increases. The comparison of the phase maps and grain boundary type maps indicates that while some delta ferrites are present inside the grains, a much higher proportion is adjacent to high angle grain boundaries. Higher magnification EBSD maps were acquired at 2500X with refined step size and the results are summarized in Figure 20. The primary goal of these examinations is to confirm that martensite does not exist in these cold forged materials, as expected given the preheating conducted on these materials right before forging. The martensite phases were included for indexing, but the 10% and 20%CF showed no trace of these phases. In some of the higher CF samples, there were hints of some martensite phase near grain boundaries, but the data was sparse and not quantifiable. As a result, it can be concluded that the preheating performed before forging successfully prevented martensite from forming during cold forging. Even if martensite exists, they only occasionally present at discrete sites and, therefore, will have negligible impact on materials' mechanical properties and SCC resistance.

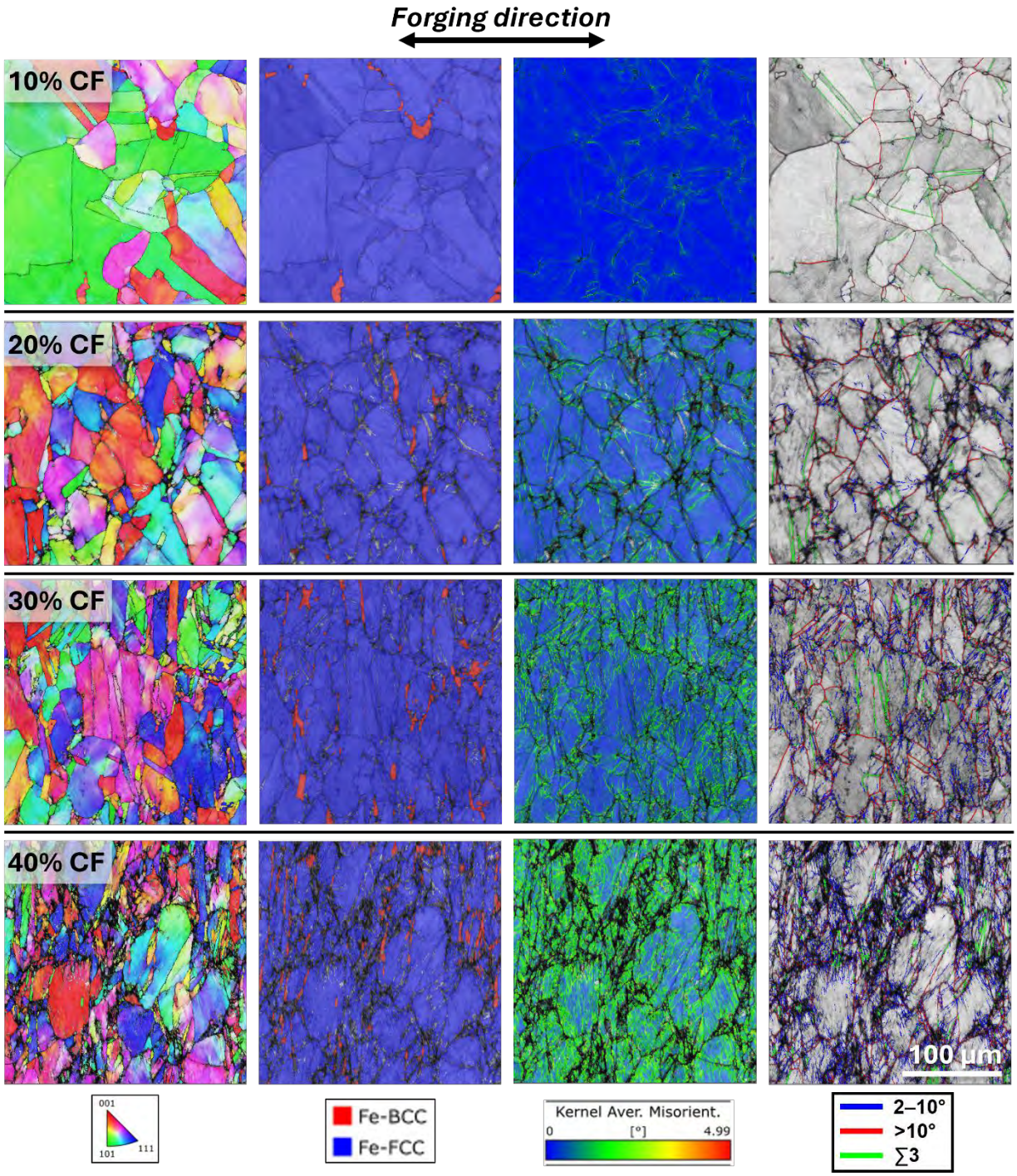

Figure 19. Comparison of EBSD maps taken at 400X on the TS plane of the 10, 20, 30, and 40%CF 304L materials. Columns from left to right are inverse pole figures, phase maps, KAM maps, and band contrast maps with GB types, respectively.

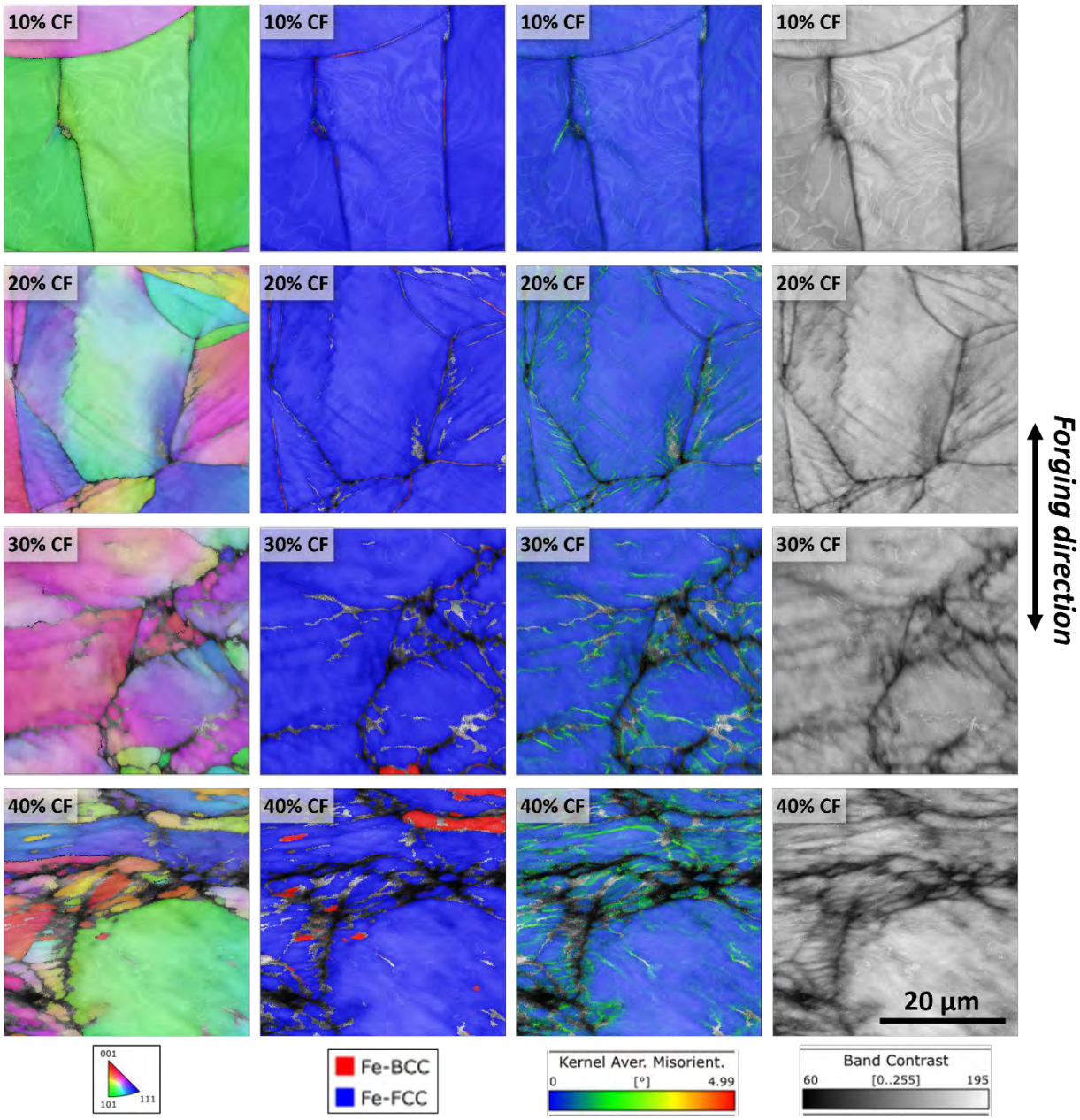

Figure 20. Comparison of EBSD maps taken at 2500X on the TS plane of the 10, 20, 30, and 40%CF 304L materials. Columns from left to right are inverse pole figures, phase maps, KAM maps, and band contrast maps, respectively.

3.3.2 316L General Microstructure

SEM examinations were also performed on the 316L materials that were cold forged to four different levels. Figures 21 and 22 present the general microstructure observed in the 10, 20, 30, and 40% CF 316L materials at magnifications of 250X and 500X, respectively. At 10% and 20% CF levels, the materials exhibit comparatively equiaxed grains with mild deformation-induced elongation. As the cold forging increased to 30% to 40% reduction in thickness, grain elongation in the deformation direction intensified, as well as the texture contrast within the grains, indicating increased strain accumulation with the increase in cold work level. A series of dark-contrast stringers, confirmed as delta ferrite in the subsequent EDS and EBSD analysis, were also present in the 316L materials. They are generally smaller and shorter than those observed in 304L (Figure 14), and became more visible in the SEM-BSE images after the magnification was increased to 500X (Figure 22). Interestingly, a great number of these ferrites were accentuated with a series of bright-contrast precipitates around their periphery at all cold work levels. Some of these precipitates have cracks or voids in them, which were likely induced during the cold forging process (Figure 23 Sites B and C, and Figure 24 a2, a3, b2, c1, and c3), but no consistent relationship was found between the degree of damage in the precipitates and the cold work level from the limited observations. In addition, darker, nanometer-sized particles were occasionally seen to be present inside delta ferrites or along the ferrite-matrix interface, as shown in Figure 24 a1, b1, b2, c1, and c2.

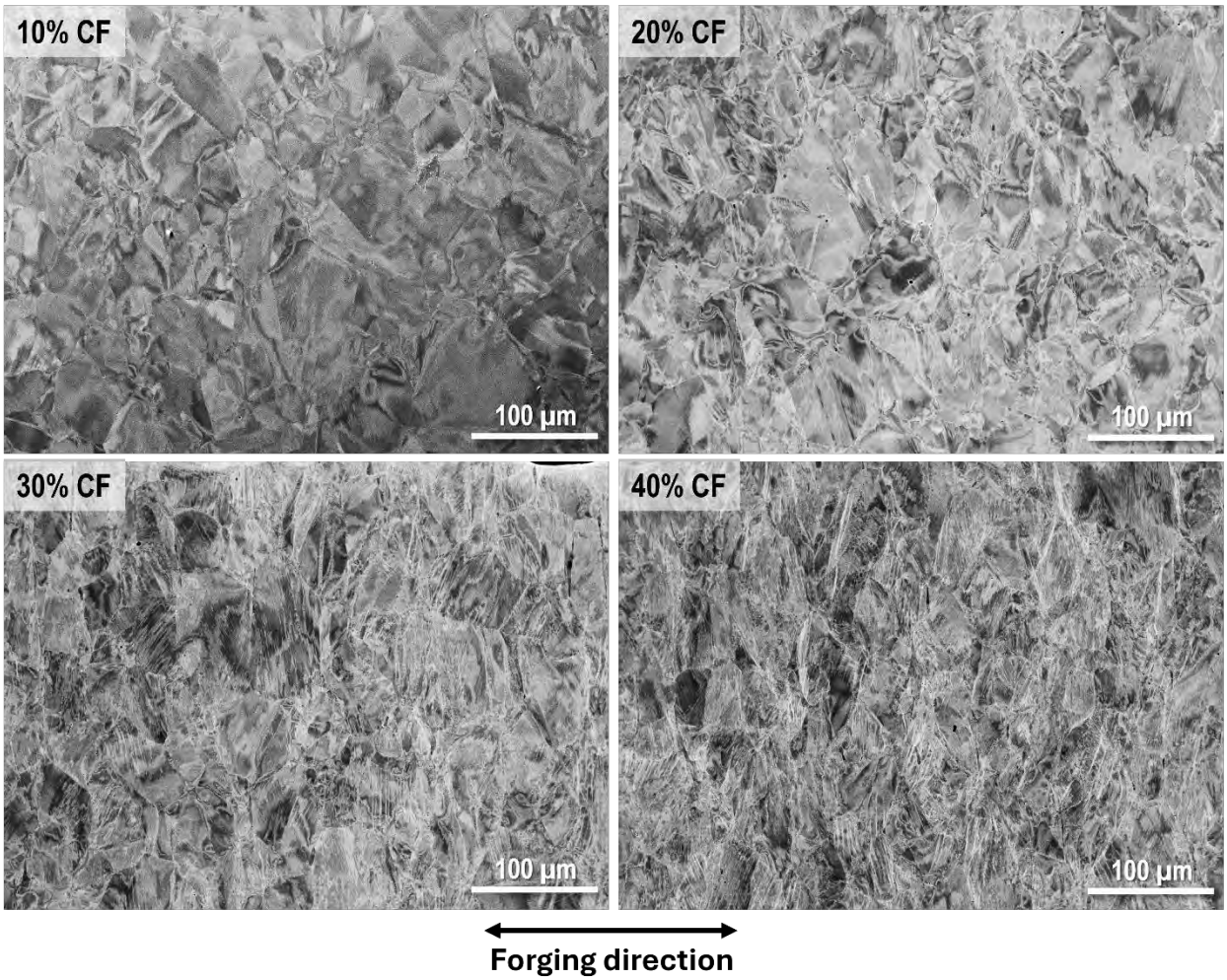

Figure 21. Representative SEM-BSE images of the microstructure in the TS plane of 316L cold forged to 10–40% reduction in thickness at 250X.

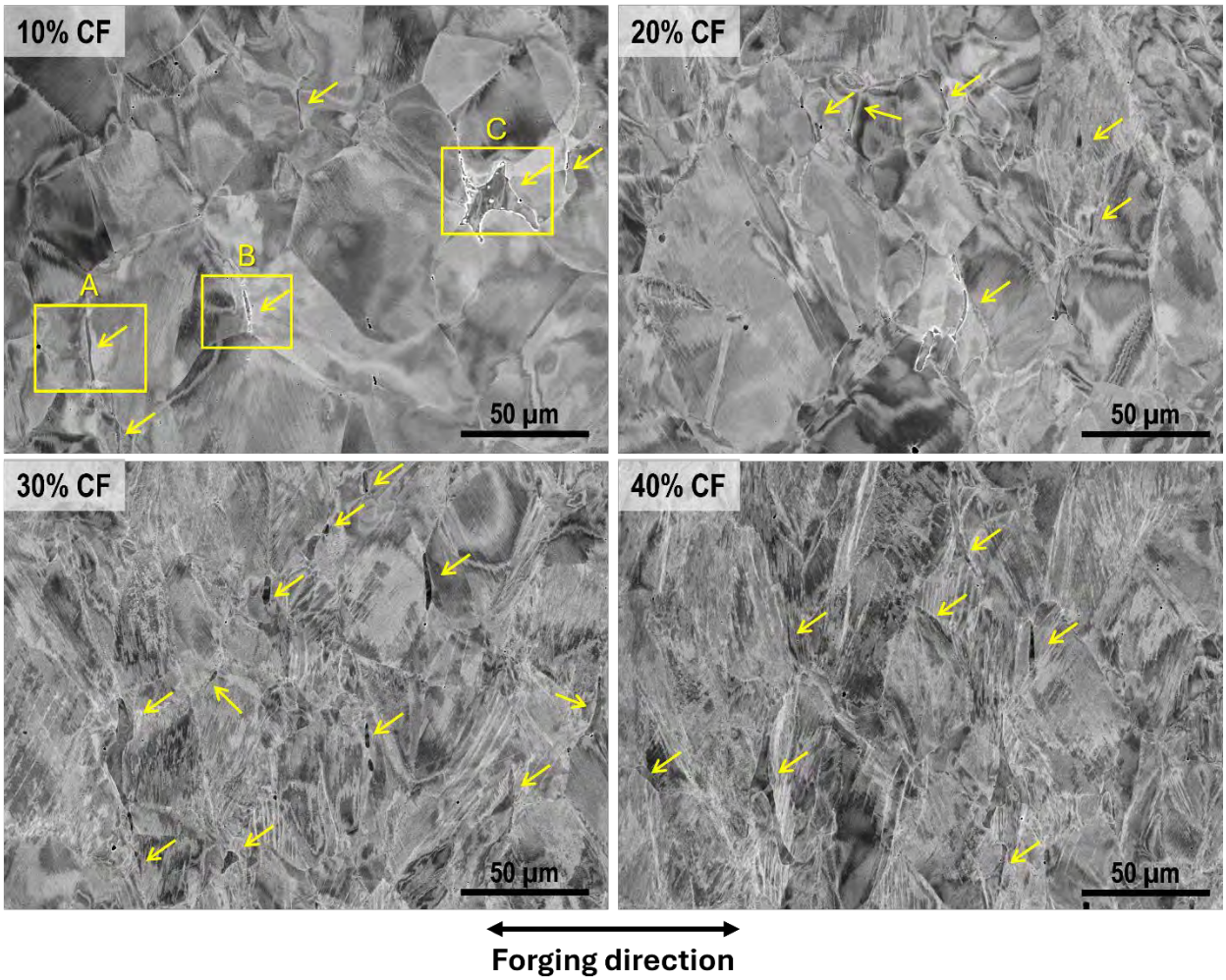

Figure 22. Representative SEM-BSE images of the microstructure in the TS plane of 316L cold forged to 10–40% reduction in thickness at 500X, where delta ferrites are highlighted with arrows.

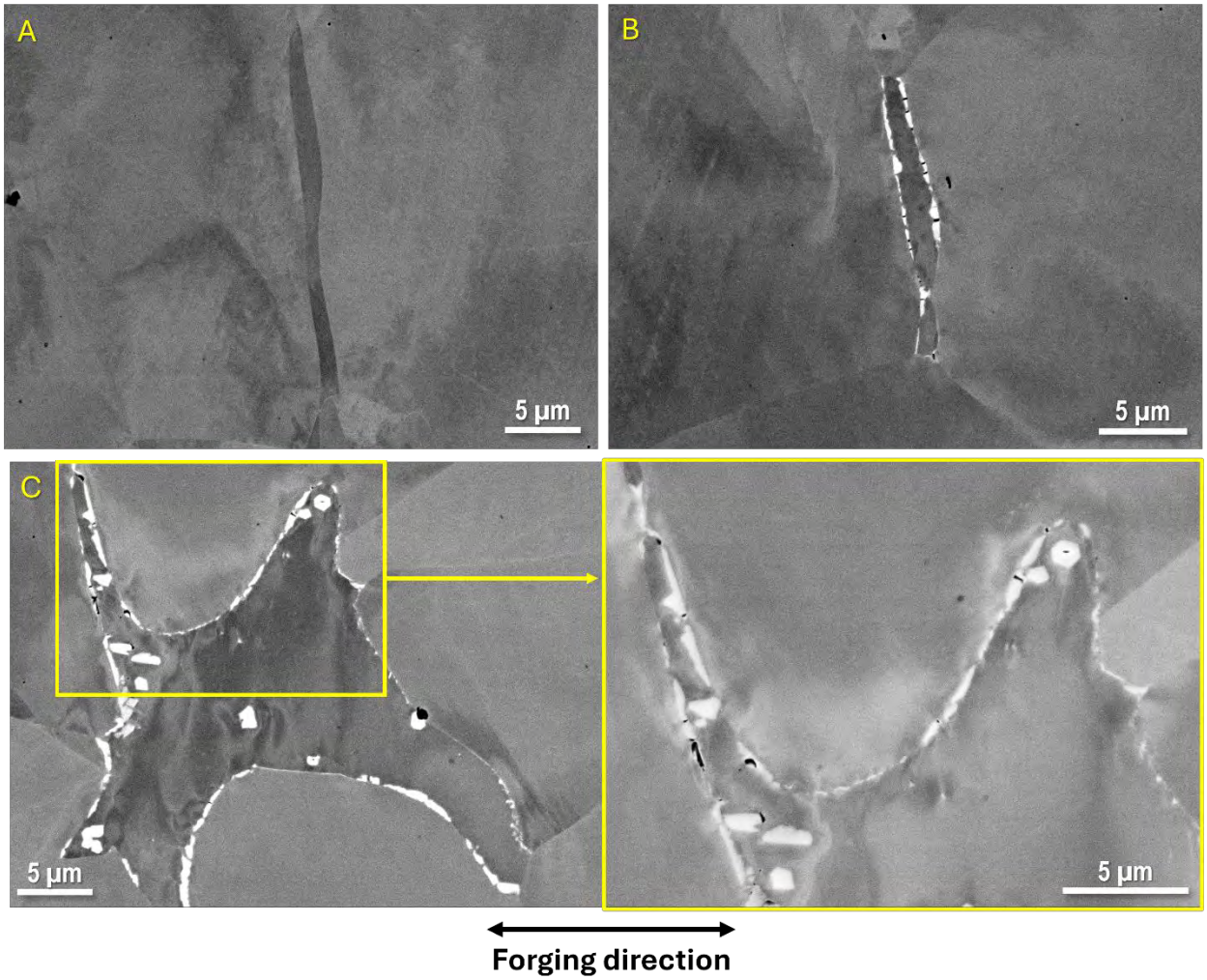

Figure 23. SEM-BSE images of the delta ferrite morphology observed in sites A – C marked in Figure 22 in the 10% CF 316L material.

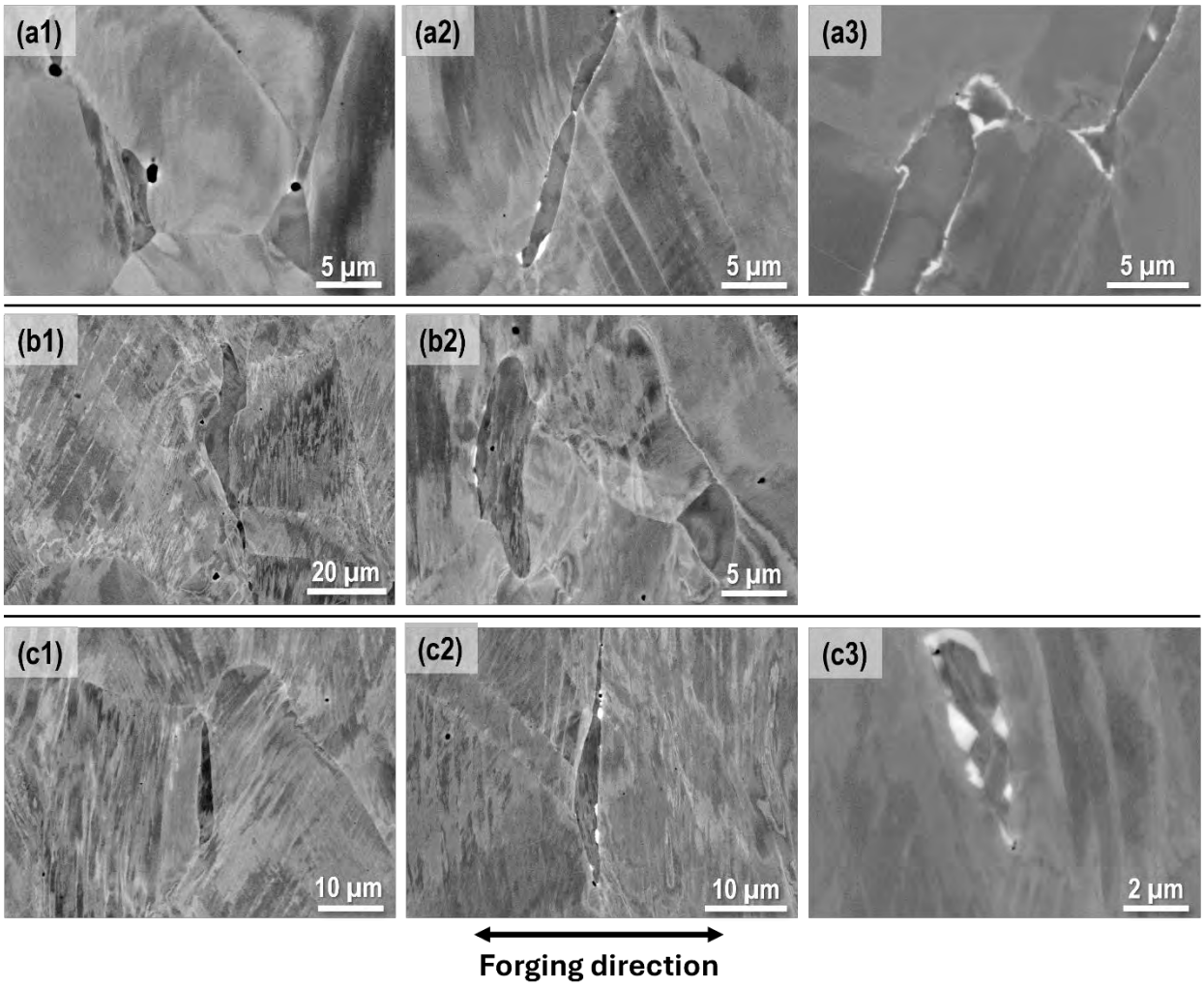

Figure 24. SEM-BSE images of the delta ferrite morphology observed in the 20% CF (a1–a3), 30% CF (b1 and b2), and 40% CF (c1–c3) 316L materials.

3.3.2.1 EDS Analysis

EDS analyses were performed on cold forged 316L materials first to confirm the composition of the dark-contrast stringers observed in the SEM-BSE images. Presented in Figure 25 are the Cr and Mo elemental maps obtained from a randomly selected area in the 10%CF 316L material. The higher Cr and Mo content in the stringers confirms that they are delta ferrites. The same observations were obtained in EDS elemental mapping of areas from 316L materials at other cold work levels.

Then the EDS analyses were performed with a focus on evaluating the precipitates observed in the delta ferrites or along the interface between the delta ferrites and the matrix. An example is provided in Figure 26 on the 20%CF 316L material, where the precipitates that feature a brighter contrast than the delta ferrites and the matrix in the SEM-BSE image are predominantly enriched by Mo with minor enrichment of Si. In addition, a darker precipitate observed in the upper center region of the image, next to Mo-rich precipitates near the delta ferrite-matrix interface, is essentially enriched in Mn, indicating the presence of manganese sulfide (MnS). In fact, a mild presence of MnS inclusions was observed in the 316L materials cold forged to different levels, as evidenced by EDS line scans shown in Figures 27 and 28 for the 10% and 30% CF 316L, respectively. They frequently coexist with other precipitates such as

Mo-rich precipitates and TiAlO particles (Figures 26, 27, and 28b). The association of MnS with delta ferrite interfaces suggests preferential segregation during solidification, influenced by localized chemical composition and phase transformation dynamics. These inclusions are known to be initiation sites for pitting corrosion, and may impact localized mechanical properties. It would be interesting to evaluate their role in SCC initiation in the subsequent tests.

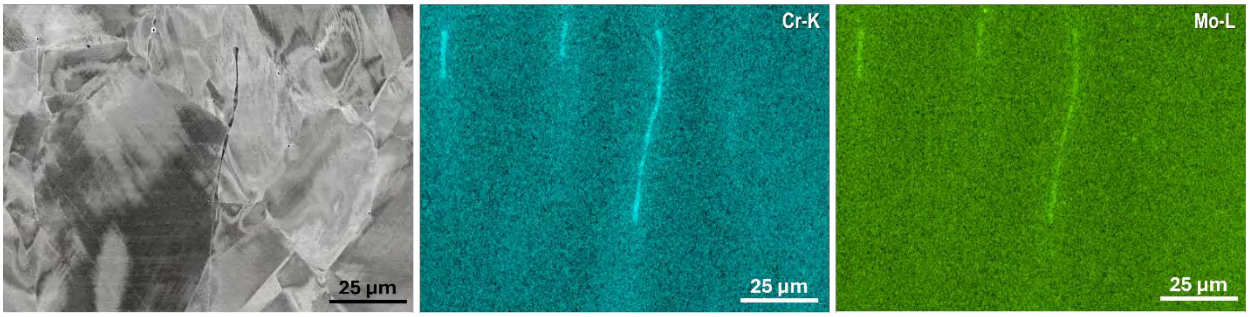

Figure 25. SEM-BSE image and EDS elemental mapping of a randomly selected area in the 10%CF 316L material (TS plane view) that confirmed the stringers are delta ferrites.

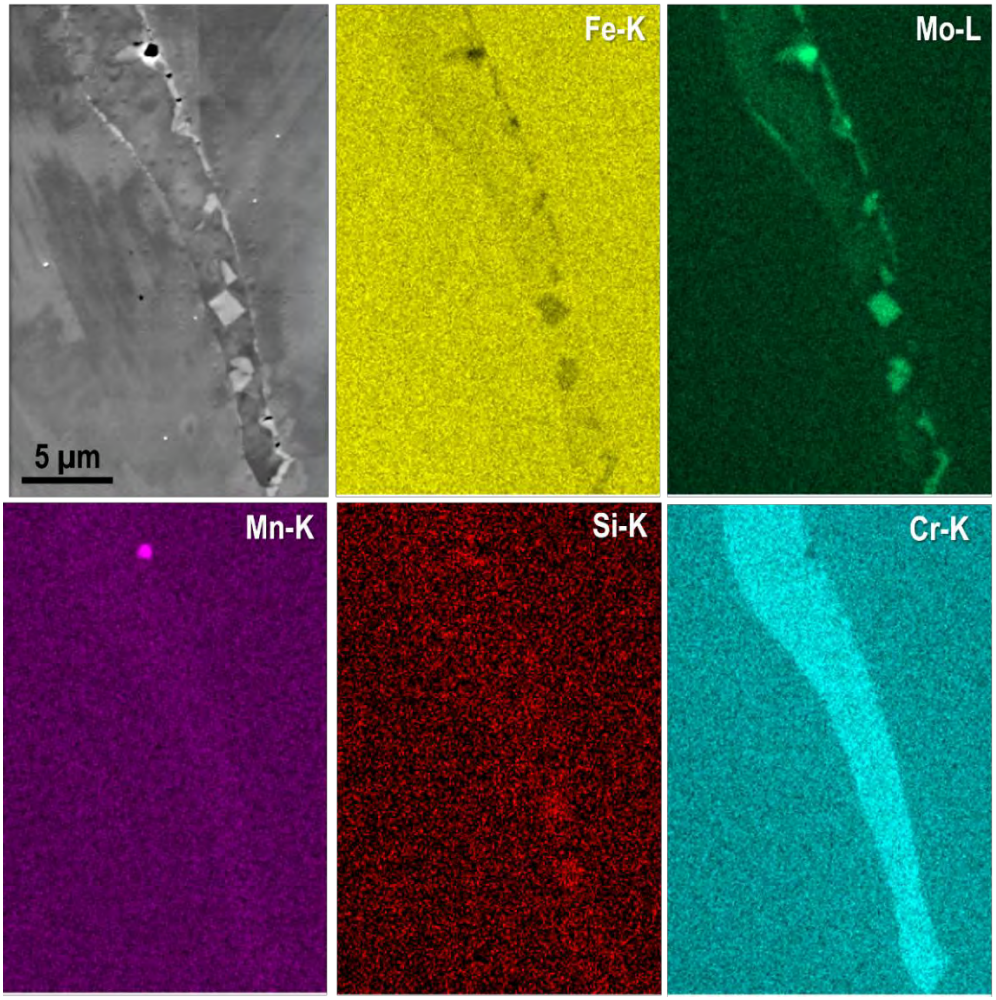

Figure 26. SEM-BSE image and EDS elemental mapping of a delta ferrite in the 20%CF 316L material (TS plane view).

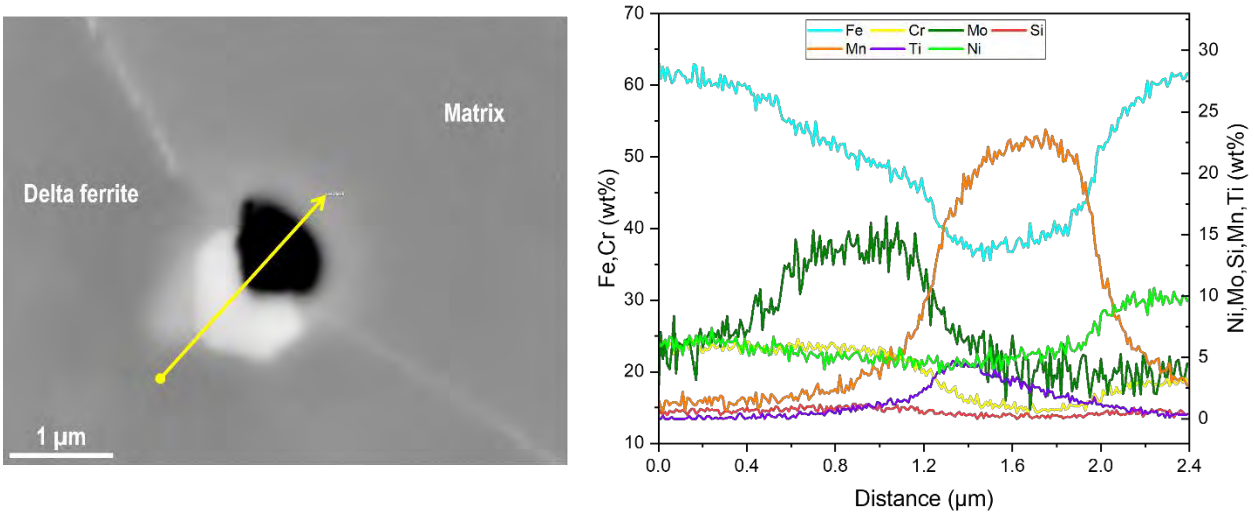

Figure 27. SEM-BSE image and EDS line scan of two precipitates residing on the delta ferrite-matrix interface in the 10%CF 316L material.

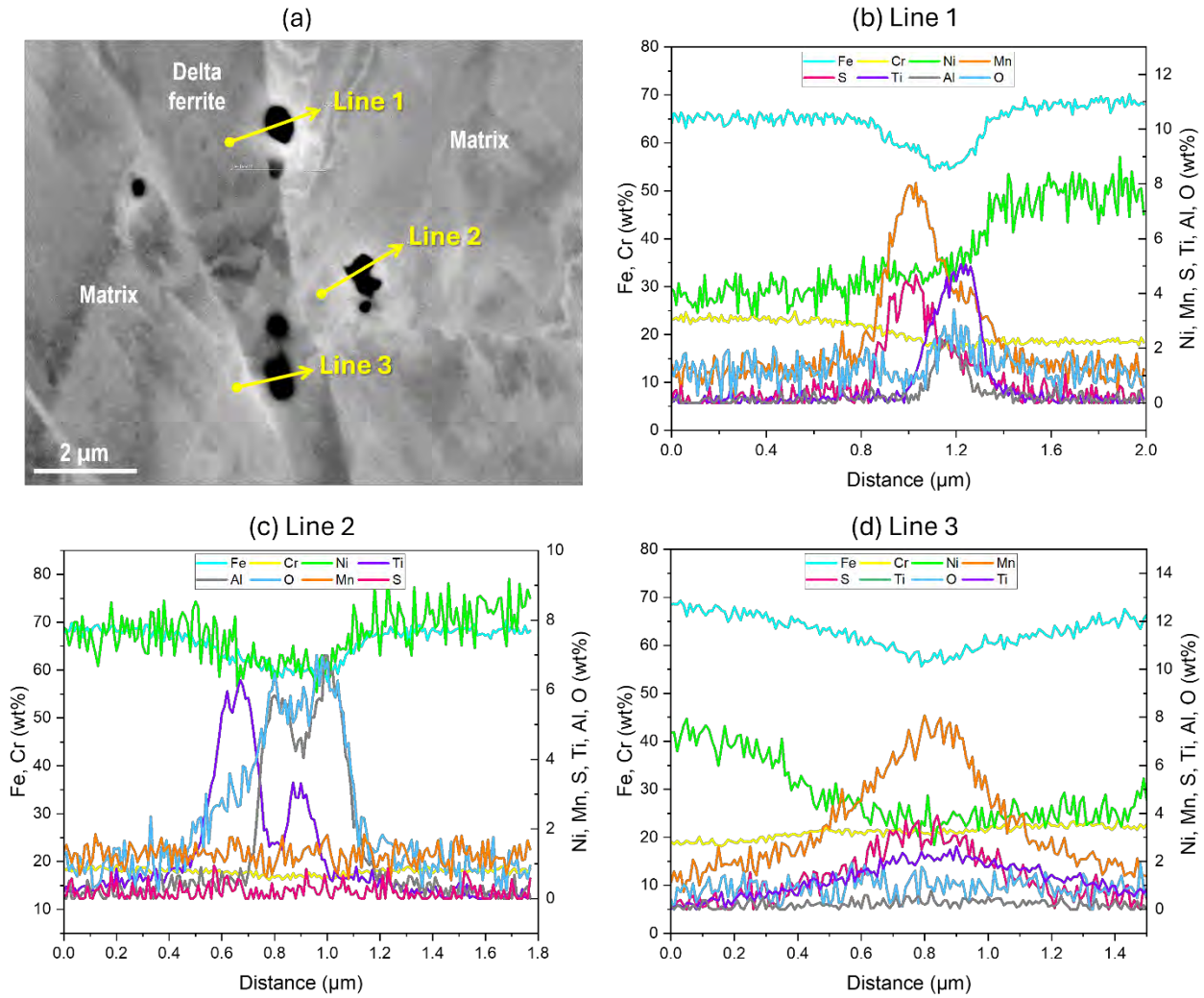

Figure 28. SEM-BSE image and EDS line scans of three precipitates located in or near a delta ferrite in the 30%CF 316L material.

3.3.2.2 EBSD Analysis

EBSD was performed on the 316L materials following a similar procedure used for 304L as described in Section 3.3.1.2. All EBSD were performed in the center of the TS plane sample as shown in Figure 13b. Microstructural comparisons between different levels of cold work were first carried out at constant settings using a 150X magnification with a 2 μm step size, and the results are presented in Figures 29–34. The inverse pole figure maps (Figure 29) and pole figures (Figure 30) illustrate the texture development as deformation progressed. In the 10%CF material, the grains exhibit relatively random orientations indicative of a less pronounced texture. With the increase in cold forge level, especially in the 30% and 40%CF materials, the grains show stronger alignment along specific crystallographic directions, reflecting the growing influence of deformation-induced texture formation and the activation of slip systems. Phase identification primarily consisted of differentiating between BCC (second phase) and FCC (matrix) iron and the results are presented in Figure 31. The stringers marked in red in these maps are identified as of BCC structure. Combined with the results of EDS analysis on these features, it is further confirmed that they are delta ferrites instead of strain-induced martensite, since strain-induced martensite is not compositionally different from austenite. The KAM maps shown in Figure 32 provide a detailed visualization of local strain variations within the microstructures of cold forged 316L. At 10%CF level, elevated strains are generally localized to regions in the vicinity of high-angle grain boundaries (HAGB). The increase in cold forge level clearly led to increasingly pronounced and widespread strains through the grains and localized areas of high misorientation, suggesting dislocation pile-ups and strain accumulation. In Figure 33, GB types are highlighted for HAGBs and twin boundaries, where an obvious increase in HAGBs was observed with the increase in cold forge level. These changes are indicative of progressive grain refinement via the deformation processes, which will likely result in changes of mechanical properties such as strength and hardness. In addition, grain boundary distribution analysis was performed with respect to the FCC and BCC phases and the results are summarized in Figure 34. Cold forging appears to have minimal influence on the grain boundary character distribution within the ferrite phase. Regardless of the cold forge levels, ferrite grains predominantly exhibit low-angle grain boundaries (LAGBs). This stability suggests that ferrite grains are less susceptible to extensive strain accumulation or grain refinement during cold forging. In comparison, the austenitic phase of the matrix behaves differently under cold work conditions. When analyzed as random pairs, the FCC phase exhibits a typical Mackenzie distribution, which is generally observed for materials with random misorientations. This distribution is closely related to the statistical prevalence of HAGBs within the FCC matrix prior to deformation, reflecting the structure's grain boundary equilibrium state. Cold forging did induce changes in boundary characteristics as deformation progresses, but this random pairing behavior in terms of misorientation distribution was generally preserved in the 10% and 20% CF materials, while progressively larger offset towards higher angles was observed when the cold forge level was increased to 30% and then 40% reduction in thickness. Another key observation is the distinct increase in the fraction of LAGBs between neighboring grains with increasing cold work. This trend signifies strain-induced adjustments to the misorientation of grain boundaries, with higher cold forge level inducing stronger local substructure formation.

Additional high-resolution maps with higher magnifications (500X, 1kX, 1.5kX) were recorded for localized grain boundary and phase identification with examples acquired from the 20%CF and 30%CF 316L samples, which are shown in Figures 35 and 36, respectively. Internal strain accumulation was observed inside the ferrites, indicating dislocation build-up resulted from lattice reactions with adjacent grains, including austenitic neighbors. Delta ferrites exhibit considerable internal strain, accompanied by strain contouring around neighboring grains, likely due to mechanical incompatibilities with the FCC matrix during cold forging. In addition, the EBSD results revealed no localized stress concentrations or strain accumulation patterns within the matrix that would directly support nucleation events for martensite formation. Instead, these observations further confirmed that the ferrite presence within these 316L materials is governed by thermodynamic and compositional factors inherent to the alloy rather than strain gradients induced during cold forging processes.

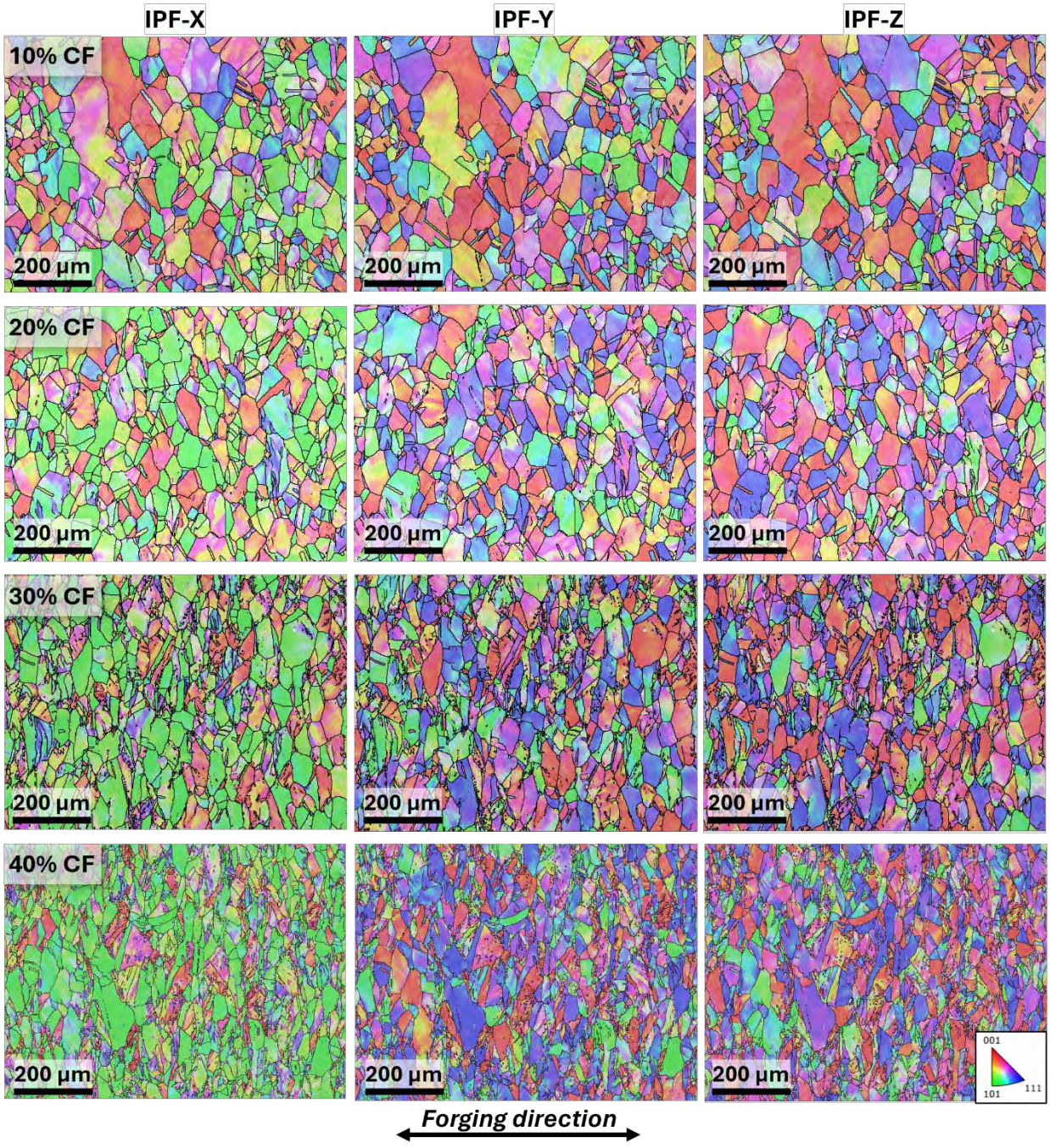

Figure 29. Comparison of EBSD inverse pole figure maps taken at 150X on the TS plane of the 10, 20, 30, and 40%CF 316L materials.

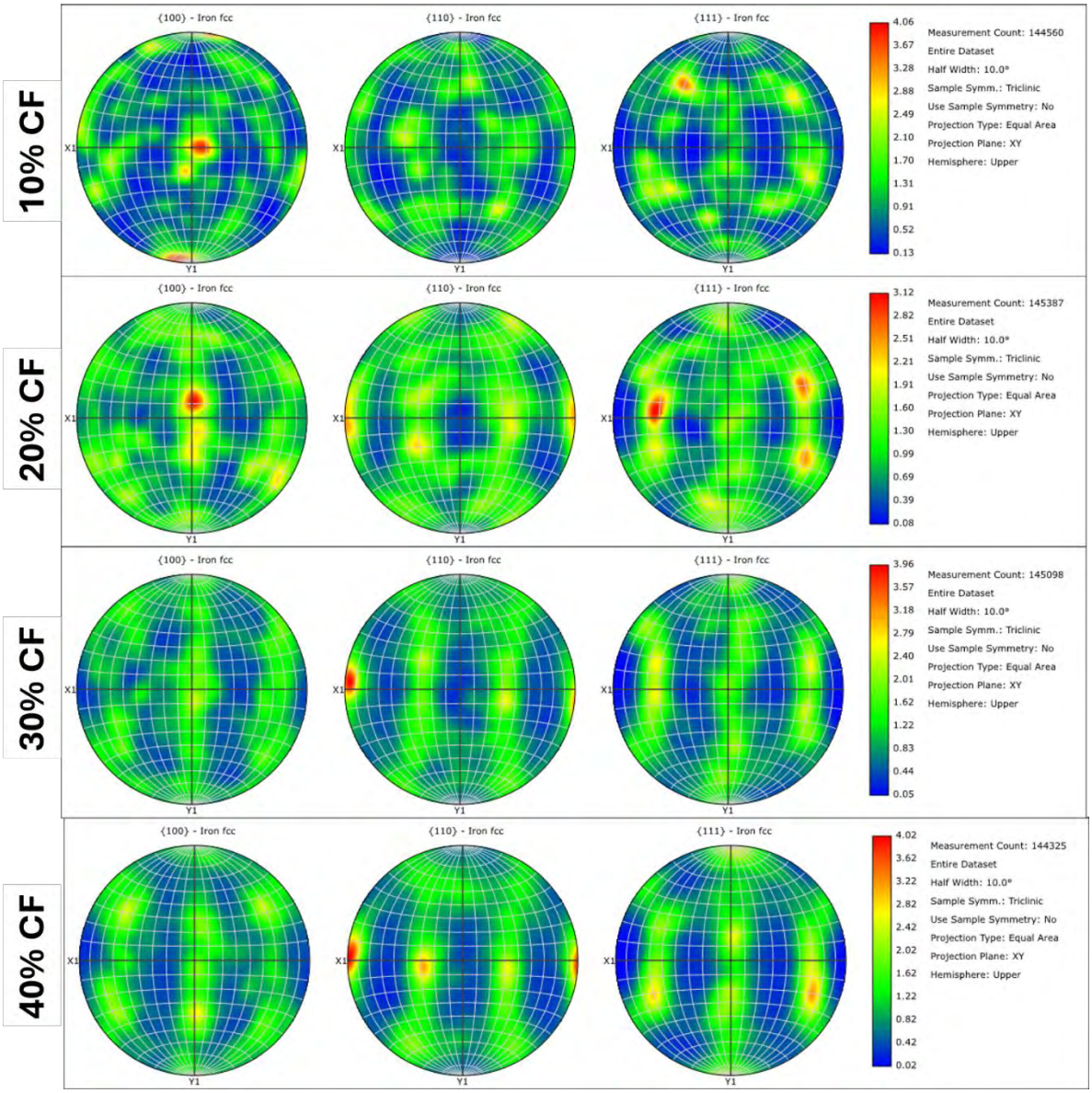

Figure 30. Pole figures showing the texture evolution in the 316L materials with the increase in cold forge level.

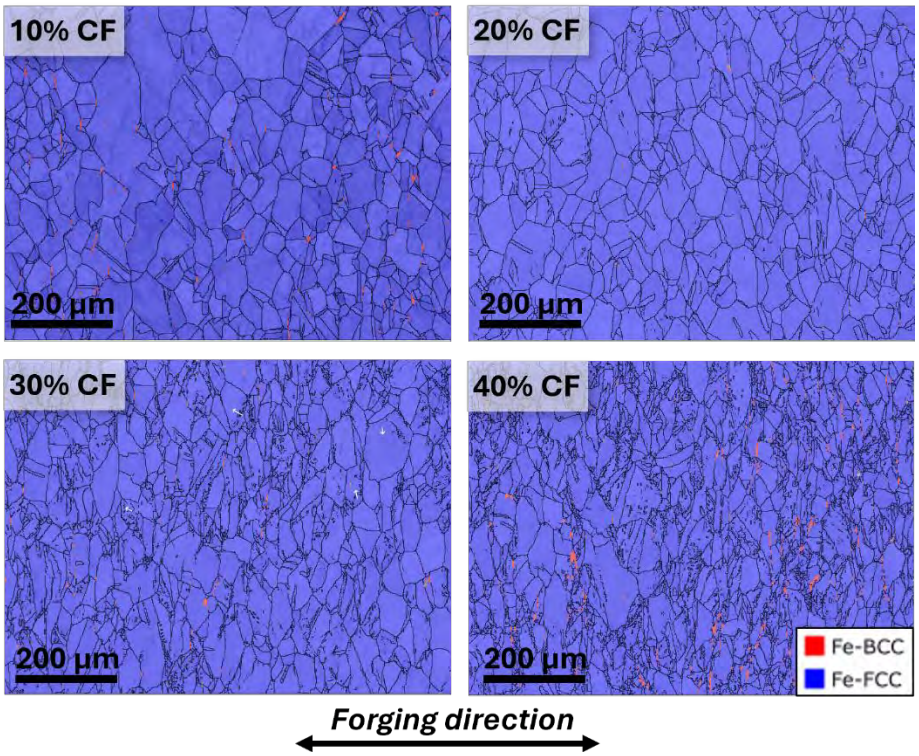

Figure 31. Comparison of EBSD phase maps taken at 150X on the TS plane of the 10, 20, 30, and 40%CF 316L materials.

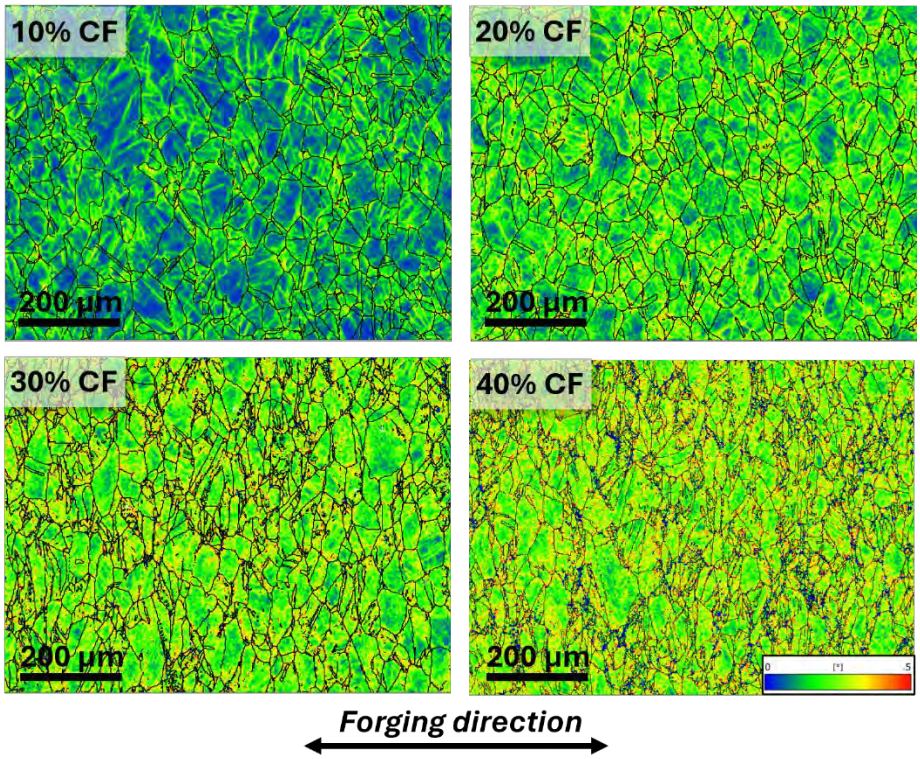

Figure 32. Comparison of EBSD KAM maps taken at 150X on the TS plane of the 10, 20, 30, and 40%CF 316L materials.

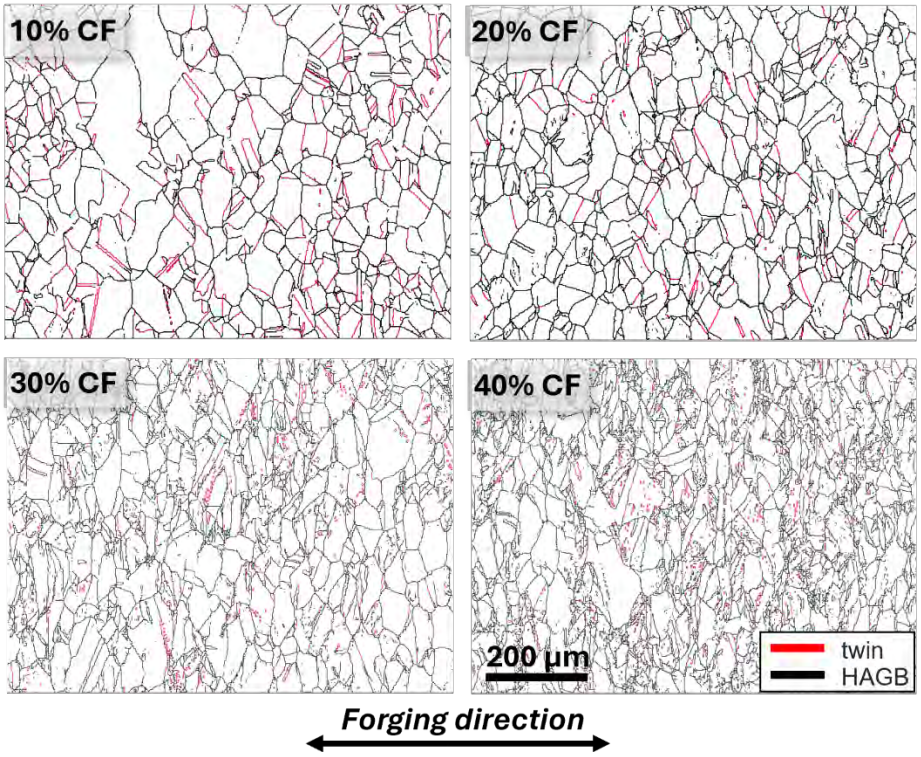

Figure 33. Comparison of EBSD grain boundary type maps taken at 150X on the TS plane of the 10, 20, 30, and 40%CF 316L materials.

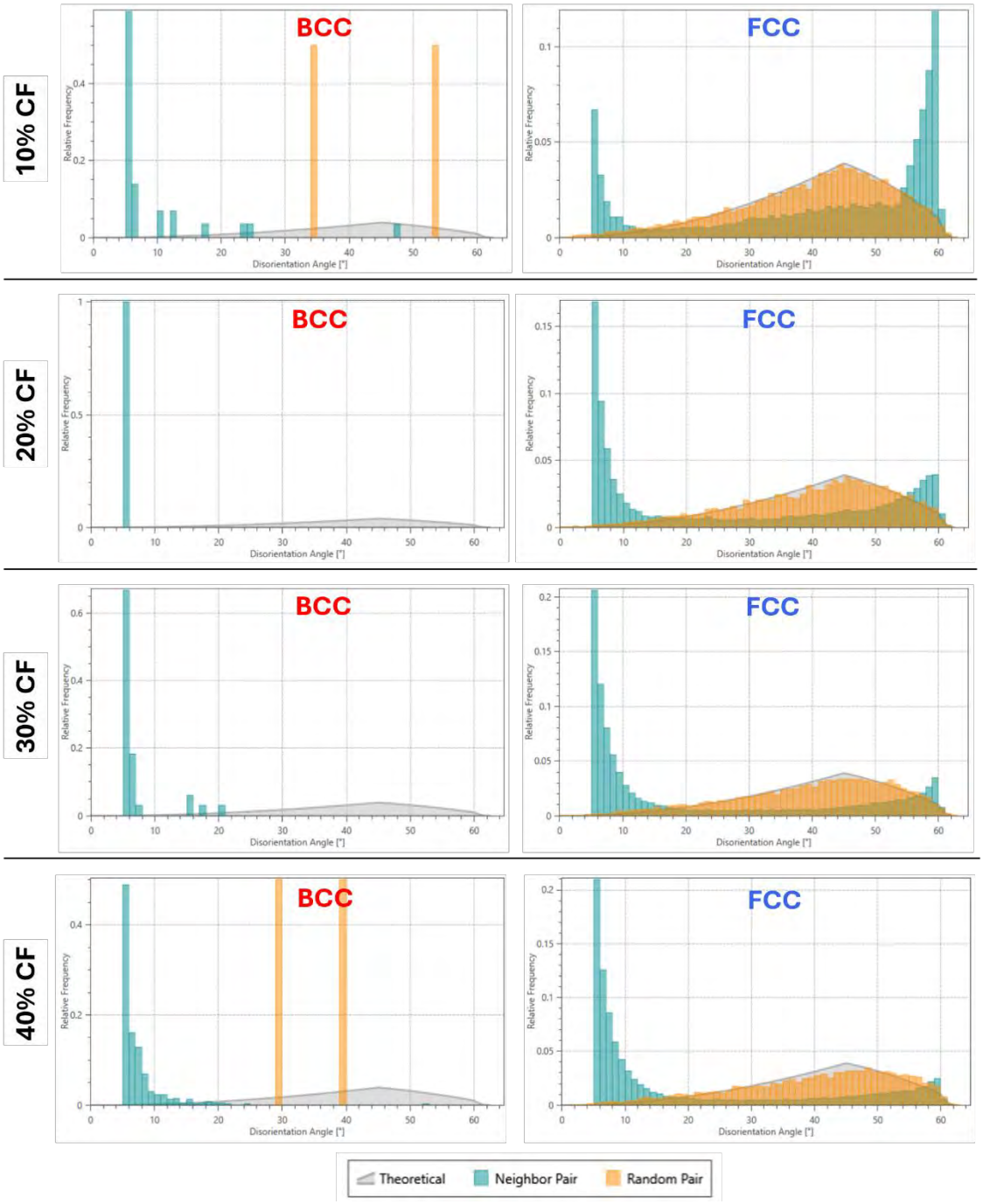

Figure 34. Comparison of the GB misorientation distribution of the BCC phase (left column) and FCC phase (right column) in 316L materials at four different cold forge levels.

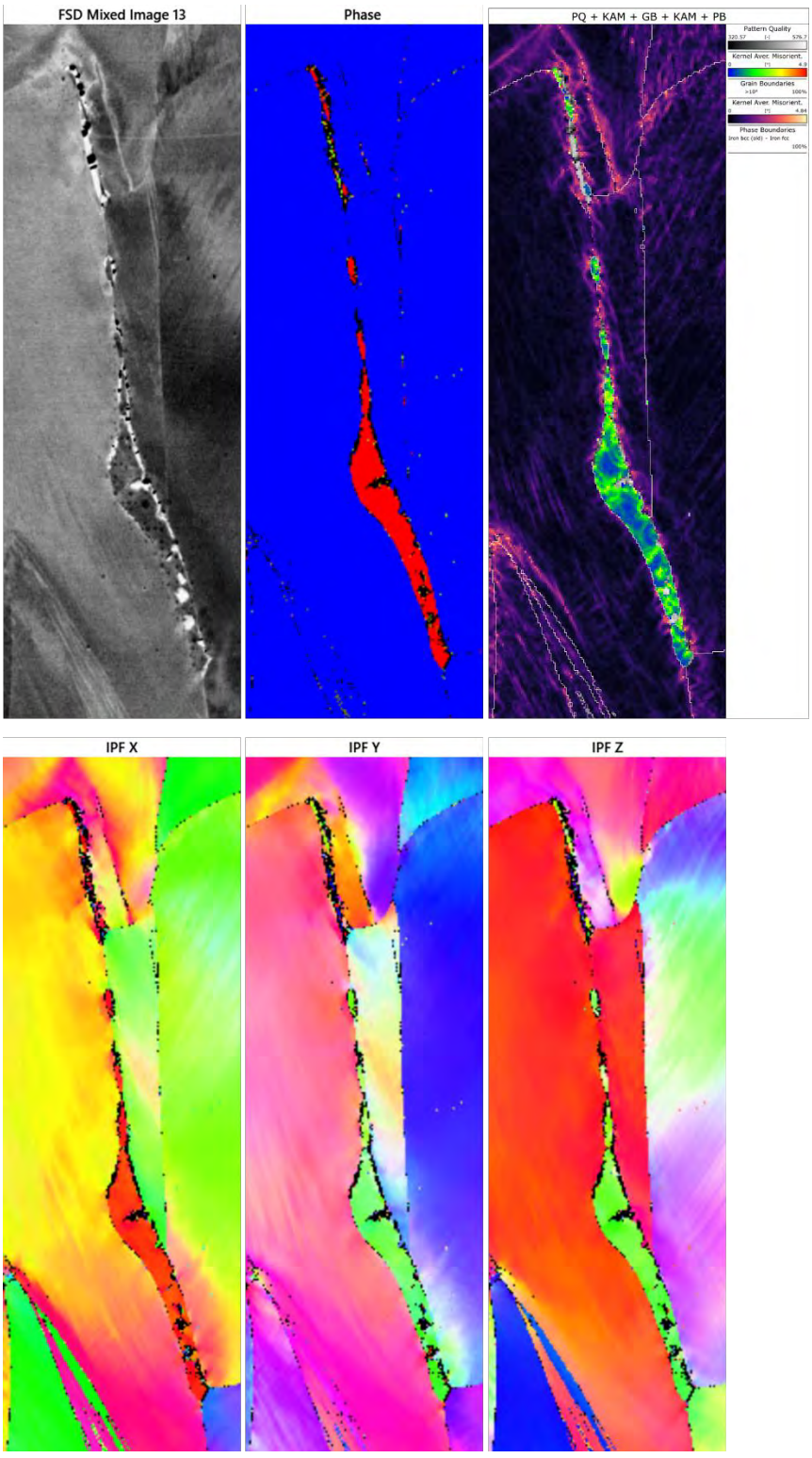

Figure 35. EBSD maps (from left to right on the top row: BSE+ pattern quality, phase, KAM, on the bottom row: IPF-X, Y, Z) in the vicinity of a delta ferrite in the 20%CF 316L.

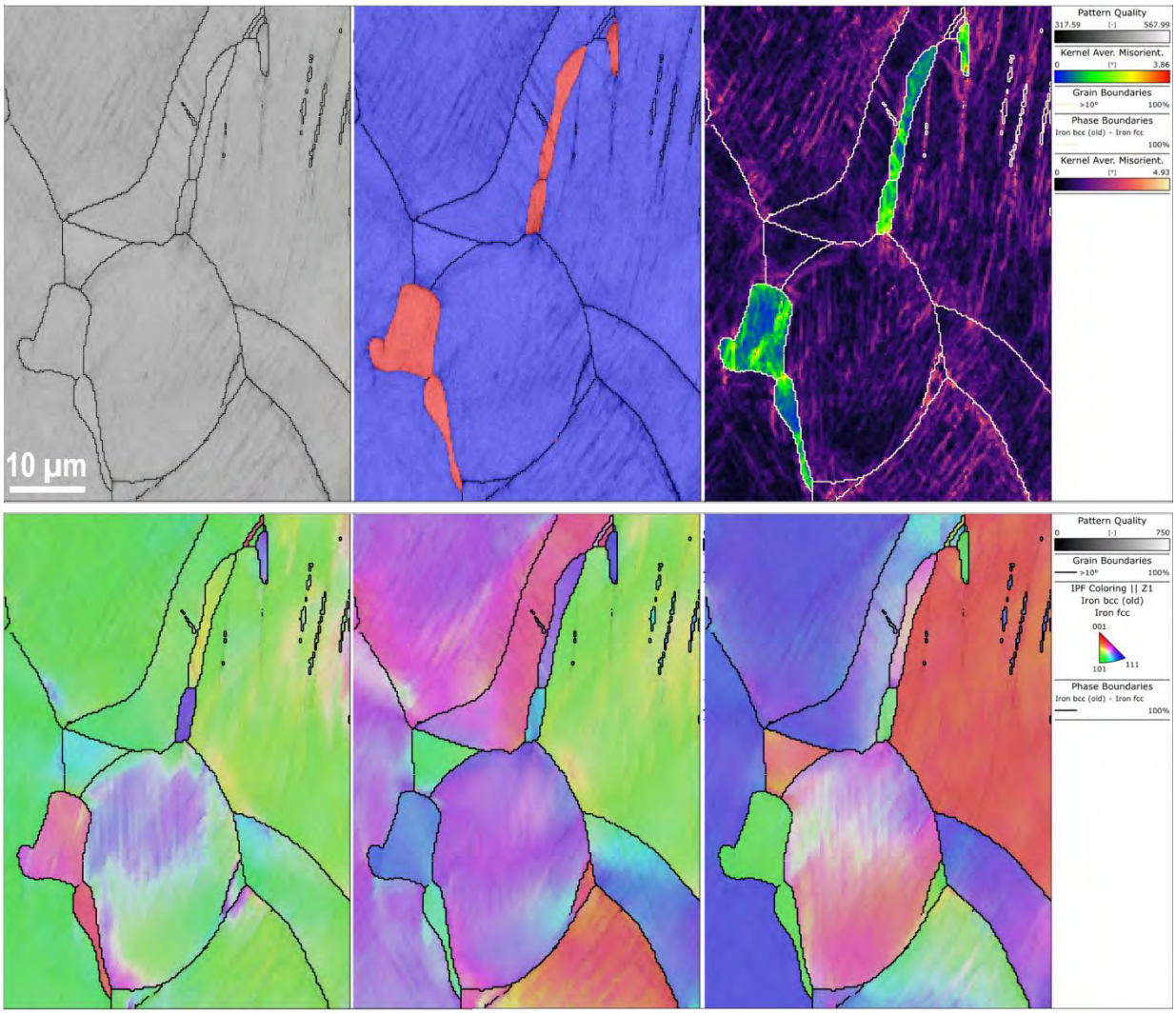

Figure 36. EBSD maps (from left to right on the top row: pattern quality, phase, KAM, on the bottom row: IPF-X, Y, Z) in the vicinity of two delta ferrites in the 30%CF 316L.

3.3.3 X-Ray Diffraction Analysis

Complementary X-ray diffraction (XRD) analysis was conducted alongside EBSD to confirm the presence or absence of strain-induced martensite in the cold-forged 304L and 316L materials, taking advantage of its effectiveness in identifying crystallographic phases based on their unique set of diffraction peaks, which correspond to specific atomic plane spacings. The XRD data were collected using a Rigaku SmartLab XE diffractometer in Bragg-Brentano geometry, equipped with a Cu rotating anode ($\lambda = 1.5418$ Å) operating at 45 kV and 200 mA. A variable divergence slit illuminated a 10 mm x 10 mm area of the sample surface, and 2.5° Soller slits were used to limit axial divergence. Diffracted intensities between 15 and 100° 2θ were recorded at 0.01° intervals using a position-sensitive HyPix 3000 detector operating in 1D mode. The results for the materials evaluated are summarized in Figure 37, where the diffraction peaks correspond to distinct crystallographic phases, including austenite (FCC) and delta ferrite (BCC). Peaks at 43.5°, 50.7°, and 74.3° represent austenite reflections from {111}, {200}, and {220} planes, while delta ferrite reflections appear at 44.6°, 65.0°, and 82.3°, associated with {110}, {200}, and {211} planes. Additional peaks at 90.5° and 96° suggest higher-order reflections of austenite. It is noted that the alpha1/alpha2 doublet is well resolved for the 10% forged samples at 96°, but becomes progressively broader (and therefore less resolved) with increasing forging levels. This indicates that forging has induced strain and/or reduced crystallite size, which is consistent with the findings from EBSD analysis. If martensite is present, their peaks would overlap or closely align with delta ferrite peaks but show broader profiles due to higher defect densities and internal stresses associated with deformation. Additionally, the relative intensity of martensite-related peaks is expected to increase with the level of cold work, reflecting a greater phase transformation. However, no evidence of martensite was observed in the XRD patterns, which is consistent with the EBSD results and further confirms that martensite was not induced during the cold forging process.

While the texture induced by forging makes it difficult to obtain good quantification, an attempt was made using an arbitrary model for texture to get an indication of the delta ferrite content. This resulted in about 3–4 % for the 304L series and 1–3 % for the 316L series, and there did not appear to be any trend with increasing forging level.

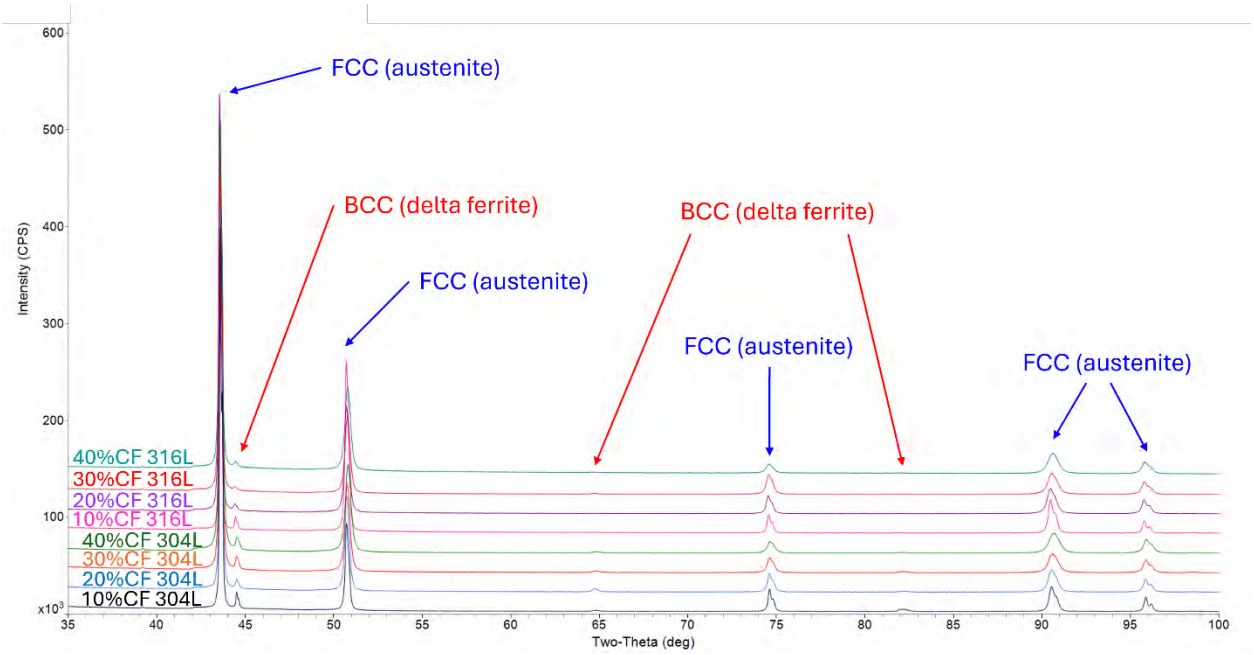

Figure 37. XRD patterns showing the two-theta peaks observed for cold-forged 304L and 316L stainless steel at various cold forge levels (10%, 20%, 30%, and 40%).

3.3.4 Hardness Measurements

After the completion of all SEM and XRD characterizations, Vickers Hardness testing was performed on these mounted samples. For each CF condition, hardness was measured on samples prepared from all three different orientation planes of the cold forged block, as illustrated in Figure 13b. A Series CM-802 Micro Indentation Clark Instrument was used with a load of 300 gf and a dwelling time of 12 seconds per indent. The accuracy of indent reading was checked using standard samples before the actual hardness tests to ensure comparability of the hardness values measured from different material conditions. As shown in Figure 38, the sampling area is a ~3×3 mm^2 region at the center of each specimen, which includes ~170 indent points.

The measured average hardness data are summarized in Table 4 and plotted in Figure 39 for 304L and in Figure 40 for 316L for better visualization. The average hardness values measured in 304L from three orientation planes steadily increased with increasing cold work, and the difference in hardness values among the planes are within statistical error at each cold forge level, indicating uniform deformation-induced strengthening. As shown in Table 4, the overall average hardness measured for the 10%CF 304L material is ~224 HV and increased by 30 HV to 255 HV for the 20%CF material. Then the increase in hardness slowed down and increased by 15 HV for each 10% additional increment in cold forging level, resulting in an average hardness value of ~288 HV for the 40%CF 304L material. The 316L materials exhibited slightly lower hardness values in almost all planes and cold work levels compared to 304L, despite having a higher yield strength than 304L at 300°C, as will be presented and discussed in the next section. At 10%CF, the average hardness for 316L is ~218 HV, only slightly lower than 304L in this condition, indicating similar initial deformation responses. At 20%CF, the hardness increased to 241 HV, showing slower work-hardening progress compared to 304L. The increase in average hardness remained steady at ~20 HV for subsequent increases in cold work, leading to an overall average hardness of ~290 HV for the 40%CF 316L material. However, it should be noted that increased anisotropy was observed in 316L, with the highest hardness always observed in the LS plane, particularly in the 20% and 40%CF conditions, where the average hardness values measured in the LS plane are >20 HV than the average hardness values measured in the other two planes. In addition, the hardness fluctuation measured on each plane of the 40%CF 304L and the 40%CF 316L materials was illustrated in Figures 41 and 42, respectively. Regions of hardness values exceeding 300 HV are interweaved with regions of hardness values below 250 HV, highlighting the inhomogeneous nature of the hardness distribution. More pronounced orientation-dependent anisotropy in 316L than in 304L was also revealed when the hardness values were colored according to the same scale across the three orientations, where the hardness values in the LS plane of the 40%CF 316L are obviously higher than the other planes (Figure 42).

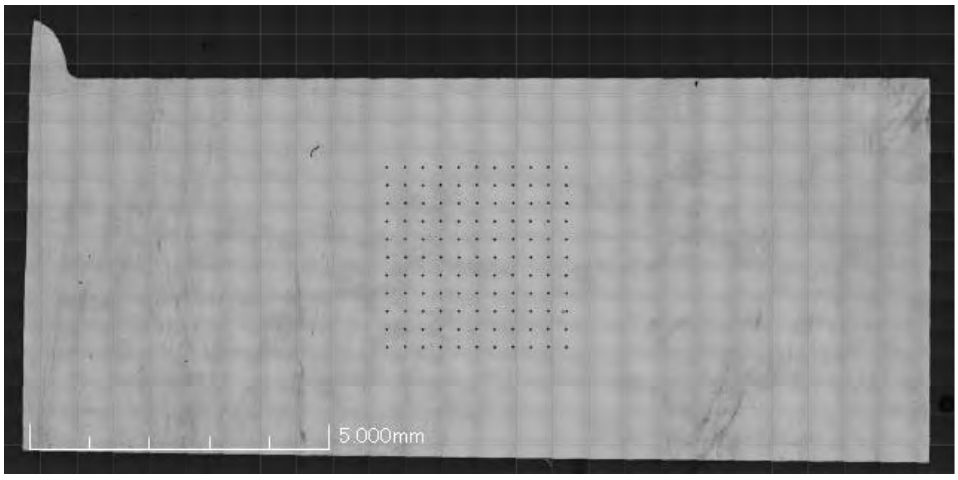

Figure 38. An optical micrograph showing the typical area sampled for hardness measurement in the specimens.

Table 4. Measured hardness values for the cold forged 304L and 316L materials.

Hardness / Material	Avg. HV (kg/mm^2)			
	LS plane	**TS plane**	**TL plane**	**All planes**
10% CF 304L	228.7±7.2	221.7±8.4	222.7±8	224.4±8.4
20% CF 304L	258.2±10.1	253.6±11.5	253.0±9.9	254.9±10.8
30% CF 304L	276.2±16.9	262.9±15.2	272.0±11.4	270.4±15.7
40% CF 304L	282.8±25.7	294.3±14.7	285.4±17.9	287.5±20.5
10% CF 316L	222.7±10.8	216.6±9.0	215.8±9.1	218.4±10.1
20% CF 316L	256.7±13.4	234.5±10.3	232.3±8.9	241.2±15.7
30% CF 316L	272.4±10.5	267.4±11.8	248.8±12.8	262.8±17.0
40% CF 316L	302.0±13.5	278.8±10.4	273.9±9.7	284.9±17.0

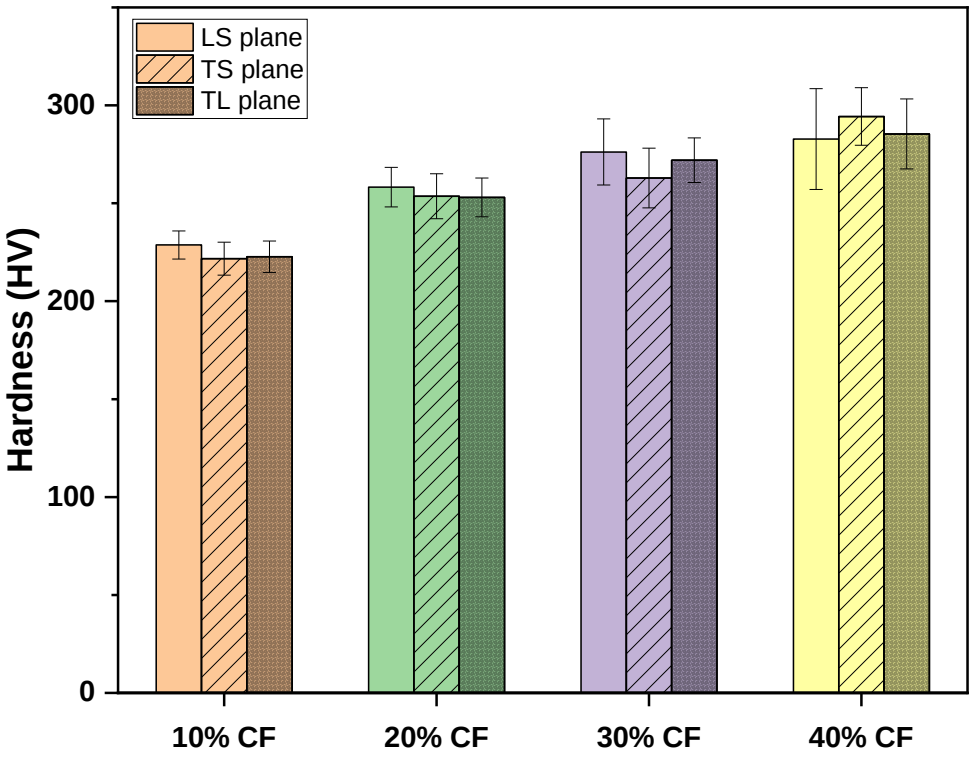

Figure 39. Hardness values measured on the LS, TS, and TL planes of the 304L blocks cold forged to 10%, 20%, 30%, and 40% reduction in thickness.

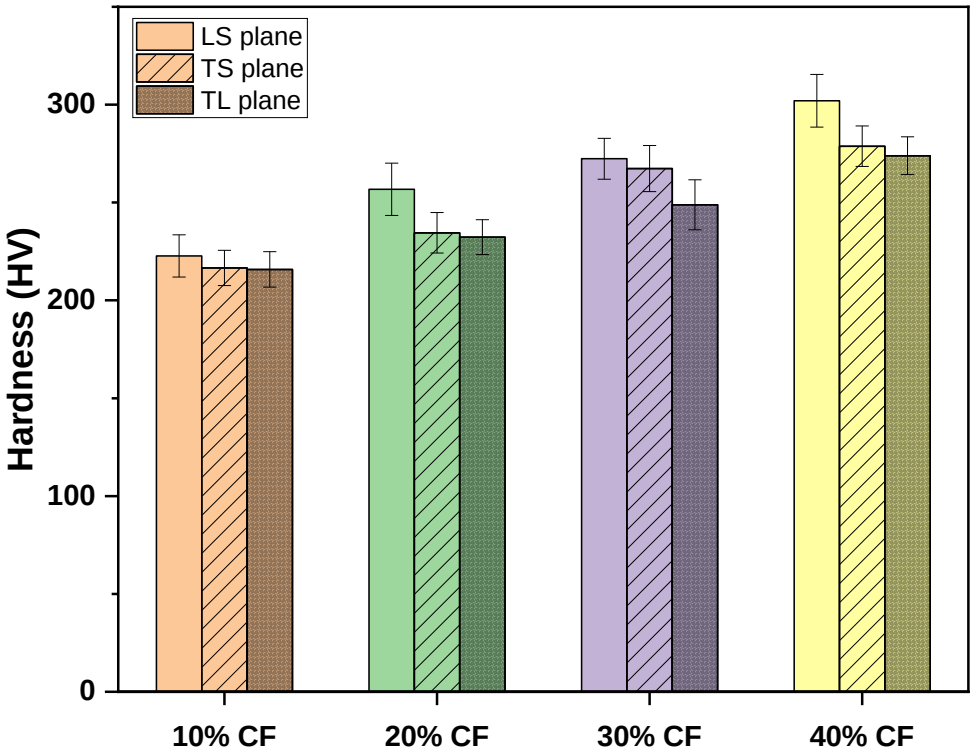

Figure 40. Hardness values measured on the LS, TS, and TL planes of the 316L blocks cold forged to 10%, 20%, 30%, and 40% reduction in thickness.

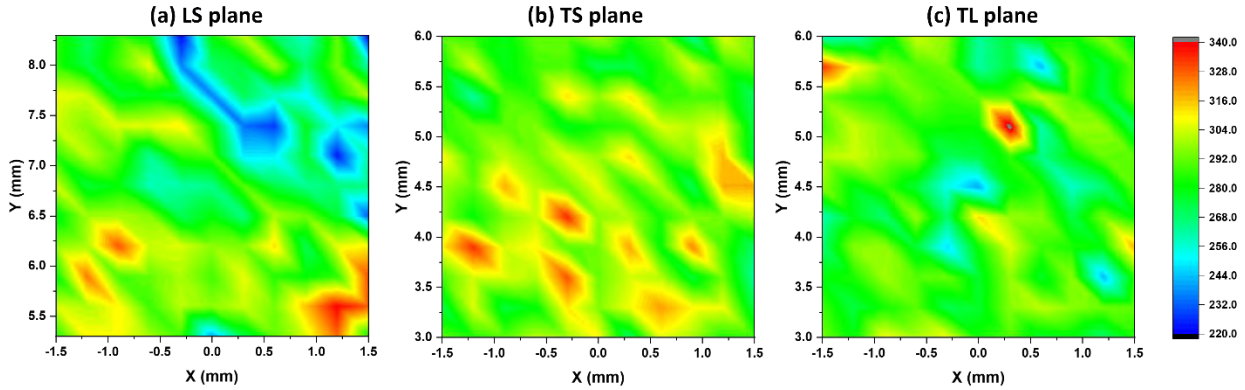

Figure 41. Hardness contour maps on the three planes of the 40%CF 304L material.

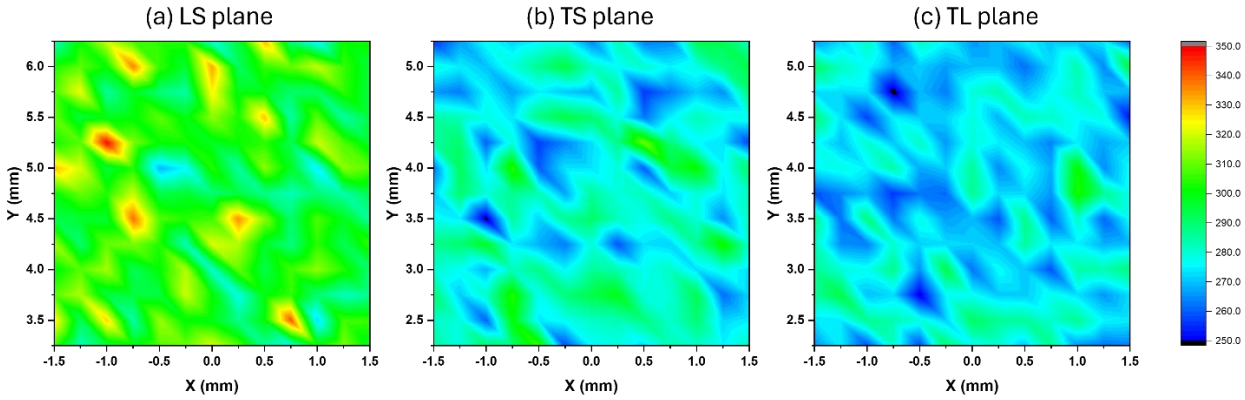

Figure 42. Hardness contour maps on the three planes of the 40%CF 316L material.

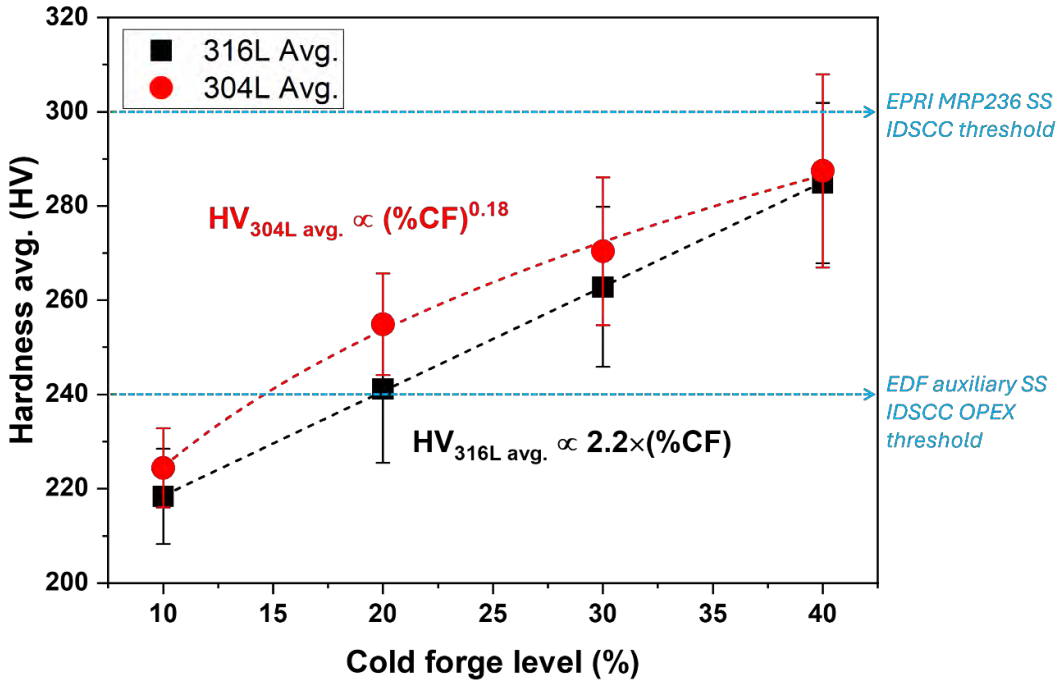

Figure 43. Overall average hardness values of 304L and 316L as a function of cold forge level with a power law fit for 304L and a linear fit for 316L.

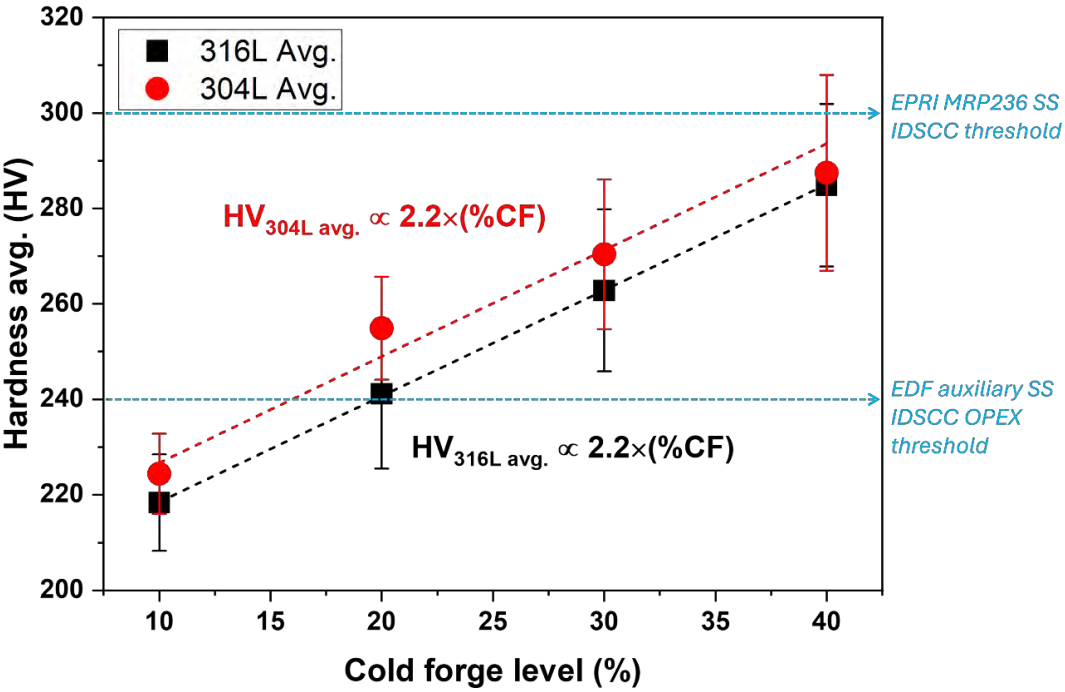

Figure 44. Overall average hardness values of 304L and 316L as a function of cold forge level with linear fit for both materials.

The hardness data clearly suggest there is some difference in the work hardening behavior between 304L and 316L. The overall average hardness values in cold forged 316L in the range of 10% to 40% reduction in thickness clearly follows a linear relationship with cold work, while the magnitude of increase in the overall average hardness values in the cold forged 304L tend to slow down with the increase in cold work, of which the trend appears to be best interpreted by a power law fit, as shown in Figure 43. Nevertheless, an attempt was also made to fit the overall average hardness values from both 304L and 316L to a linear relationship with the cold work level, and the result is presented in Figure 44. Interestingly, the linear coefficient turned out to be the same for both materials. The hardness threshold reported for SCC to occur in stainless steels in PWRs based on operation experience was also marked in these figures. It suggests that the 304L and 316L materials cold forged to 20% reduction and above have produced average hardness values equivalent or higher than the hardness threshold reported for SCC to occur in the SS auxiliary piping in French NPPs, but cold work higher than 40% reduction is needed to achieve the threshold hardness of 300 HV identified in MRP-236 for SCC in stainless steels in nominal PWR primary water, consistent with what was reported in literature [9]. Nevertheless, it should be noted that the measurements for determining the hardness threshold from operation experience may have been obtained using a different force during hardness testing. For example, the hardness measurement performed on the plant weld materials from the French NPPs were usually performed with an applied force of either 100 g or 500 g. In order to evaluate the impact of using different forces on the resulted HV values, additional hardness testing was performed on the 40%CF 304L sample on the TS plane at four different test loads: 100 gf, 300 gf, 500 gf, and 1 kgf. A total of 169 indents were produced in a ~3×3 mm^2 were produced at each test load, of which the distance between the centers of neighboring indents is at least 3X the diagonal length of the indent (Figure 45). The general statistics of the results are summarized in Figure 46 where a decrease in the average and median hardness values is seen when the test load was increased from 0.1 to 0.5 gf, while further increase to 1 kgf resulted in hardness values similar to those produced at 0.3 gf. As shown in Figure 47, the average hardness value consistently decreased by 10 HV when the load was increased by every 200 gf between 100 and 500 gf, indicating a linear relationship for this load range. As a result, it can be concluded that the cold forging conducted on 304L and 316L in this suggest has successfully produced high hardness values matching those measured on French SS auxiliary piping where SCC incidents were reported.

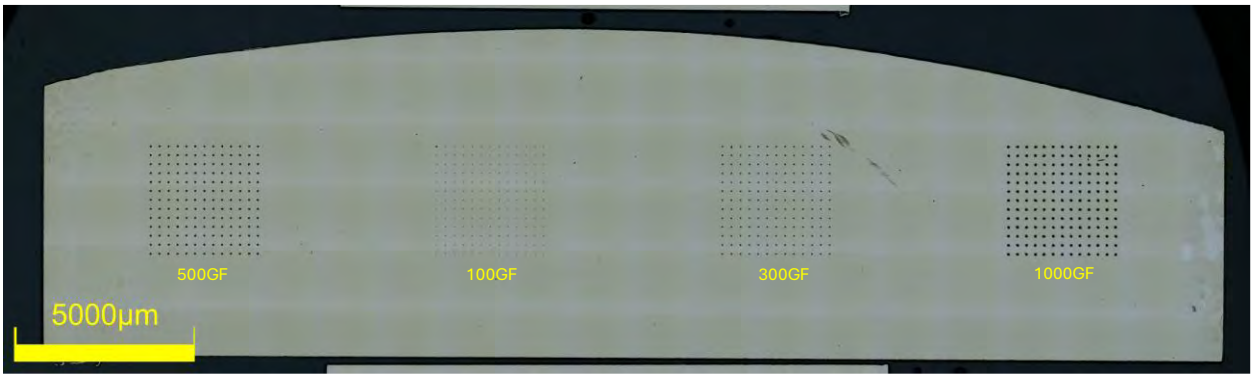

Figure 45. An optical micrograph showing the area of indents produced in the 40%CF 304L TS plane sample during hardness measurement using different test loads (from left to right: 500 gf, 100 gf, 300 gf, and 1 kgf).

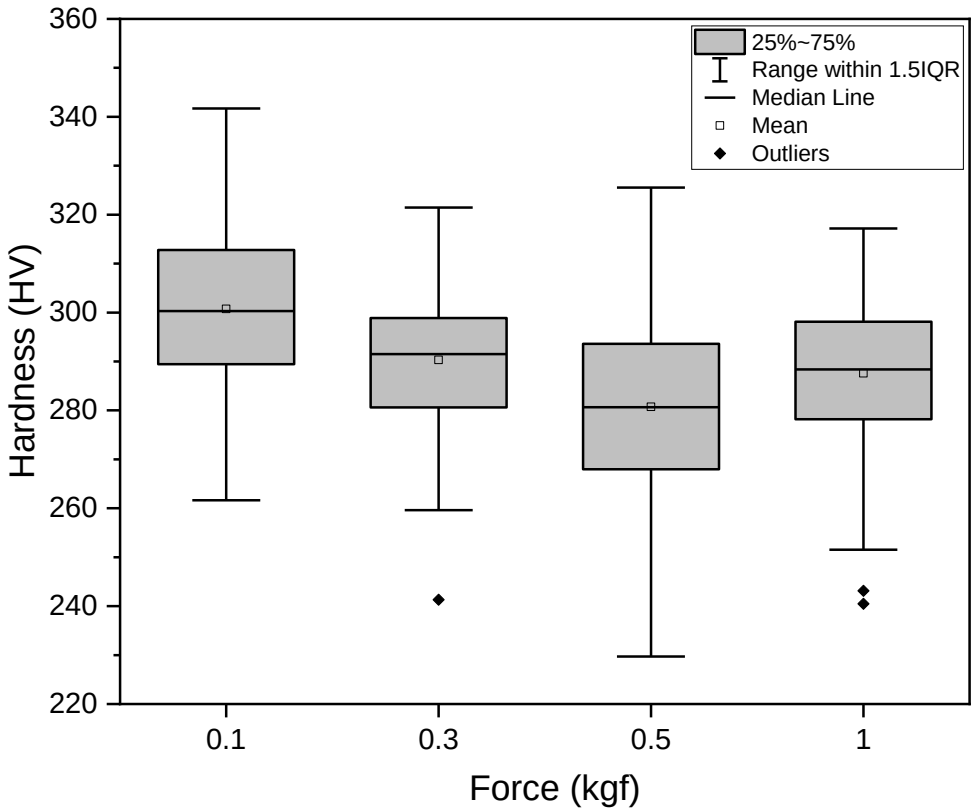

Figure 46. Statistical analysis of the HV data measured using test loads in the 40%CF 304L sample.

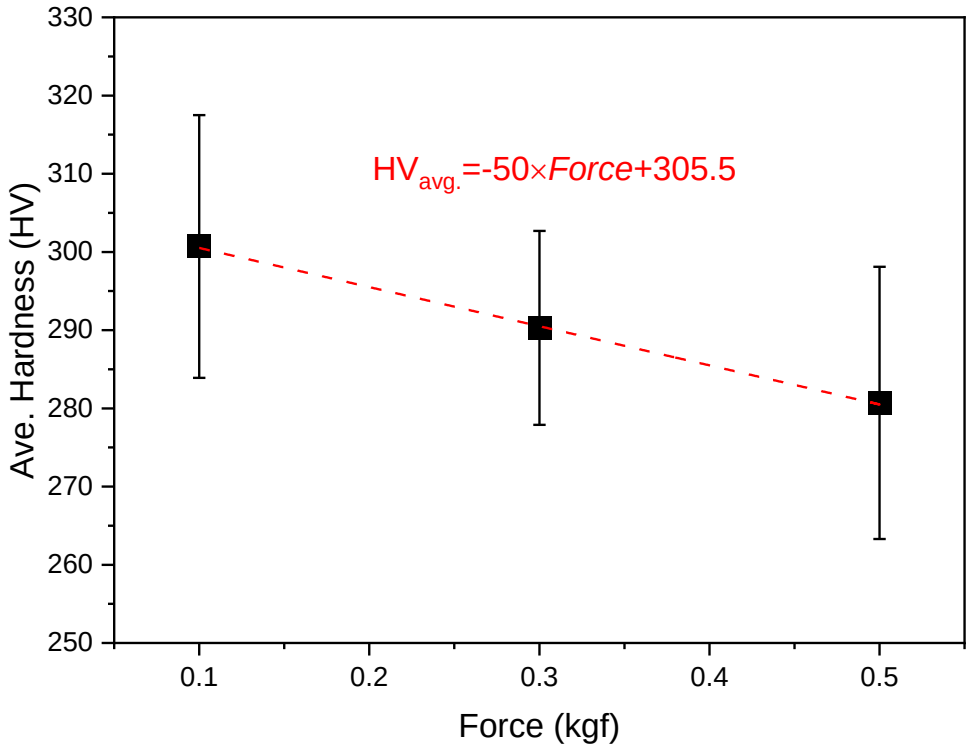

Figure 47. Average hardness values of the 40%CF 304L sample as a function of test load between 100 and 500 gf with a linear fit.

3.3.5 Tensile Testing

Tensile properties were measured on 304L and 316L materials cold forged to all four levels. The orientation and dimensions of the tensile specimens used for this testing are shown in Figures 12 and 48, respectively. The testing temperature was set at 300°C, the same temperature at which the SCC initiation testing will be performed. The obtained YS values are plotted against the corresponding hardness data of the same material and summarized in Figure 49 for 304L and in Figure 50 for 316L. They were correlated with both the hardness values measured from the TS plane, i.e., the plane normal to the loading direction of the tensile specimens, and the overall averaged hardness values measured from all three planes. A very similar linear dependence was found between the hardness values and material's YS in the form of $hardness = A \times YS$, where A varied between 0.28–0.30 for cold forged 304L and between 0.24–0.25 for cold forged 316L. It should be noted that while the yield strength measured at 300 °C on the 304L materials cold forged to different levels are lower than those of their 316L counterparts, their hardness measured at room temperature are comparable or even slightly higher than the hardness of their 316L counterparts (Figure 51). Since no strain-induced martensite has been confirmed in any of these materials, this observation may be contributed to a combination of the difference in chemical composition and processing methods of 304L and 316L, as well as the different temperatures at which the yield strength (300°C) and the hardness values (room temperature) were measured. The higher Ni and Mo content in 316L likely has promoted dynamic recovery in 316L and reduced strain localization, leading to lower hardness values. In addition, the higher Ni and Mo content and lower delta ferrite content in 316L probably promoted its thermal stability, therefore resulting in less reduction in yield strength than 304L when tested at elevated temperatures, such as at 300°C. As pointed out in the previous section, the hardness measurements demonstrate that 304L's microstructural response to cold forging initially results in higher work-hardening rates compared to 316L, leading to consistently higher hardness values despite its lower yield strength, but the work hardening rate appeared to slow down with the increase in cold work level, especially after 30% reduction, and the hardness values of the 40%CF 304L is only marginally higher than its 316L counterpart. These findings provide useful insight into the strain-hardening capabilities of austenitic stainless steels under deformation processes, and it will be interesting to assess how thermal aging will impact their microstructural evolution and mechanical properties.

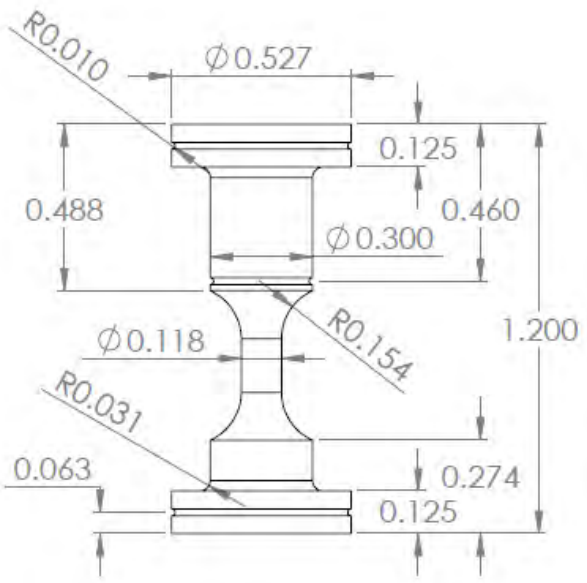

Figure 48. Dimensions of the tensile specimens (unit: inch).

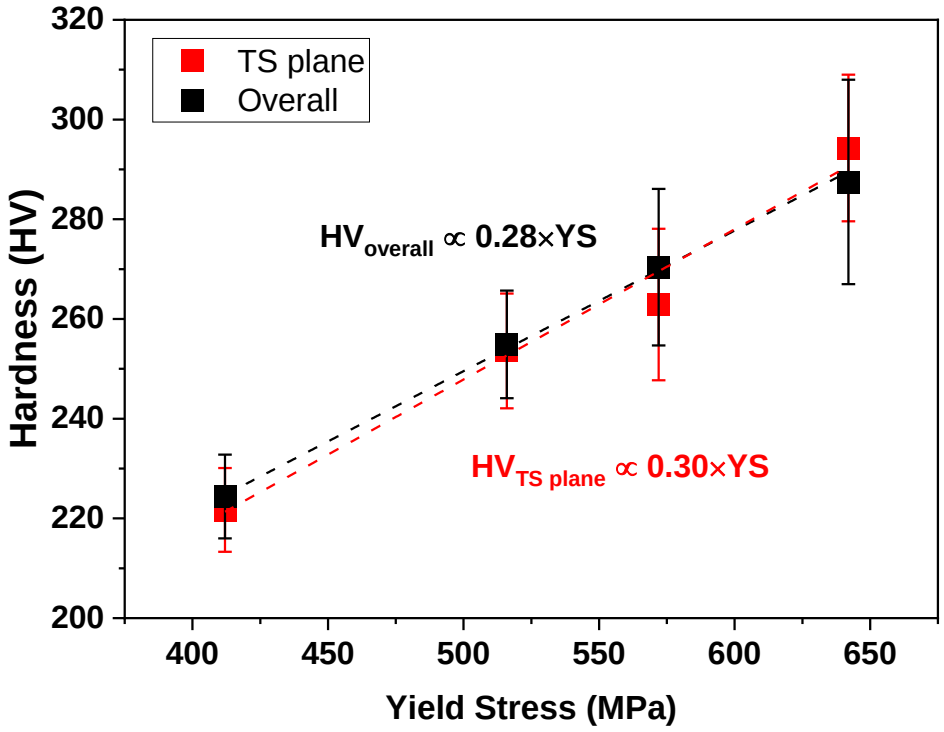

Figure 49. Hardness measured on the TS plane and the overall average hardness measured from all three planes in the 10–40%CF 304L materials as a function of their yield stress at 300 °C.

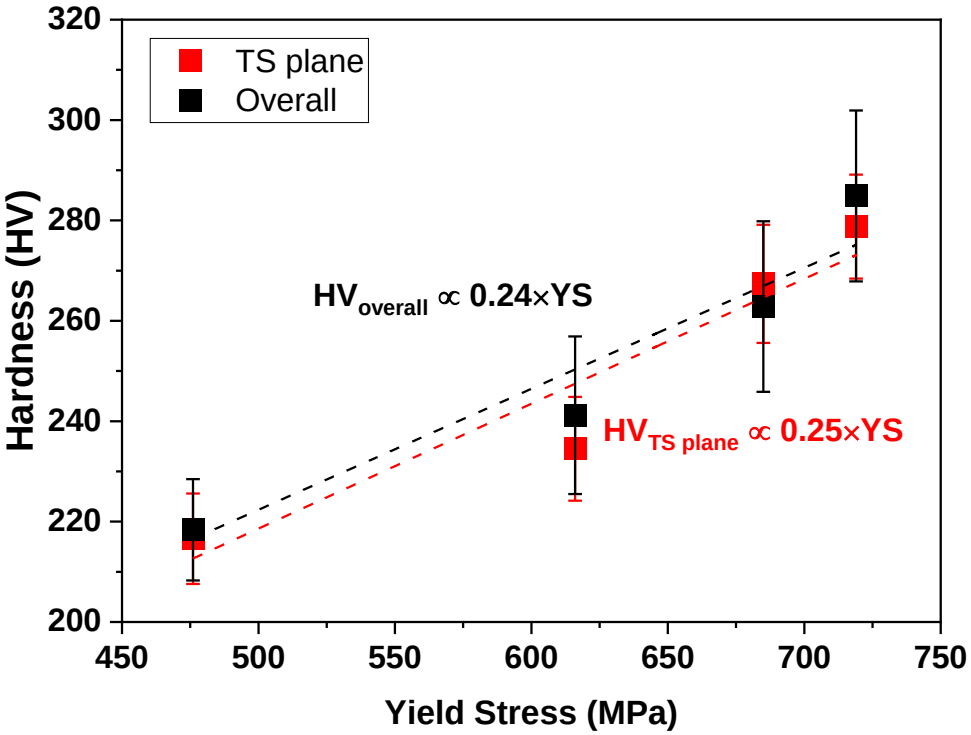

Figure 50. Hardness measured on the TS plane and the overall average hardness measured from all three planes in the 10–40%CF 316L materials as a function of their yield stress at 300 °C.

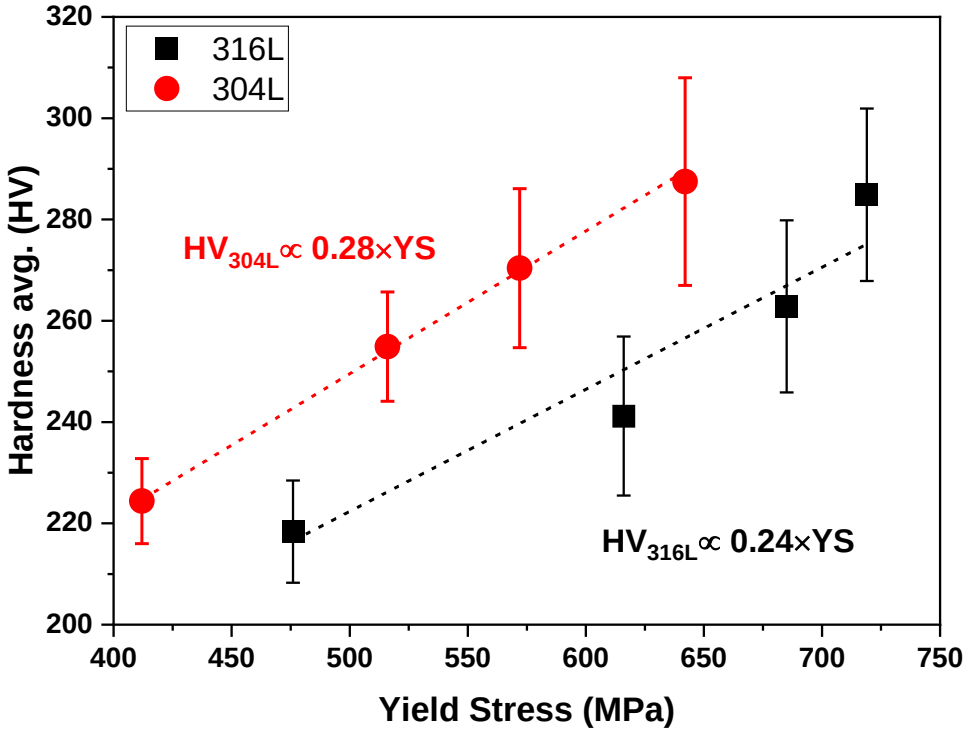

Figure 51. Comparison of the overall average hardness measured in the 10 – 40%CF 304L and 316L materials as a function of their yield stress at 300 °C.

4. Test Update

4.1 Experimental

4.1.1 Specimen Preparation

A general consensus summarized in our previous literature review [3] is that traditional constant load tensile specimen SCC initiation tests on 304L/316L may not be able to produce crack initiation, even in a highly cold worked condition. Complex strain paths and/or some amount of strain cycling appear to be necessary in promoting SCC initiation. BNCT specimen offers the flexibility to incorporate these two factors in the initiation testing. Its geometry allows for multi-axial loading at the notch bottom. It also enables strain cycling and enhanced deformation in the high-stress region near the notch bottom without risking the specimen failing due to transitioning to instability, as can happen with tensile specimens. As a result, the BNCT specimen geometry was selected for the first phase SCC initiation testing of CF 304L and 316L.

Standard 0.5T CT specimens with dimensions shown in Figure 52 were machined using electrical discharge machining (EDM). As illustrated in Figure 12, all specimens were extracted in the L-S orientation so that the cracking plane aligns with the crack growth direction in actual circumferential welds in the auxiliary piping. To remove the EDM recast layer and to allow documentation of crack initiation sites, the notch surface was manually polished to a 1 μm finish using special tools developed in-house. Before the start of the test, SEM examinations were performed to confirm the quality of polish on the notch surface. Figure 53 shows examples of acceptable surface finish on the notch bottom of the BNCT specimens. Although some polishing marks remain due to the challenging notch geometry, the delta ferrites were clearly revealed with clean edges in all specimens with mild contrast from the grain

microstructures. Some strain contrasts were also visible on the notch surface. If the polish did not reach such degree, the specimens will be returned for more polishing until an acceptable quality was confirmed via iterative SEM examinations.

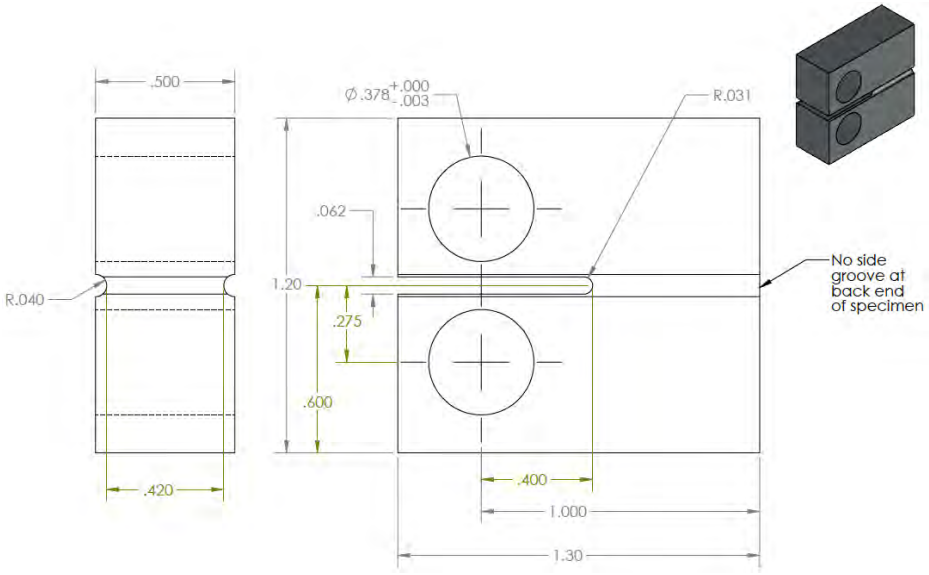

Figure 52. Dimensions of the BNCT specimens used for the SCC initiation testing (unit: inch).

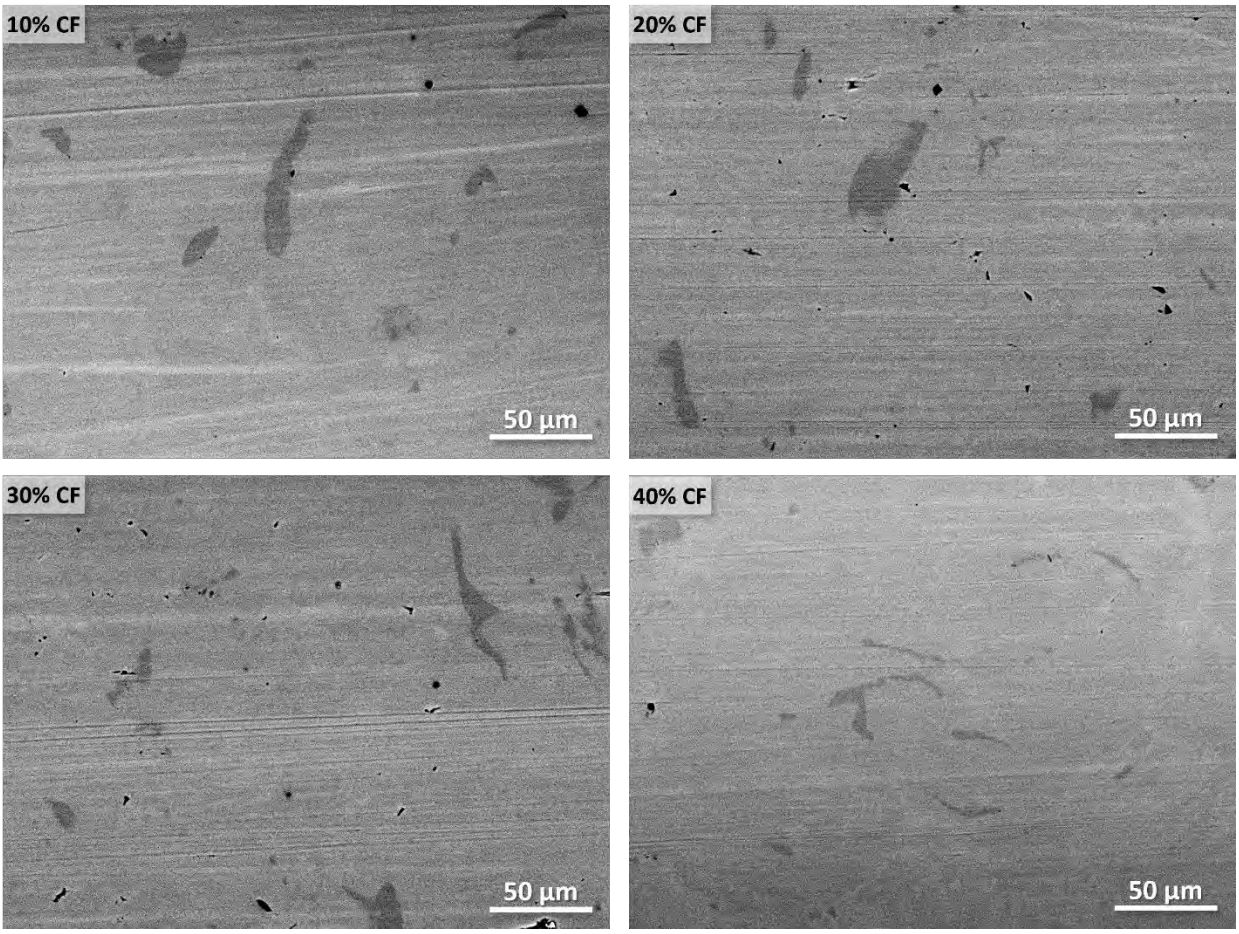

Figure 53. SEM-BSE images of the typical morphology of the pre-test polished surface of the notch bottom in 304L BNCT specimens under four different cold forging conditions.

4.1.2 SCC Initiation Testing

Due to the limit in testing capacity, SCC initiation testing in FY 2025 continued to focus on 304L using two mid-sized LWRS SCC test systems (denoted as LWRS2 and LWRS3 hereafter). The testing of 316L is planned to start in FY 2026 after these two mid-sized LWRS SCC test systems are upgraded to 12-specimen capacity by the end of FY 2025. The SCC test systems are equipped with active load control via a high-precision servo-electric load control system and in-situ monitoring using direct current potential drop (DCPD) technique. Detailed information on the development of the SCC test system and DCPD technique can be found in previous publications [26]. As shown in Figure 54, four BNCT specimens (one from each cold forging condition) are loaded in series in each test system. The test environment simulates PWR primary water with 1000 ppm of boron and 2 ppm of lithium at 300°C, the highest operating temperature reported for the SS auxiliary piping. Different DO content was selected for these two tests to evaluate the effect of oxygen on SCC initiation of cold worked 304L. In addition, one small SCC test system became available in the early summer of 2025, and we used it to start another SCC initiation test on two 304L BNCT specimens (one in 30%CF and the other in 40%CF condition) in hydrogenated water chemistry as a control test to the other two tests. This test is running at the same water chemistry as the other two tests (300°C, 1000 ppm B, 2 ppm Li) except with a dissolved hydrogen (DH) level of 30 cc/kg. The flow rate of all three tests is kept at 220 cc/min. Given the diameter of the tubing used for the primary water loop, this results in a flow speed of ~12 cm/s.

4.1.2.1 Gas Content Selection and Control

As discussed in Section 2.1, it is very challenging to determine the level of DO representative of the values that may be present in SS auxiliary piping. While performing discontinuous oxygen ingress in hydrogenated water better simulates the actual environment the auxiliary stainless steel piping may be exposed to in the French PWRs, it was decided to focus on constant DO levels as the first step to screen the effect of DO on SCC initiation of 304L. After discussing with the industry and reviewing literature data, two DO levels were chosen for the first test in the two test systems: 2 ppm DO in LWRS2, and 50 ppb DO in LWRS3. A number of SCC crack growth rate and low cycle fatigue studies on 304L/316L used these same DO contents for testing, allowing future comparison to be made with our SCC initiation testing results if applicable.

During the test, the DO content was maintained at the preset value via running an oxygen feeding tube to the water column of each test system. Mixed oxygen-nitrogen gas bottles with specific volume ratios were purchased and fitted with a 0-60 PSI regulator that was set to 15 PSI to ensure a steady flow out from the bottle. The tubing from the regulator to the water column gas inlet was then attached to an isolating valve in line with a metering valve. Once all connections were made, the lines were flushed of any potential residual gases before the test was started. The metering valve was then set at the calculated pressure needed to achieve the desired DO content in each test system. The combination of using the metering valve with a pressure regulator on the water column allows a steady pressure to be maintained on the oxygen feed thus constant DO content during testing. In addition, the outlet conductivity of the flow loop is being continuously monitored during testing, providing an indicator on the stability of the DO level in the test system.

Figure 54. The loading train with four BNCT specimens installed and spot welded with insulated Pt wires for in-situ DCPD monitoring of crack initiation and growth.

An estimate of the electrochemical potential (ECP) of the 304L specimens in the tested water chemistries was made according to EdF's ECP model (Figure 55). A few important indications can be drawn from this figure. (1) Trace amount of DO between 1 ppb and 40 ppb leads to the most profound change in the ECP of SS. (2) The ECP of SS becomes independent of flow rate when the DO content in primary water exceeds 40 ppb. (3) At a fixed flow rate such as 12 cm/s (similar to the flow rate in our tests), the ECP of SS decreases with increasing temperature in both DO and DH water chemistries. Using this model, the ECP estimated for the 304L specimens tested in this SCC study with 2 ppm DO and 50 ppb DO are ~-0.08 mV and slightly below -0.2 mV, respectively. However, low levels of DO, such as 50 ppb, are known to be difficult to maintain consistently in the water loop because oxygen would be partially consumed during water recirculation, even when it is fed at a constant pressure and injected at a high flow rate. As a result, the DO in the test system is likely below 50 ppb, which would lead to a lower ECP, likely somewhere between -0.6 and -0.2 mV, for the 304L specimens tested in the 50 ppb DO-containing water. Meanwhile, the ECP of the specimens tested in the DH water chemistry containing 30 cc/kg H_2 is estimated to be between -0.7 and -0.8 mV according to EdF's model. Such water chemistry represents the typical reducing water condition implemented in the SS auxiliary piping systems in Japan and U.S. PWRs, and serves as a reference to the tests in DO-containing water chemistries.

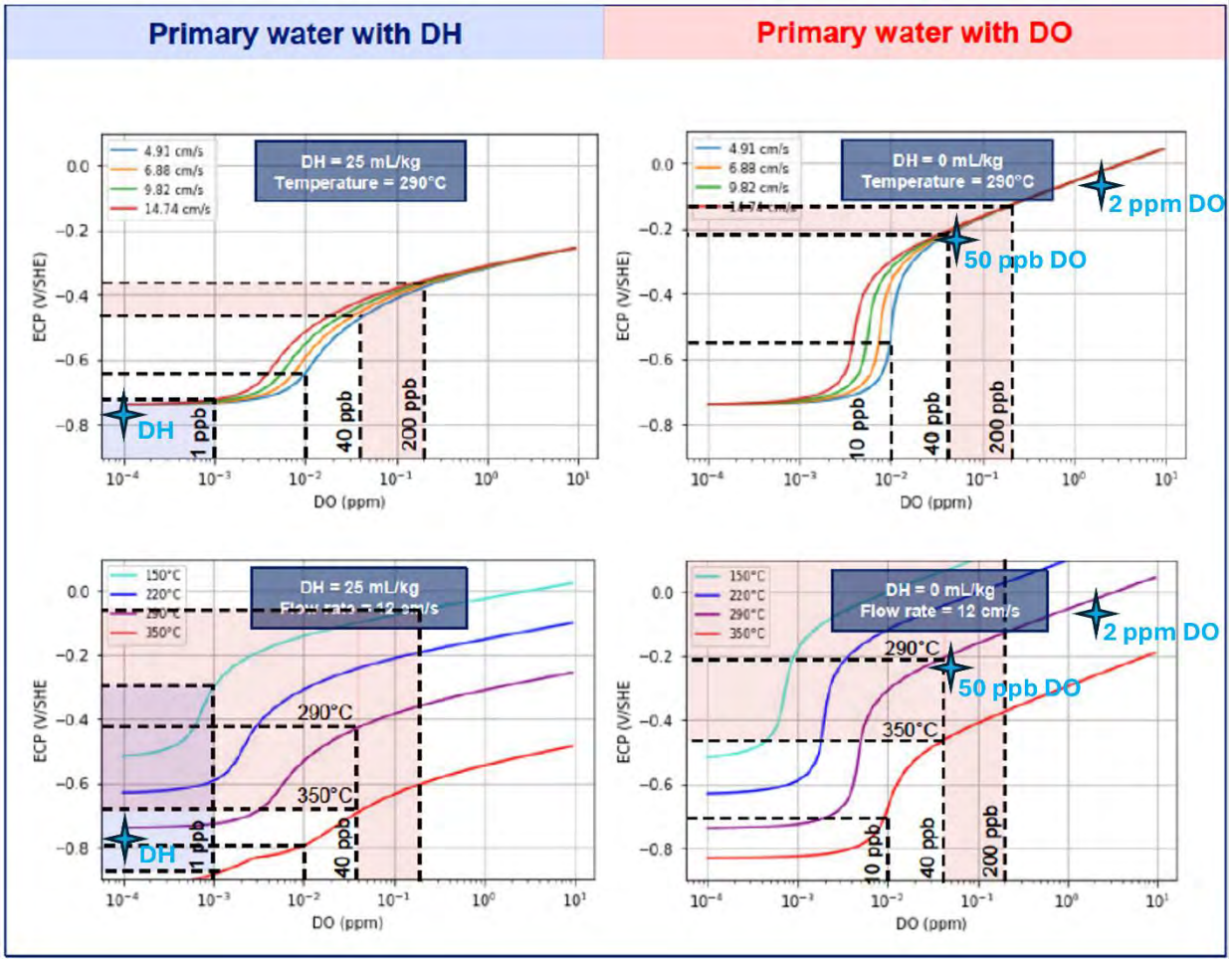

Figure 55. EdF's electrochemical potential (ECP) modeling of the ECP of SS in PWR primary water as a function of dissolved gas content, temperature, and flow rate (*private communication from EDF R&D, used with permission*). Estimated ECP values from this model for the SS 304L specimens tested in the three water chemistries at PNNL are also highlighted.

4.2 304L SCC Initiation Test Progress

4.2.1 SCC Initiation Test in PWR Primary Water with 2 ppm DO

An overview of the DCPD-indicated crack length evolution from the notch of the four cold forged 304L specimens CT 304–307, one each from the 10, 20, 30, and 40% CF condition, is provided in Figure 56. This test was started at constant load with a stress intensity (*K*) of ~30 MPa√m for the four specimens. The *K* level of the BNCT is better described as a "pseudo *K*" because it is calculated assuming a sharp crack is present across the specimen, rather than a blunt notch with a smooth surface. The *K* of 30 MPa√m was chosen as it has been commonly used for SCC crack growth rate testing of cold worked stainless steels, and is considered a reasonable start point for the SCC initiation test.

The test at a constant K of 30 MPa√m was performed for the first ~800 hours. The DCPD-indicated crack length evolution trend during this period were generally flat or slightly negative. The latter should be phantom and is likely associated with internal strain redistribution under loading and the oxides formation on the notch surface. Since many studies in the literature pointed out that constant load may not be sufficient to induce SCC initiation in 304L/316L even in highly cold worked conditions, it was decided to stop the test after reaching 800 hours of exposure to examine the notch surface of all specimens for precursor damage and initiation indications. The results are summarized in Figures 57–60 for the 10%, 20%, 30%, and 40%CF specimen, respectively. Although not obvious in these low-magnification images, the formation of oxides was confirmed on the notch surface of all specimens. No prominent evidence of intergranular corrosion was observed in any of these specimens. It is worth noting that a high density of slip bands was identified on the notch surface of the 10% and 20%CF 304L specimens, with examples shown in the lower images in Figures 57–58. In comparison, no slip bands were observed in the 30% and 40%CF 304L specimens (Figures 59–60). These observations suggest that the constant load at 30 MPa√m had led to substantial localized hardening in the notch region of the 10% and 20%CF 304L specimens, but to a much lesser degree in the 30% and 40%CF 304L specimens, which is consistent with the lower YS measured for the 10% and 20%CF 304L materials (Section 3.3.5). Was et al. [27] has long been suggesting that dislocation channels, presented in the form of stacked slip planes, have a key role in irradiation-assisted SCC initiation in austenitic stainless steels. When encountering a grain boundary, the dislocation channels (DC) can either transfer to a neighboring grain (i.e., continuous DC) or terminate at the grain boundary (i.e., discontinuous DC), resulting in very different strain/stress states at the DC-GB site. The discontinuous DC-GB sites exhibit much higher stress and have been shown to lead to a much higher probability of cracking than that for continuous DC-GB sites. In addition, it has been reported that a high propensity for crack initiation was seen when discontinuous dislocation channels intersect MnS inclusions in 304L [28]. Since MnS inclusion has been confirmed in the 304L being tested in this study, it would also be of interest to evaluate the interactions between DO level, precipitates, and loading condition to obtain a better understanding of SCC initiation mechanism in these CF 304L materials when applicable.

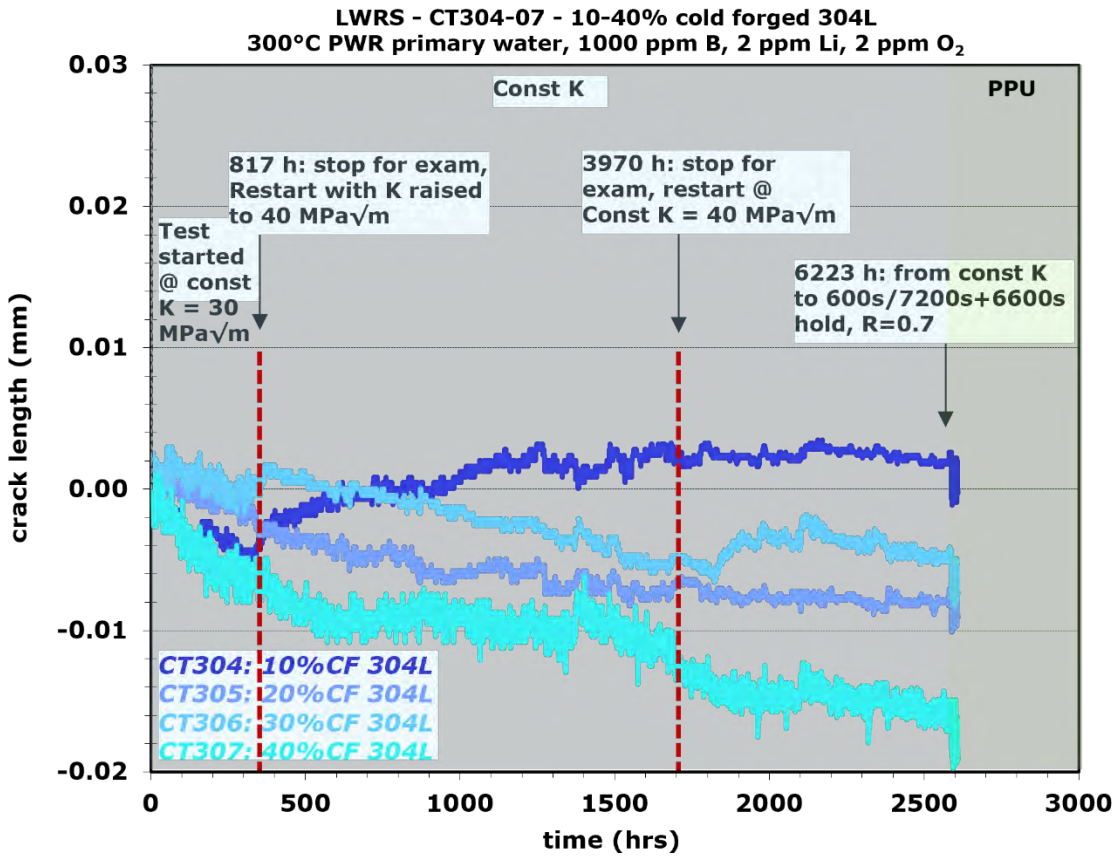

Figure 56. Test overview of the DCPD indicated crack length evolution in 10–40% CF 304L BNCT specimens in 300°C PWR primary water containing 2 ppm DO. The testing is ongoing as of the writing of this report.

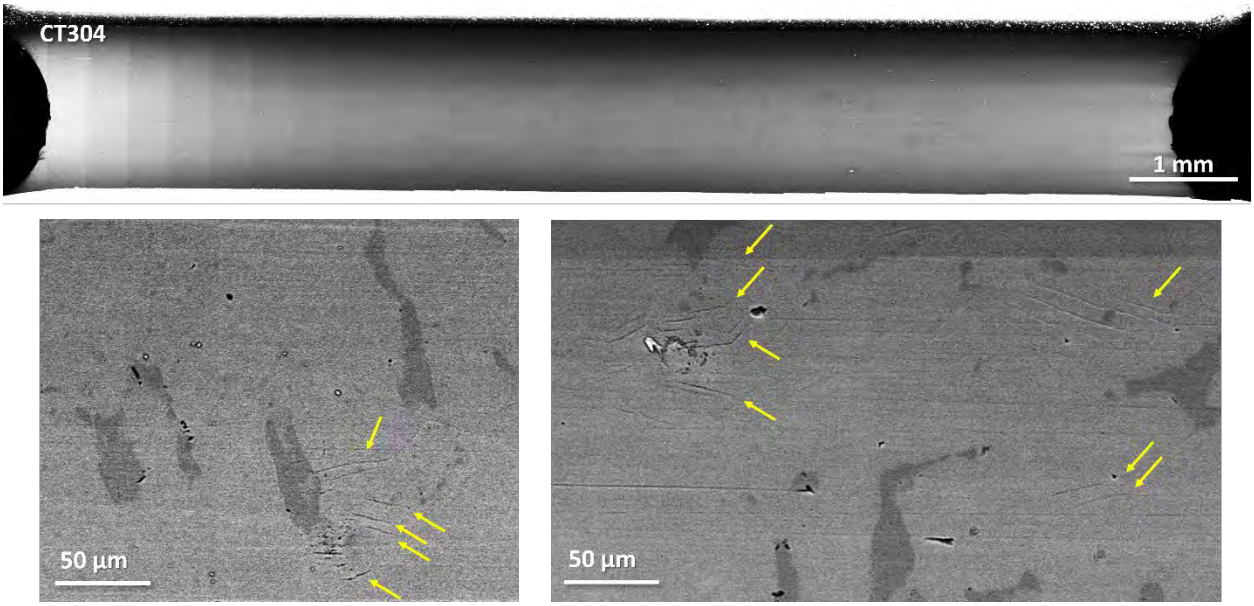

Figure 57. SEM-BSE montage image (upper) of the notch surface of the 10%CF 304L BNCT specimen CT304 after 815 hours of exposure in 300°C PWR primary water containing 2 ppm DO, with higher

magnification images at randomly selected sites on the notch surface (lower). Observed slip bands are highlighted by arrows.

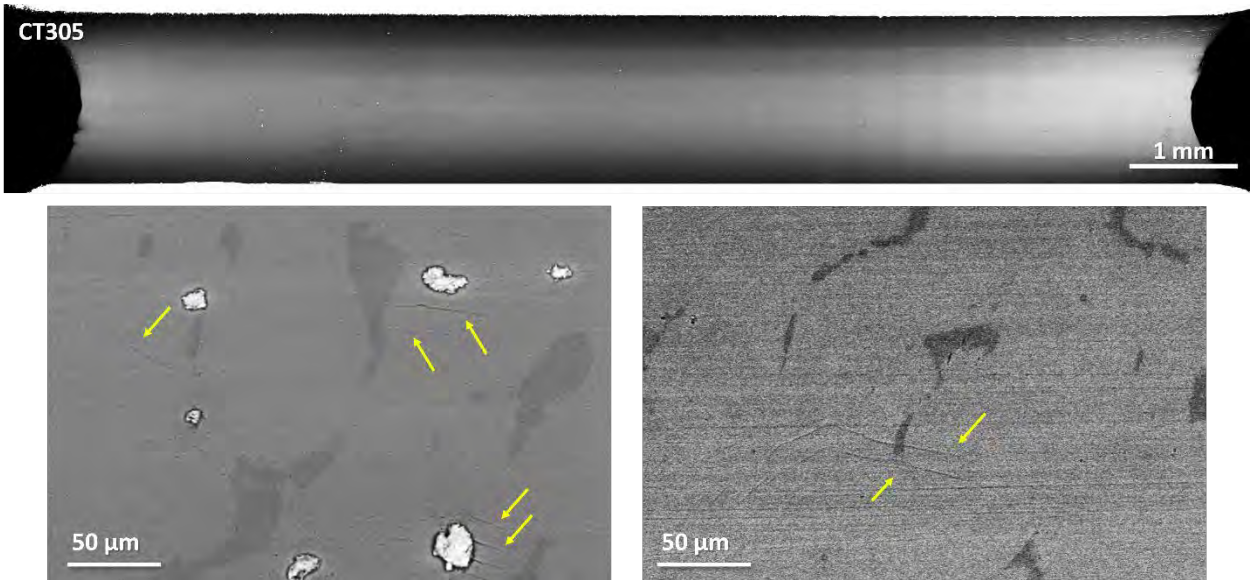

Figure 58. SEM-BSE montage image (upper) of the notch surface of the 20%CF 304L BNCT specimen CT305 after ~815 hours of exposure in 300°C PWR primary water containing 2 ppm DO, with higher magnification images at randomly selected sites on the notch surface (lower). Observed slip bands are highlighted by arrows.

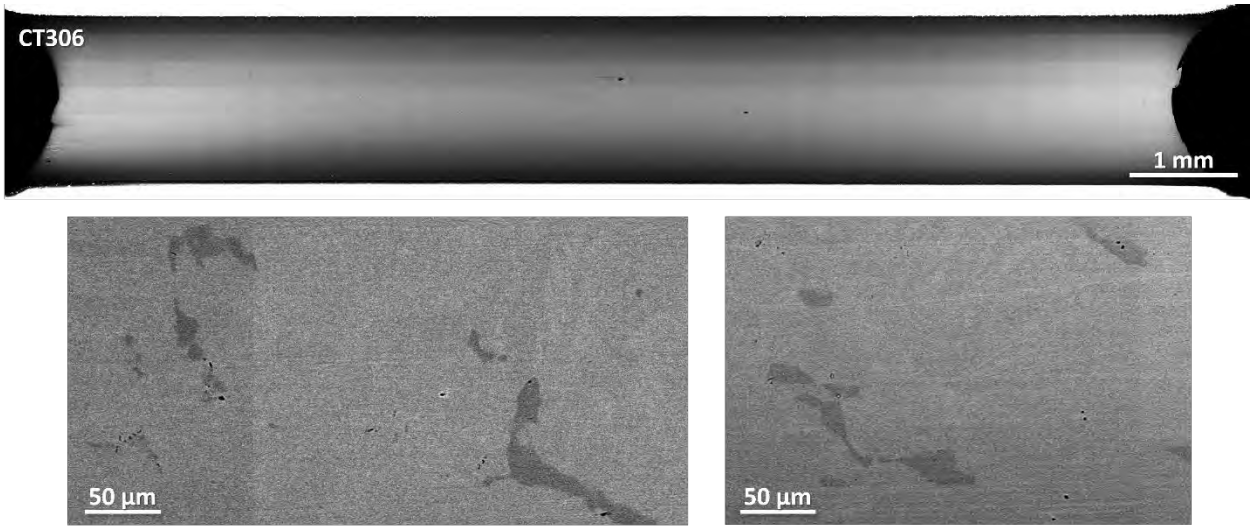

Figure 59. SEM-BSE montage image (upper) of the notch surface of the 30%CF 304L BNCT specimen CT306 after ~815 hours of exposure in 300°C PWR primary water containing 2 ppm DO, with higher magnification images at randomly selected sites on the notch surface (lower).

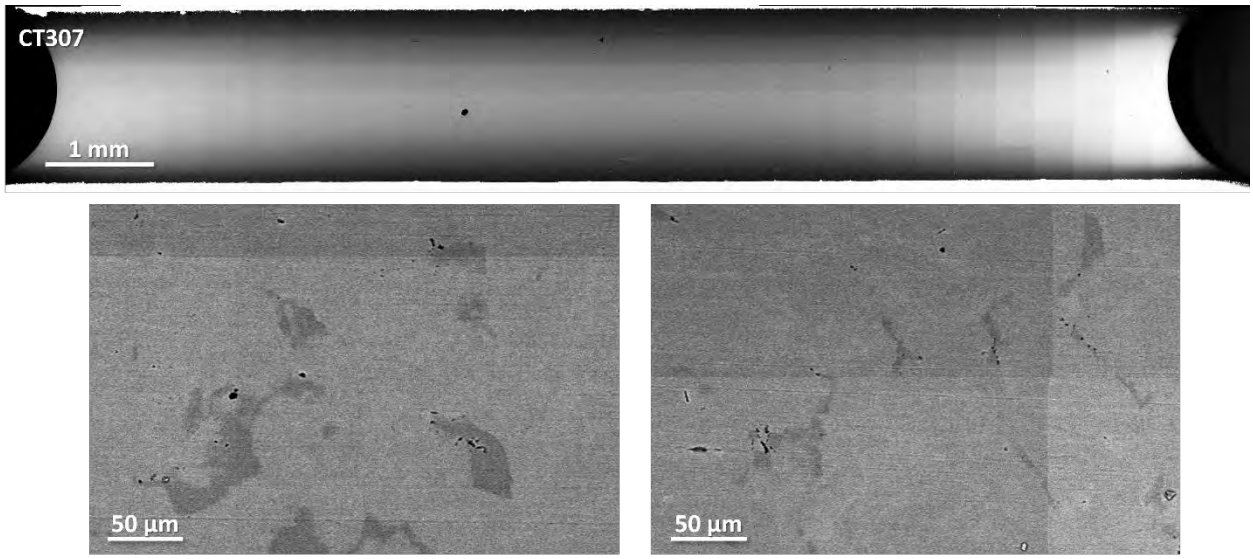

Figure 60. SEM-BSE montage image (upper) of the notch surface of the 40%CF 304L BNCT specimen CT307 after ~815 hours of exposure in 300°C PWR primary water containing 2 ppm DO, with higher magnification images at randomly selected sites on the notch surface (lower).

Based on the observation above, it was decided to increase the constant load from 30 to 40 MPa√m on all specimens after the restart of the test. As shown in Figure 56, the test was maintained at this constant K condition for ~3,000 hours until the specimens were removed for another notch surface examination. No DCPD-indication of macroscopic crack initiation was detected in any specimen in this interim. However, evidence of small crack nucleation was found in all specimens after they were removed from testing for SEM examination. As shown in Figures 61–64, short cracks were observed in all specimens, with obviously opened cracks marked in red, and those having a darker contrast than the extensive shallow slip bands classified as possible cracks and marked in green in the montage images. Higher magnification images taken in the BSE and SE modes of obvious cracks at selected sites are also provided. The BSE images better reveal the contrast between different phases (e.g., the matrix and delta ferrites and oxidation morphology), while the SE images better capture the topological difference between the cracks and slip bands. It appears that the density of obvious cracks increased with increasing cold work, but their presence is still scattered, and no evidence of crack coalescence forming long cracks was found in any of these specimens. While the surface finish made it challenging to determine the cracking mode for all the cracks, it appears both intergranular (IG) and transgranular (TG) cracks are present. As shown at Sites 2 and 3 in Figure 62, a series of slip bands was found to terminate at the open cracks, in good agreement with literature where the discontinuous DC-GB sites have been identified as preferred sites for SCC initiation. In addition, open cracks were also found at the interface between delta ferrite and the matrix, such as the one presented at Site 3 in Figure 61. However, it should be noted that only very limited number of cracks were found to be associated with delta ferrites in the four observed specimens, suggesting that the delta ferrites are not popular sites for SCC initiation in this test. Pitting corrosion was also evidenced in these specimens, with examples shown at Sites 1 and 2 in Figure 61. Such sites often contain a series of parallel but closely spaced cracks, indicative of previous slip bands, and are accentuated by a ring of oxides circling them, as well as darker oxides residing on the flanks of opened cracks.

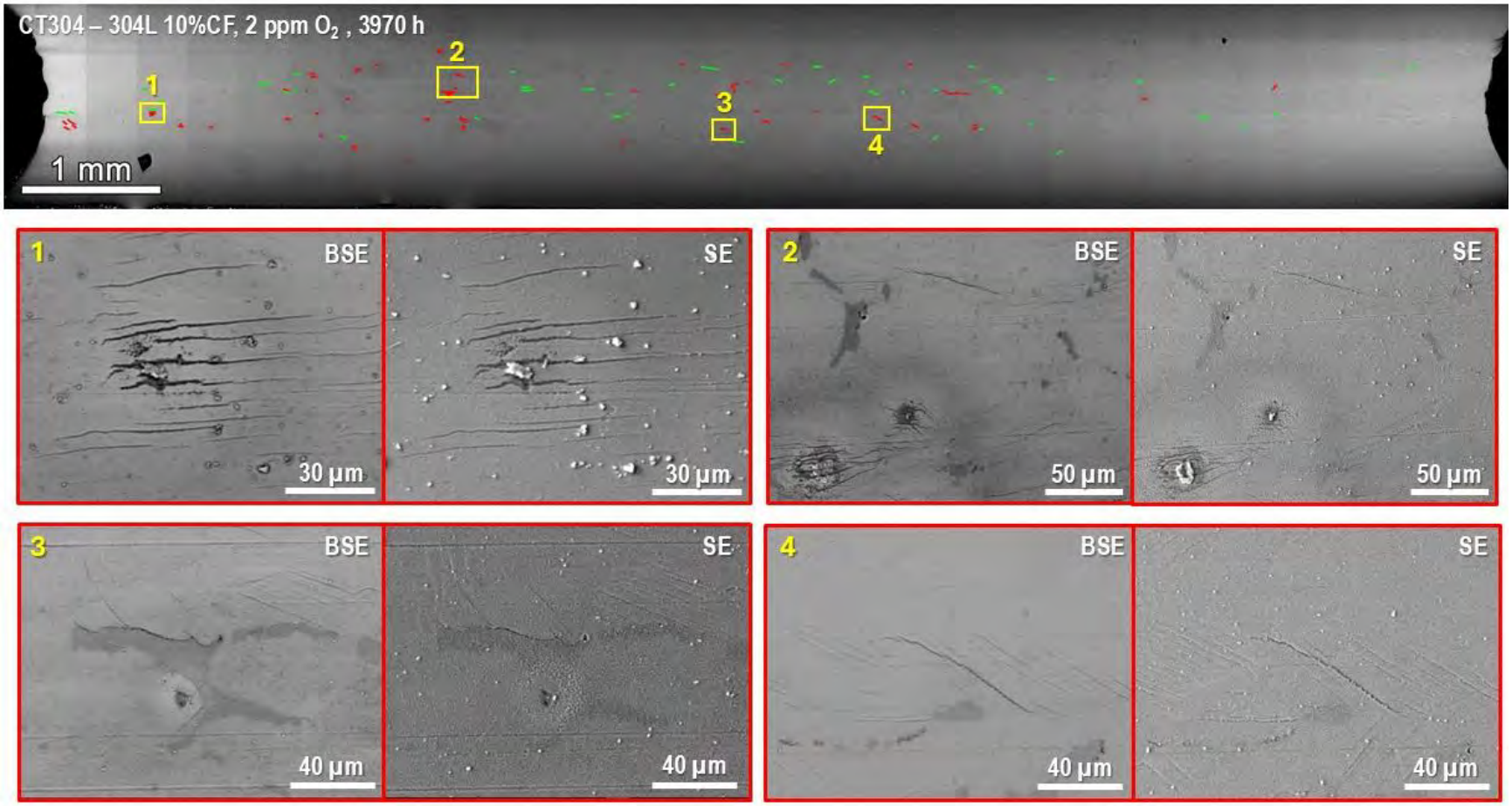

Figure 61. SEM-BSE montage image (upper) of the notch surface of the 10%CF 304L BNCT specimen CT304 after 3970 hours of exposure in 300°C PWR primary water containing 2 ppm DO, with obvious cracks marked in red and possible cracks marked in green. Higher magnification images of four crack-containing sites were also presented (lower).

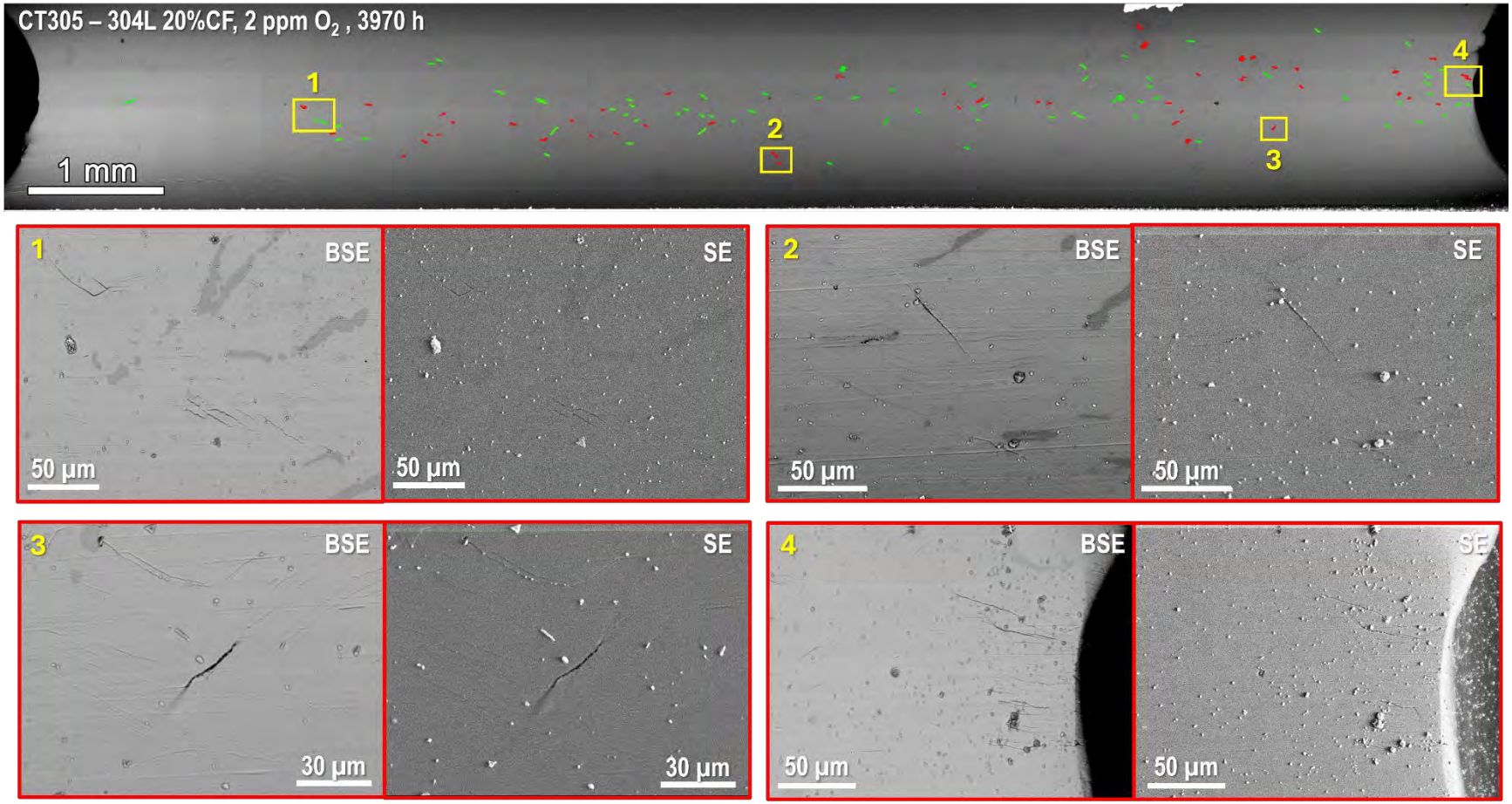

Figure 62. SEM-BSE montage image (upper) of the notch surface of the 20%CF 304L BNCT specimen CT305 after 3970 hours of exposure in 300°C PWR primary water containing 2 ppm DO, with obvious cracks marked in red and possible cracks marked in green. Higher magnification images of four crack-containing sites were also presented (lower).

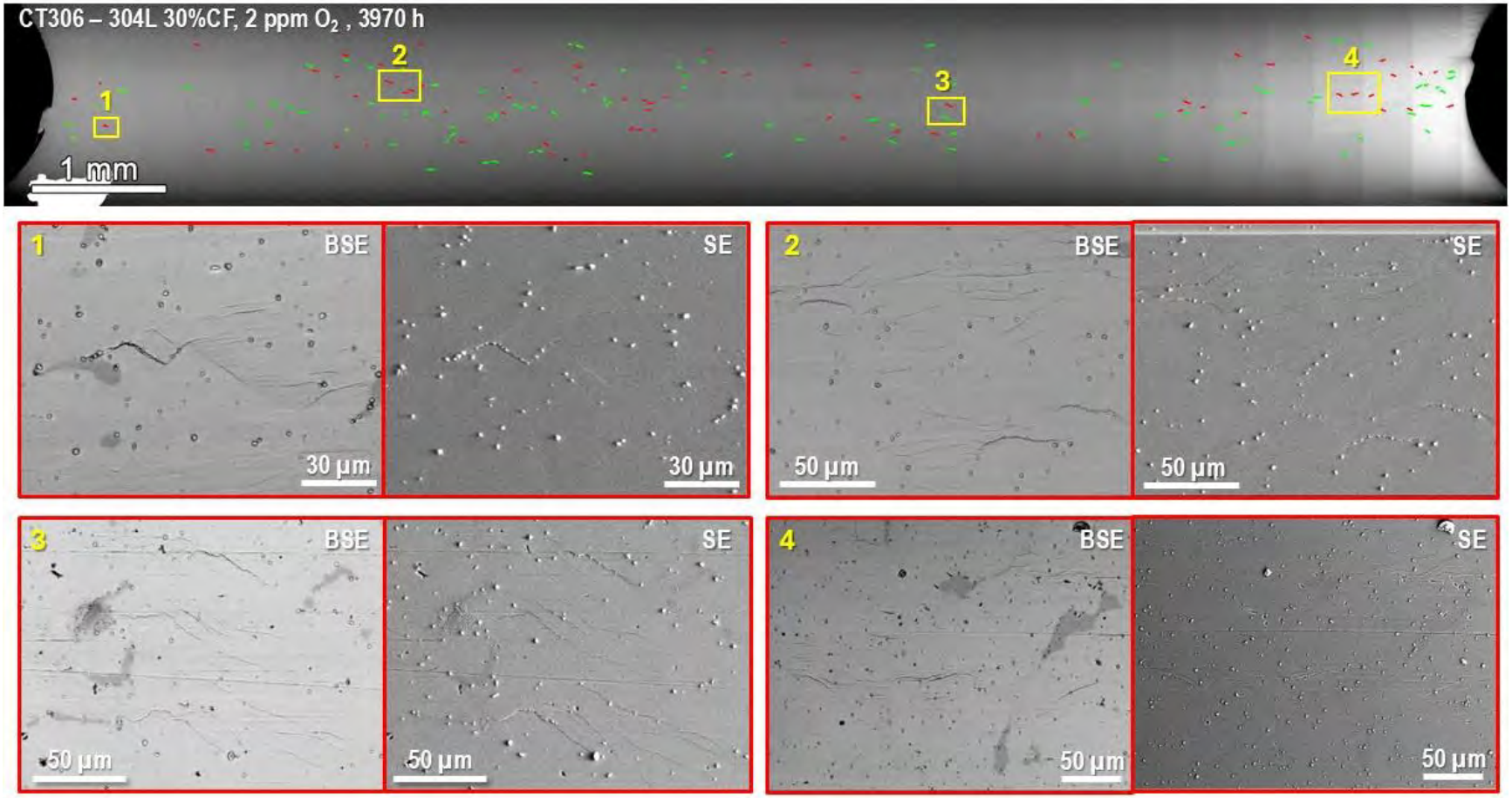

Figure 63. SEM-BSE montage image (upper) of the notch surface of the 30%CF 304L BNCT specimen CT306 after 3970 hours of exposure in 300°C PWR primary water containing 2 ppm DO, with obvious cracks marked in red and possible cracks marked in green. Higher magnification images of four crack-containing sites were also presented (lower).

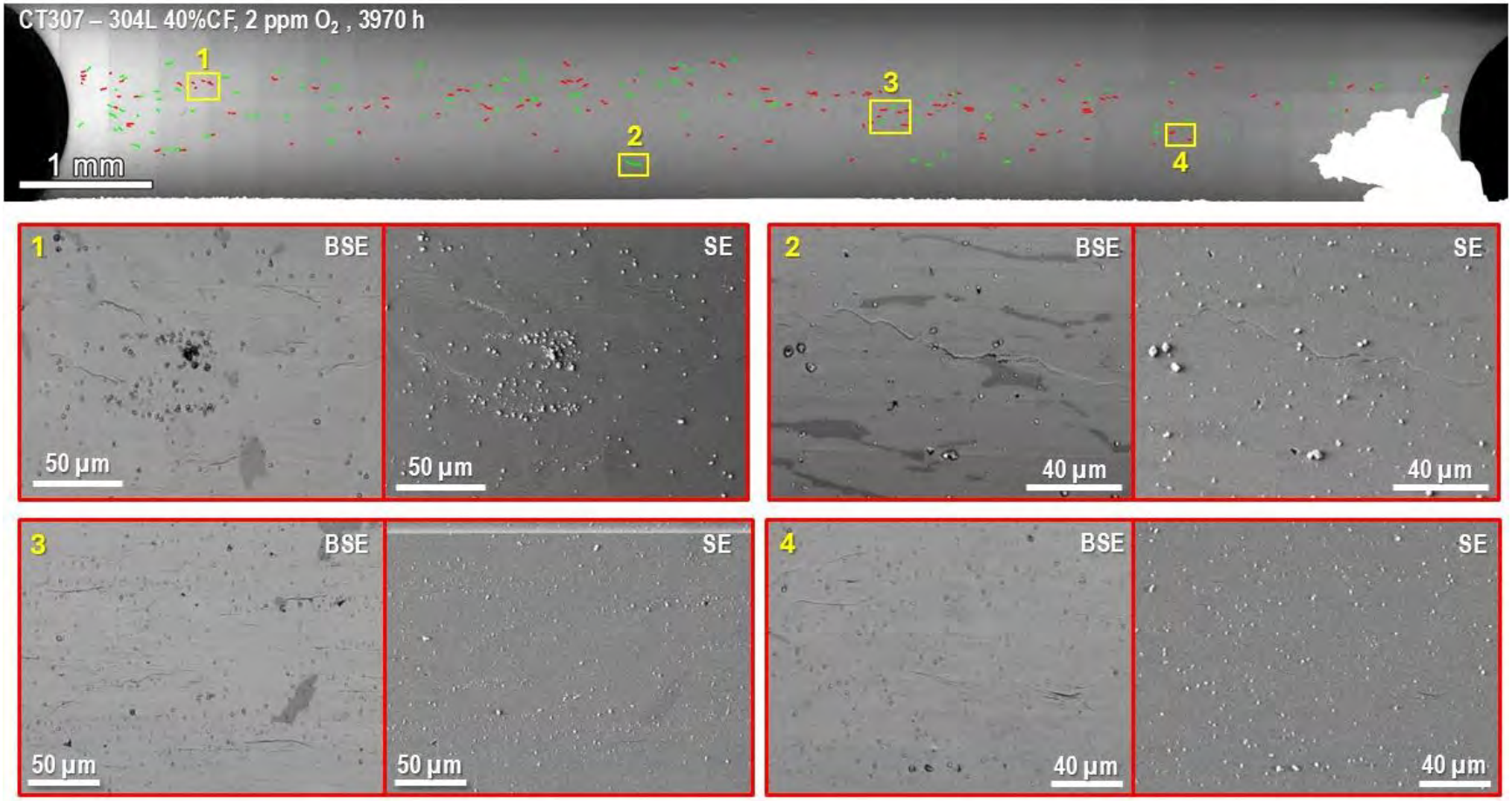

Figure 64. SEM-BSE montage image (upper) of the notch surface of the 40%CF 304L BNCT specimen CT307 after 3970 hours of exposure in 300°C PWR primary water containing 2 ppm DO, with obvious cracks marked in red and possible cracks marked in green. Higher magnification images of four crack-containing sites were also presented (lower).

Since evidence of cracking was found in all specimens during the second SEM examination, it was decided to return the specimens to testing at the same constant K condition. However, no change in the crack length evolution was observed in any of these specimens after another ~2,200 hours, indicating slow to negligible crack growth. As a result, it was decided to introduce periodic partial unloading (PPU) starting at 6,223 hours to assess if dynamic strains could accelerate SCC initiation in these 304L specimens. A search was conducted to identify suitable load cycling conditions that simulate a realistic thermal cycling scenario in the plant. While data is scarce in the open literature, one study was found to contain field monitoring data on thermal cycling of safety injection line in a French NPP [Blondet 2002]. By referencing Figure 65, the parameters of the PPU cycles were determined with an R ratio of 0.7, a rise time of 600 seconds, a fall time of 7200 seconds, and a hold time at a maximum load of K = 40 MPa√m for 6600 seconds. This condition generates six load cycles per day. As shown in Figure 56, currently the test is only ~50 hours into the PPU testing phase, and no immediate change in crack length has been detected by DCPD in any specimen yet despite larger fluctuation in the values in response to the implemented load cycles. The plan is to continue the PPU for at least of total of 1,000 hours and then remove the specimens for another SEM examination. New testing plan on these specimens will be devised based on the results of the next SEM examination.

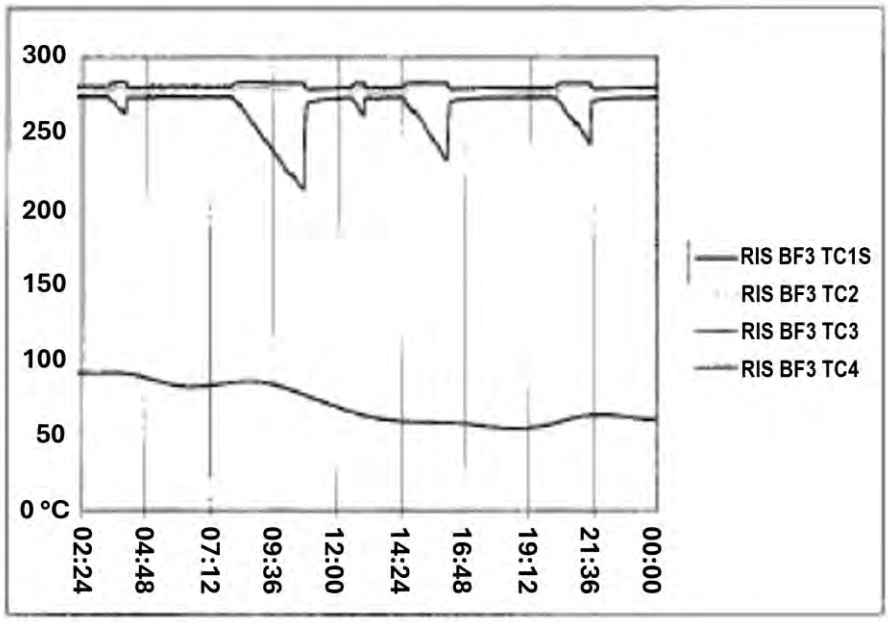

Figure 65. Axial instability thermal cycling on Blayais 1 – cold leg 3 injection line [29].

4.2.2 SCC Initiation Test in PWR Primary Water with 50 ppb DO

This test was started at the same loading condition as the test with 2 ppm DO on another set of four CF 304L specimens (i.e., CT308–311), one each from the 10%, 20%, 30%, and 40% CF condition. The DO content of this test is maintained at 50 ppb, but as discussed in Section 4.1.2.1, the actual DO in the system is likely lower. As shown in Figure 66, constant load at a "pseudo *K*" of ~30 MPa√m is applied on all the specimens for the first ~1,000 hours of the test. Unfortunately, there were some issues with the DCPD wires used on CT311 since the start of the test, giving erroneous readings and crack length prediction. The test was stopped a few times to debug and rebuild the feedthrough for the wires but did not successfully resolve it. Therefore, the DCPD crack length response of this specimen is not included in the figures for this reporting. Nevertheless, according to the SEM montage performed after 4,065 hours of

exposure, this specimen showed no macroscopic crack initiation. As a result, it can be reasonably assumed that the DCPD response of this specimen is similar to that of the other three specimens. As can be seen in Figure 66, a generally flat trend in the crack length evolution was observed for all specimens during the 30 MPa/m constant K period. Based on the observation results of the notch surface of CT304-07 after the first ~800 hours, no cracking is expected in these four specimens either, so the decision was made to directly increase the load in this test from 30 to 40 MPa/m at 1,368 hours without stopping the test to document the notch surface of these specimens. The latter portion of Figure 66 shows the DCPD-indicated crack length evolution of CT308-310 in the following ~3,000 hours, again no indication of crack initiation was observed in any specimens. The specimens were then removed from the test after a total exposure of 4,065 hours for their first SEM examination of the notch surface, and the results are summarized in Figures 67–70 for the CT308–311, respectively. A lesser density of obvious cracks and possible cracks (marked in red and green, respectively, in the montage images of the entire notch bottom surface) were found in these specimens as compared to CT304–307 exposed to primary water containing a higher DO content, but the number of cracks appears to have increased with the increase in cold work level. In general, the cracks in CT308–311 appear tighter and shallower than those found in CT304–307, with no indication of pitting corrosion in any of these specimens. Interestingly, it should also be noted that the notch surface of all specimens appears to be covered by thicker oxides, which obscured the delta ferrites that were visible on the surface under SEM before the test. These observations suggest that decreasing DO content in primary water likely allowed a more protective oxide layer (or layers) to form on the specimen surface, and reduced the SCC initiation susceptibility of 304L by lowering its ECP.

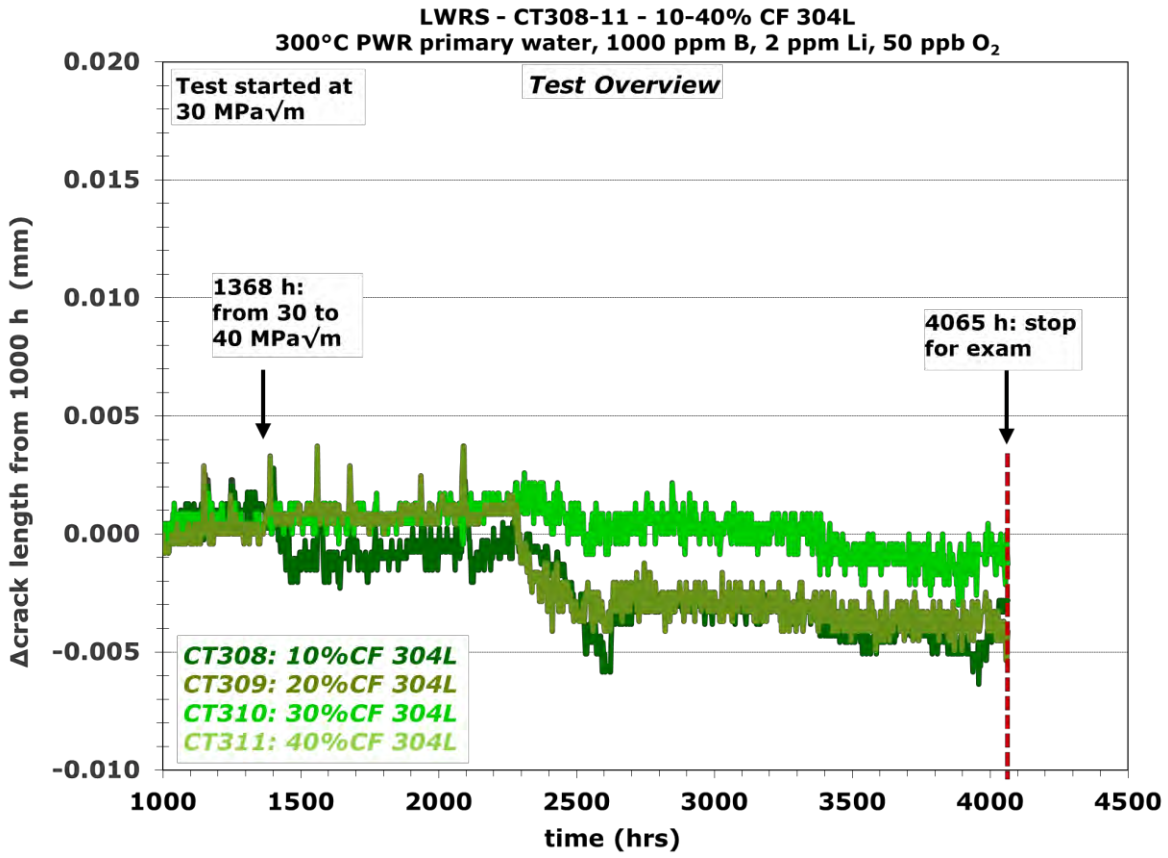

Figure 66. DCPD indicated crack length evolution of the first 4065 hours of constant K testing of the 10–40% CF 304L BNCT specimens CT308–311 in 300°C PWR primary water containing 50 ppb O_2.

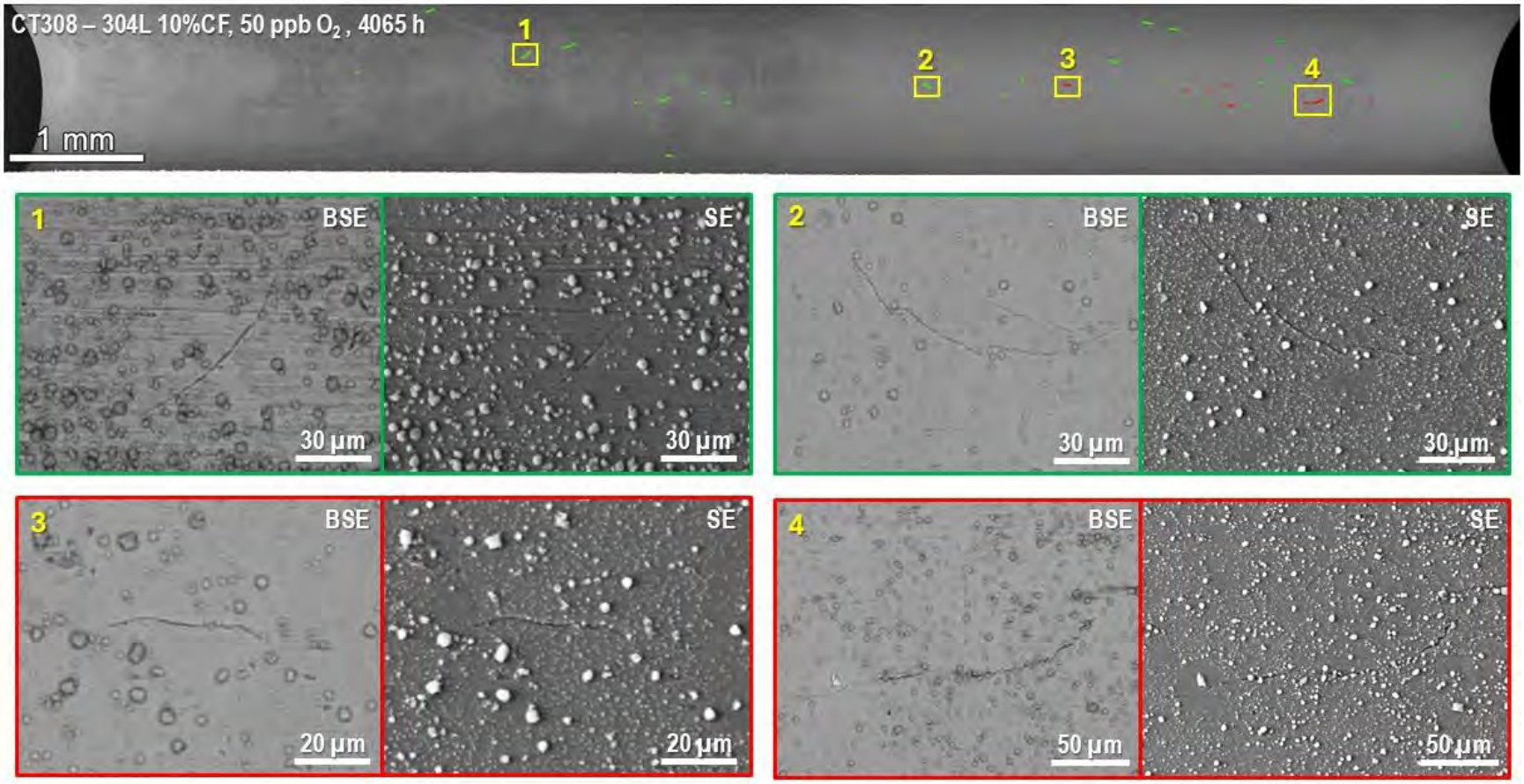

Figure 67. SEM-BSE montage image (upper) of the notch surface of the 10%CF 304L BNCT specimen CT308 after 4065 hours of exposure in 300°C PWR primary water containing 50 ppb DO, with obvious cracks marked in red and possible cracks marked in green. Higher magnification images of four crack-containing sites were also presented (lower).

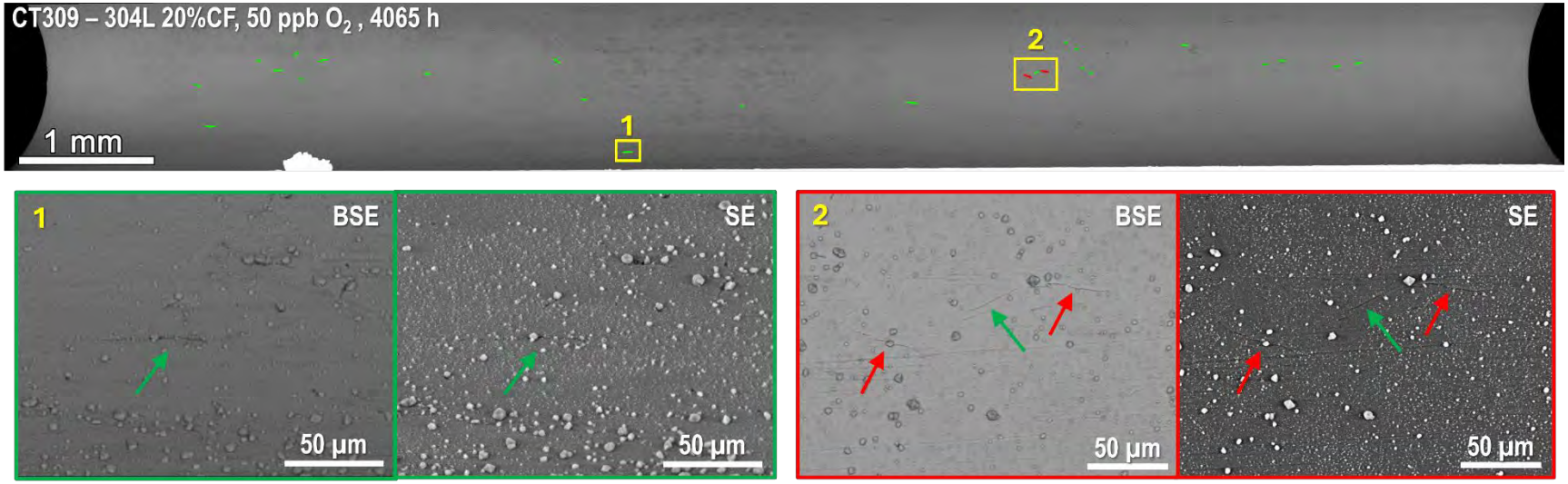

Figure 68. SEM-BSE montage image (upper) of the notch surface of the 20%CF 304L BNCT specimen CT309 after 4065 hours of exposure in 300°C PWR primary water containing 50 ppb DO, with obvious cracks marked in red and possible cracks marked in green. Higher magnification images of two crack-containing sites were also presented (lower).

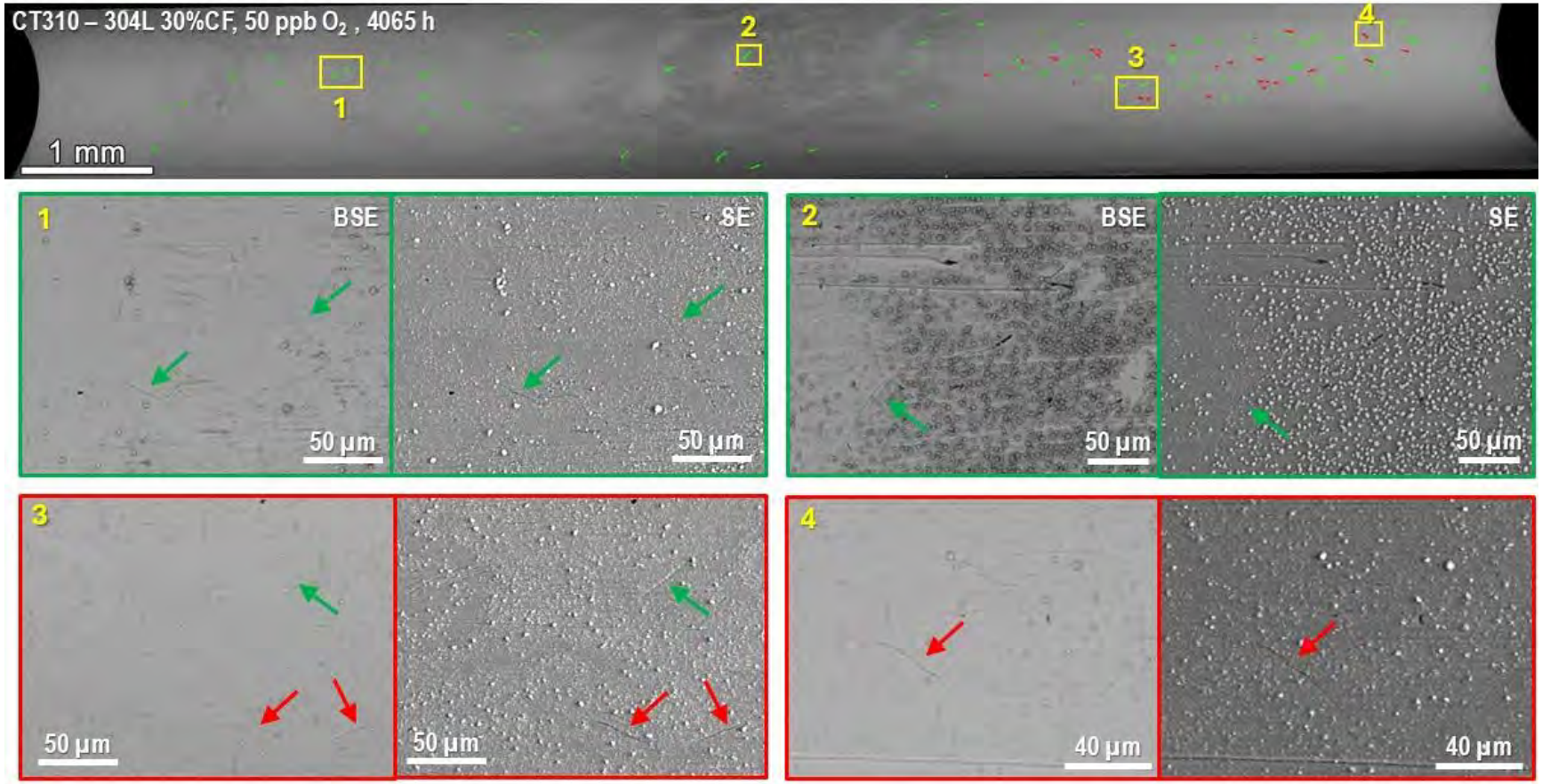

Figure 69. SEM-BSE montage image (upper) of the notch surface of the 30%CF 304L BNCT specimen CT310 after 4065 hours of exposure in 300°C PWR primary water containing 50 ppb DO, with obvious cracks marked in red and possible cracks marked in green. Higher magnification images of four crack-containing sites were also presented (lower).

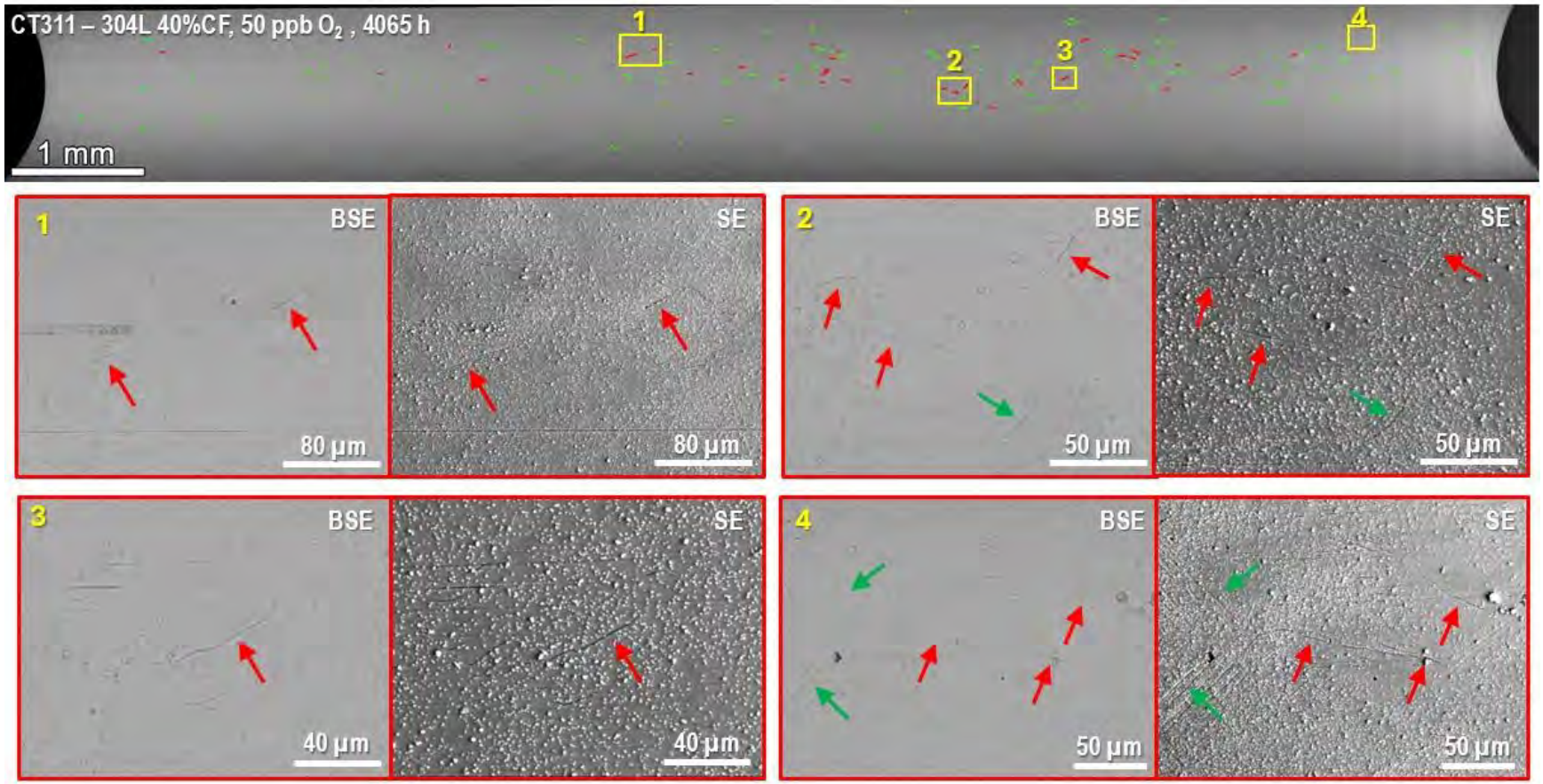

Figure 70. SEM-BSE montage image (upper) of the notch surface of the 40%CF 304L BNCT specimen CT311 after 4065 hours of exposure in 300°C PWR primary water containing 50 ppb DO, with obvious cracks marked in red and possible cracks marked in green. Higher magnification images of four crack-containing sites were also presented (lower).

The test was restarted on CT308–311 after the completion of SEM examination mentioned above. Similar to what was done for CT304–307, these specimens were kept at a constant pseudo K of 40 MPa/m for another ~1,300 hours. Even though a mild increase in crack length was indicated for CT309 and CT310 between 4780 and 5380 hours, the actual crack growth rate (CGR) is still below 3×10^{-9} mm/s, suggesting very slow crack growth if there was any. It was then decided to evaluate the effect of load cycling on these specimens using the same pattern performed on CT304–307 in the 2 ppm DO test. Unfortunately, the load cycling was accidentally set using an initial R ratio of 0.5 instead of 0.7, and the hold was not enabled for the first three days until the correct load cycling parameters were implemented. As a result, the specimens underwent three days of low cycle fatigue at a frequency of ~0.00013 Hz. Since this cycling condition is very gentle and the period of fatigue is relatively short, it is considered that it had little effect on the existing cracks, but targeted characterization will be performed at the next test interruption to differentiate its actual impact on crack initiation of these specimens. As of the time of this writing, the test has been under the same PPU condition as the one implemented on CT304–307 for ~350 hours with no change in crack length observed for CT308 and CT309. Interestingly, a mild increasing trend was observed in CT310, but the absolute value of CGR is below 6×10^{-10} mm/s, indicating no or very limited crack growth. Like the test in 2 ppm DO-containing water, the current plan is to maintain the PPU for a total of 1,000 hours and then remove the specimens from the test for another notch surface examination. The obtained results will be compared to those obtained from CT304–307 and will be used to guide the development of the next-phase testing.

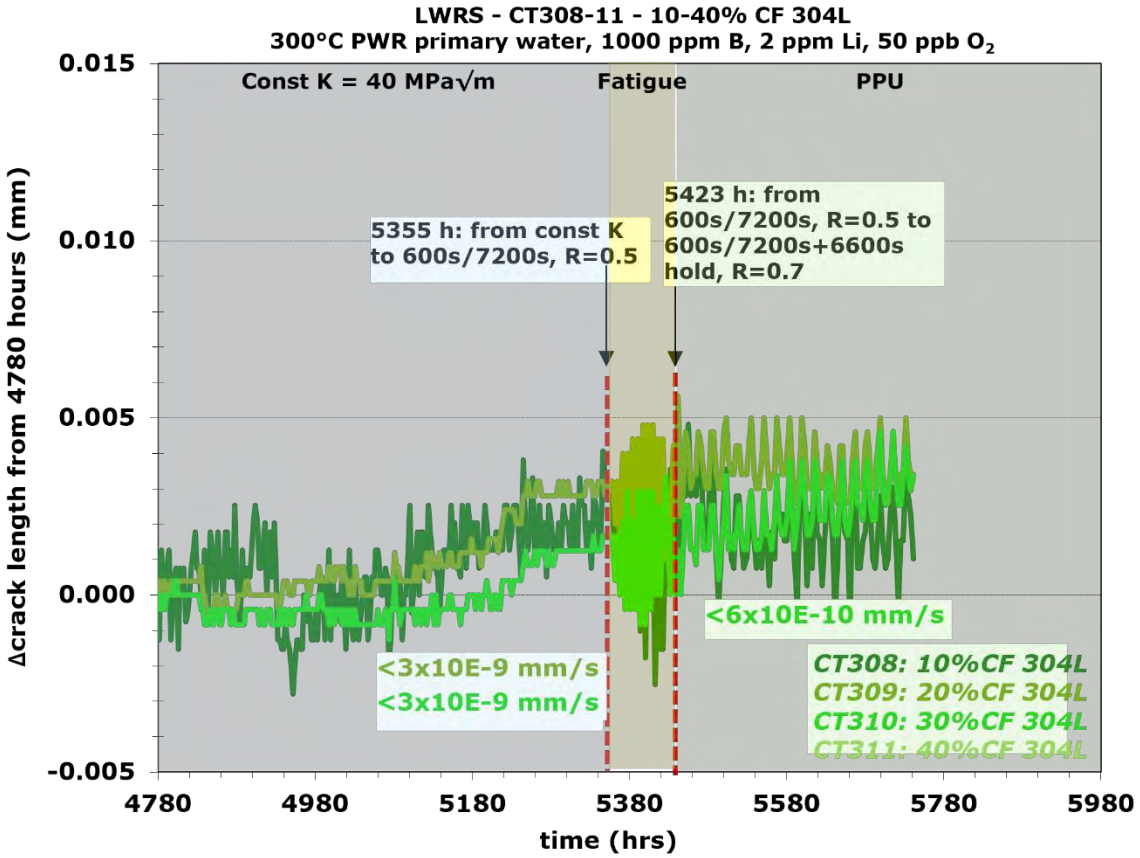

Figure 71. DCPD indicated crack length evolution starting from 4780 hours of the 10–40% CF 304L BNCT specimens CT308–311 in 300°C PWR primary water containing 50 ppb O_2. The testing is ongoing as of the writing of this report.

4.2.3 SCC Initiation Test in PWR Primary Water with 30 cc/kg H_2

As discussed in Section 4.1.2, the third SCC initiation test was started this summer in a small autoclave on two CF 304L specimens, one in 30% CF condition and the other in 40% CF condition, in 300°C PWR primary water containing 30 cc/kg H_2. Figure 72 provides an overview of the DCPD indicated crack length evolution of these two specimens. To date, the test has been running for 400 hours at a constant load of 40 MPa√m, with no indication of crack initiation. The plan is to continue the test in its current condition for a total of at least 2,000 hours and perform SEM examination on the notch surface of both specimens. The specimen behavior will be reviewed to determine the next step for this test, with plans centered on introducing fatigue cycling through either mechanical or chemical means.

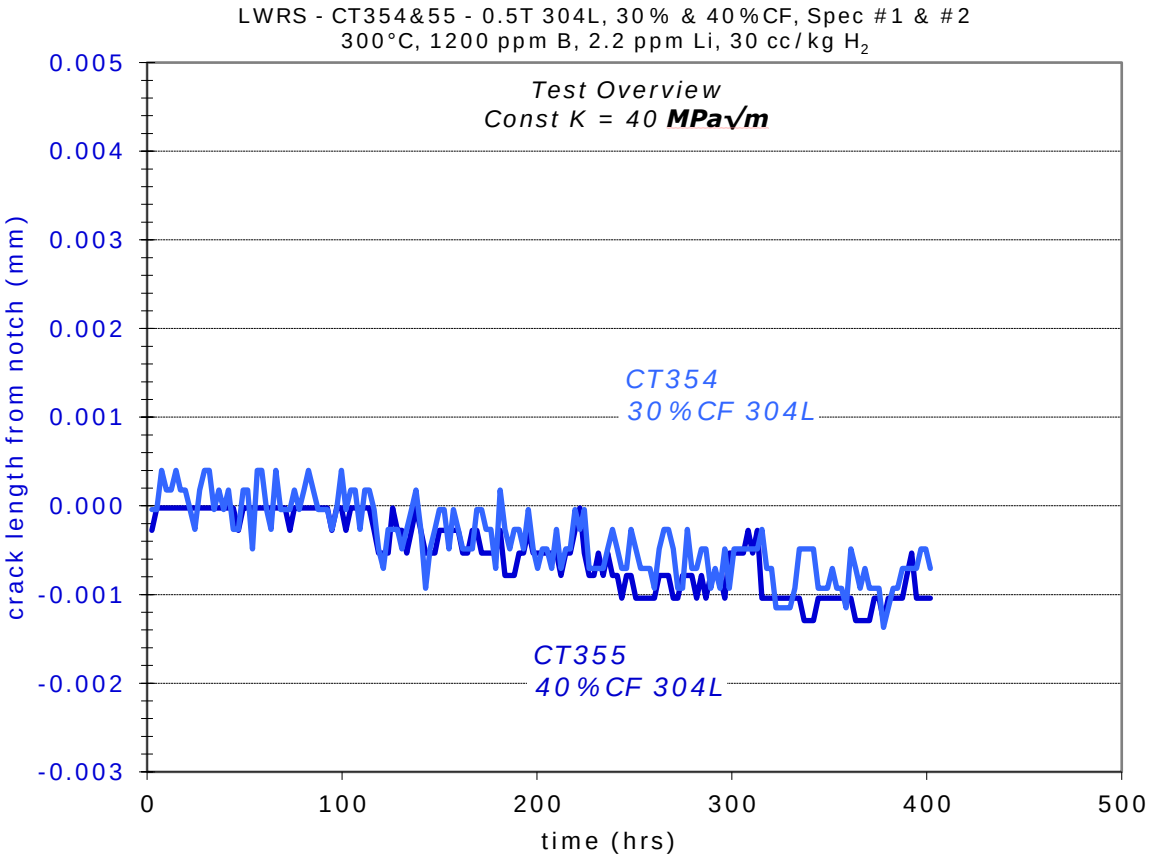

Figure 72. Test overview of the DCPD indicated crack length evolution of CT 354 (30%CF 304L) & 355 (40%CF 304L) BNCT specimens in 300°C PWR primary water containing 30 cc/kg H_2. The testing is ongoing as of the writing of this report.

5. Summary

The IGSCC cases recently reported in 304L/316L(N) auxiliary piping weldments in multiple French PWRs demonstrated that austenitic stainless steels are not immune to IGSCC in PWR primary water. These SCC incidents were among the first cases reported in non-isolable portions of branch piping in the PWR primary circuit, posing threat to nuclear safety and have led to significant financial loss. While weld residual stress has been considered to play a key role in these incidents, it is also recognized that high residual stress alone is insufficient in causing the magnitude of IGSCC cases detected to date. The SCC initiation mechanisms remain largely convoluted due to the complex welding history, operating conditions, and metallurgical characteristics, requiring more systematic studies to determine the effect of each key influencing factor and their interactions. The current study is established to address this need with two primary objectives. The first is to support the cause analysis of recent auxiliary piping SCC incidents reported in French NPPs focusing on knowledge gaps on environmental factors (i.e., dissolved oxygen and temperature). The second goal is to generate service-relevant SS SCC initiation data to inform inspection planning and maintenance strategy development for field applications.

This report documents fiscal year 2025 progress on the parametric study focusing on the role of DO in SCC initiation of cold forged SS. Comprehensive characterizations on the 304L and 316L cold forged to 10, 20, 30, and 40% reduction in thickness, including SEM, XRD analysis, hardness measurements, and tensile testing, were performed to document their microstructural, crystallographic, compositional, and mechanical properties. These data serve as a foundation for evaluating SCC initiation behavior and refining testing plans.

Two ongoing constant-load SCC initiation tests were conducted on 10–40% cold-forged 304L compact tension specimens in 300°C PWR primary water with DO content of 2 ppm and 50 ppb. In situ monitoring using DCPD detected no crack initiation during ~5,000 hours of exposure, although SEM analyses revealed small cracks after ~4,000 hours. Specimens exposed to 2 ppm DO water exhibited more pronounced incipient SCC cracks compared to those in 50 ppb DO water, with both IG and TG cracking observed, and crack density correlating with cold work levels. To simulate service-relevant conditions, periodic partial unloading was introduced, allowing investigation of the combined effects of stress cycling and DO concentration; to date, ~300–500 hours of exposure have accumulated under load cycling conditions with no DCPD-detected crack growth.

Additionally, a new SCC initiation test was initiated in hydrogenated primary water on two cold-worked 304L specimens under constant load in August 2025, with no DCPD indications of crack initiation yet. These tests will continue in their current loading condition until the next SEM surface examination. Regular communication with industry contacts will be continuing to ensure alignment with operational needs.

REFERENCE

[1] G. O. Ilevbare, F. Cattant and N. K. Peat, "SCC of stainless steels under PWR service conditions", in *Fontevraud 7 - 7th International Symposium on Contribution of Materials Investigations and Operating Experience to LWRs' Safety, Performance and Reliability*, 2011, France.

[2] R. Hosler, "Auxilliary Piping SCC OE Focus Group Update (Industry Perspectives), in Advisory Committeee on Reactor Safeguards (ACRS) Meeting 11/16/2022 on French PWR Safety Injection System Cracking ". 2022.

[3] *Preparation for Stress Corrosion Crack Initiation Testing of Austenitic Stainless Steels in PWR Primary Water*. Pacific Northwest National Laboratory: Technical Milestone Report M3LW-23OR0402039, Light Water Reactor Sustainability Program, DOE Office of Nuclear Energy, June 2023.

[4] *Progress on Dissolved Oxygen Effects Evaluation on the Stress Corrosion Cracking Initiation Susceptibility of Stainless Steel in PWR Primary Water*. Pacific Northwest National Laboratory: Technical Milestone Report M2LW-24OR0402033, Light Water Reactor Sustainability Program, DOE Office of Nuclear Energy, PNNL-36636, September 2024.

[5] *Nouvelles détections de fissures sur des tuyauteries du système d'injection de sécurité des réacteurs n° 1 et n° 2 de la centrale nucléaire de Penly et n° 3 de Cattenom (New detection of cracks on pipes of the safety injection system of reactors n° 1 and n° 2 of the Penly nuclear power plant and n° 3 of Cattenom)*. IRSN, March 6th, 2023.

[6] "Safety-relevant damage in the safety injection systems of French nuclear power plants". 05/19/2022.

[7] J. Bartak and N. Camarcat, "Stress Corrosion Cracking on French NPPs – an overview". 2023.

[8] T. Couvant, C. Varé, J. M. Frund, Y. Thébault, B. Audebert and E. Lemaire, "Susceptibility to IGSCC of cold work austenitic stainless steels in non-polluted primary PWR environment", in *Fontevraud 10 - 10th International Symposium on Contribution of Materials Investigations and Operating Experience to LWRs' Safety, Performance and Reliability*, 2022, Avignon, France.

[9] *Materials Reliability Program: Stress Corrosion Cracking of Stainless Steel Components in Primary Water Circuit Environments of Pressurized Water Reactors (MRP-236, Rev. 1)*. EPRI, Palo Alto, CA: 3002009967, 2017.

[10] C. Mayor, "EDF Stress Corrosion Cracking Operating Experience Discussion, in Advisory Committeee on Reactor Safeguards (ACRS) Meeting 11/16/2022 on French PWR Safety Injection System Cracking ". 2022.

[11] "Deciphering the phenomenon of stress corrosion identified on five nuclear reactors (Décryptage du phénomène de corrosion sous contrainte identifié sur cinq réacteurs nucléaires)". January 18th, 2022, Societe Francaise d'Energie Nucleaire - SFEN.

[12] "Update on stress corrosion cracking phenomenon: causes, evolutions, reparations". August 1st, 2022, Societe Francaise d'Energie Nucleaire - SFEN.

[13] IRSN, "Corrosion sous contrainte : quelles répercussions pour les centrales en France ?". 01/12/2023.

[14] *Recommendations Following the Discovery of Intergranular Stress Corrosion Cracks on some French Pressurized Water Reactors*. Western European Nuclear Regulators Association (WENRA), November 2023.

[15] IRSN, "Maîtrise de la conformité et du vieillissement des réacterus - Dialogue technique sur le 4ème réexamen périodique des réacterus de 1300 MWe". June 2023.

[16] EdF, "Phénomène de CSC détecté sur des portions de tuyauteries de circuits auxiliaires du circuit primaire principal de plusieurs réacteurs nucléaires". 06/07/2022.

[17] "Avis IRSN N° 2022-00189". February 14th, 2022.

[18] M. Maisonneuve, C. Duhamel, C. Guerre, J. Crepin and I. de Curieres, "Effect of aerated transients on oxidation and SCC of stainless steels in PWR primary water", in *19th International Conference on Environmental Degradation of Materials in Nuclear Power Systems - Water Reactors, EnvDeg 2019*, 2019.

[19] P. L. Andresen, "Emerging issues and fundamental processes in environmental cracking in hot water", *Corrosion*, Vol.64, Iss.5, 2008, pp. 439-464.

[20] K. Fujimoto, T. Iwamura, S. Suzuki, T. Kobayashi and Y. Kikuchi, "SCC Growth rate of cold worked austenitic stainless steel in PWR environment", in *AECL/COG/EPRI Workshop: Effects of Cold Work on Stress Corrosion Cracking of Materials in Water Cooled Nuclear Plants*, 2007, Toronto, Canada.
[21] *Materials Reliability Program: Stress Corrosion Crack Growth Rates in Stainless Steels in PWR Environments (MRP–458)*. EPRI, Palo Alto, CA: 3002020451, 2022.
[22] B. M. Gordon, D. E. Delwiche and G. M. Gordon, "Service experience of BWR pressure vessels", in *American Society of Mechanical Engineers, Pressure Vessels and Piping Division (Publication) PVP*,
[23] C. Koehler, "Auxiliary Piping SCC OE Focus Group Update - Industry/NRC Materials Technical Exchange Meeting 6/14/23". June 2023.
[24] *Materials Reliability Program: Recommended Factors of Improvement for Evaluating Primary Water Stress Corrosion Cracking (PWSCC) Growth Rates of Thick-Wall Alloy 690 Materials and Alloy 52, 152, and Variants Welds (MRP 386)*. EPRI, Palo Alto, CA: 3002010756, 2017.
[25] Z. Zhai, M. Toloczko, K. Kruska and S. Bruemmer, "Precursor Evolution and Stress Corrosion Cracking Initiation of Cold-Worked Alloy 690 in Simulated Pressurized Water Reactor Primary Water", *Corrosion*, Vol.73, Iss.10, 2017, pp. 1224-1236.
[26] *Pacific Northwest National Laboratory Investigation of Stress Corrosion Cracking in Nickel-Base Alloys, Volume 3: Stress Corrosion Cracking of Cold-Worked Alloy 690*. Pacific Northwest National Laboratory: NUREG/CR-7103 Vol. 3, Nuclear Regulatory Commission, Office of Nuclear Regulatory Research, 2015.
[27] G. S. Was, C. B. Bahn, J. Busby, B. Cui, D. Farkas, M. Gussev, M. Rigen He, J. Hesterberg, Z. Jiao, D. Johnson, W. Kuang, M. McMurtrey, I. Robertson, A. Sinjlawi, M. Song, K. Stephenson, K. Sun, S. Swaminathan, M. Wang and E. West, "How irradiation promotes intergranular stress corrosion crack initiation", *Progress in Materials Science*, Vol.143, 2024, pp. 101255.
[28] K. J. Stephenson and G. S. Was, "The role of dislocation channeling in IASCC initiation of neutron irradiated stainless steel", *Journal of Nuclear Materials*, Vol.481, 2016, pp. 214-225.
[29] E. Blondet and C. Faidy, "High Cycle Thermal Fatigue in French PWR", in *10th International Conference on Nuclear Engineering*, 2002.